To the Graduate Council:

I am submitting herewith a dissertation written by Yang Gao entitled "Liquid Crystals Confined in Nanoporous Silica." I have examined the final electronic copy of this dissertation for form and content and recommend that it be accepted in partial fulfillment of the requirements for the degree of Doctor of Philosophy, with a major in Chemical Engineering.

Hank Cochran
Major Professor

We have read this dissertation
and recommend its acceptance.

John Collier

David Keffer

Robert Compton

Sheng Dai

Accepted for the Council:

Anne Mayhew
Vice Chancellor and
Dean of Graduate Studies

(Original signatures are on the file with official student records.)

LIQUID CRYSTALS CONFINED IN NANOPOROUS SILICA

A Dissertation

Presented for the

Doctor of Philosophy

Degree

The University of Tennessee, Knoxville

Yang Gao

December 2005

DEDICATION

This dissertation is dedicated to my husband Ke An, and our lovely newborn daughter Karrie Elynn An and the rest of my family, for always supporting me, encouraging me, and inspiring me to achieve my goals.

Acknowledgements

I would like to express my sincere gratitude to my advisor Dr. Hank Cochran for his constant support, guidance, and encouragement during my learning process and each stage of my work. I wish to thank Dr. Fouad Aliev and Dr. Sheng Dai for their guidance and all kinds of help they provided during the course of this work. Without their meticulous effort, this work could not have been completed. I also wish to thank my committee members Dr. David Keffer, and Dr. John Collier, and Dr. Robert Compton for their support and suggestions to my work.

I am greatly thankful to the students Sarmiththa, and Manuel in Dr. Aliev's group for teaching me to perform the DSL and DS experiments and helping me to do the data analysis work. I also appreciate all the students and post docs in Dr. Dai's group for their help and suggestions during my work at ORNL.

Finally, I would like to thank for my husband An, Ke and other family members for their constant support and inspiration during all my study life.

Abstract

Confinement has a nontrivial effect on a condensed matter system due to the finite size effect, the surface effect and the induced disorder. Different techniques such as calorimetric measurement, dielectric spectroscopy, dynamic light scattering, X-ray scattering and quasi-elastic neutron scattering have been widely used to study this important topic. Confined liquid crystals (LCs) have attracted great attention in particular because they are a soft system and their physical properties are more easily affected by the geometrical confinement (entropic) effect and the surface interaction (energetic) effect. In this paper, we study the phase transitions and dynamic behavior of LCs, 5CB and 8CB, confined in SBA-15 and MCM-41 mesoporous silica with different pore diameters ranging from 2.3 nm to 25 nm using static and dynamic light scattering and dielectric spectroscopy techniques. SBA-15 and MCM-41 are composed of uniform 2-dimensional hexagonal arrays of cylindrical pores with a sharp pore size distribution. MCM-41 has non-interconnected pores, while only microporous interconnections are found in SBA-15 pores. Such simple geometry can reduce the confusion introduced by the varying pore size and pore interconnectivity in other matrices, which may alter the properties of interest and complicate the interpretation of the experimental results. Moreover, the pore size can be tuned easily by changing the synthesis conditions. This allows us to systematically study the pore size effect on the confined fluids. The experimental results reveal how the geometric confinement and strong interfacial force affect the phase transition

temperature and other physical properties of LCs when the effective dimensionality is changing from 3D to 1D.

Table of Contents

CHAPTER 1 INTRODUCTION 1

1.1 CONFINED LIQUIDS 1

1.2 CONFINED MATRICES 2

1.3 LIQUID CRYSTALS 4

CHAPTER 2 REVIEW OF LITERATURE 6

2.1 PREPARATION AND CHARACTERIZATION OF MATRICES 6

2.2 PRIOR STUDIES OF CONFINED LCS 8

2.2.1 LCs confined in porous glass 10

2.2.2 LCs confined in anopore membranes 13

2.2.3 LCs confined in silica aerogels 16

2.2.4 LCs confined in MCM-41 17

2.3 CURRENT UNDERSTANDING 18

CHAPTER 3 OBJECTIVE OF THIS WORK 20

CHAPTER 4 MATERIALS AND METHODS 24

4.1 LCS 24

4.2 MATRICES 25

4.2.1 MCM-41 synthesis and characterization 25

4.2.2 SBA-15 synthesis and characterization 26
4.2.3 Synthesis and characterization of the transparent silica monoliths 31
4.3 STATIC AND DYNAMIC LIGHT SCATTERING 35
4.3.1 Light scattering in LCs.....39
4.3.2 Experimental setup.....54
4.3.3 DLS data analysis 59
4.4 DIELECTRIC SPECTROSCOPY 62
4.4.1 Dielectric properties of liquid crystals[81] 64
4.4.2 Experimental equipments.....68
4.4.3 Experimental procedure 72
4.4.4 Calibration.....73
4.4.5 The principle of the operation.....76
4.4.6 Evaluation of data 84
CHAPTER 5 EXPERIMENT RESULTS AND DISCUSSION 87
5.1 STATIC LIGHT SCATTERING RESULTS 88
5.2 DYNAMIC LIGHT SCATTERING (PHOTON CORRELATION SPECTROSCOPY) RESULTS.....106
5.2.1 Properties of bulk 5CB.....106
5.3 DIELECTRIC SPECTROSCOPY 126
CHAPTER 6 CONCLUSIONS AND FUTURE WORK 138

6.1 STATIC AND DYNAMIC LIGHT SCATTERING CONCLUSIONS.....138

6.2 DIELECTRIC SPECTROSCOPY CONCLUSIONS.....139

6.3 FUTURE WORKS.....139

REFERENCES CITED.....141

VITA 158

List of Tables

Table 5.1. N-I phase transition temperature of bulk and confined 5CB and 8CB.104

Table 5.2 Fitting results of autocorrelation function for bulk 5CB at different temperature using single stretched exponential equation. 109

Table 5.3 Fitting results of autocorrelation function for bulk 8CB at different temperature using single stretched exponential equation. 114

List of Figures

Figure 1.1. Common phases of a LC. 5

Figure 2.1. Schematic of homogeneous (a) and homeotropic (b) orientations on the surface of the pore wall.....12

Figure 2.2. Escaped-radial structure in a cylindrical cavity.....14

Figure 4.1. A TEM image of the calcined MCM-41 powder sample. 27

Figure 4.2. Nitrogen adsorption/desorption isotherm from MCM-41 powder sample. 28

Figure 4.3. BJH Adsorption Pore size distribution from MCM-41 powder sample. 29

Figure 4.4. TEM images of the calcined SBA-15 powder samples. (a) Pore Diameter =7.3 nm. No swelling agent. (b) Pore diameter = 25 nm. TMB/surfactant (g/g) = 2.0. 30

Figure 4.5. N_2 adsorption/desorption isotherm of 7.3 nm SBA-15 powder sample.32

Figure 4.6. BJH Adsorption Pore size distribution from 7.3 nm SBA-15 powder sample. 33

Figure 4.7. BJH Adsorption Pore size distribution from MCM-41 and SBA-15 powder with different pore sizes.....34

Figure 4.8. TEM image obtained from the calcined film prepared at the water to TEOS ratio of 10 at room temperature. 36

Figure 4.9. Nitrogen adsorption/desorption isotherm from the free-standing film

prepared at the molar ratio of water to TEOS of 10 at room temperature. 37

Figure 4.10. BJH Adsorption Pore size distribution from silica monolith. 38

Figure 4.11. Elastic distortions of a nematic LC: (a) splay (b) twist (c) bend [68]46

Figure 4.12. Light scattering geometries for the (a) splay, (b) twist and (c) bend modes. 48

Figure 4.13. Setup of the computer controlled dynamic light scattering experiments. 55

Figure 4.14. Schematic plot of $\varepsilon_{\parallel}'$ and $\varepsilon_{\perp}'$ against frequency 67

Figure 4.15. Experimental setup of the computer controlled broadband dielectric spectrometer. 69

Figure 4.16. Calibration of sample cell 75

Figure 4.17. Principle of the impedance measurement at low frequencies.....77

Figure 4.18. The principle of the impedance measurement at high frequencies. .79

Figure 4.19. Principle of reference measurement at low frequencies. 81

Figure 4.20. Principle of reference measurement at high frequencies. 83

Figure 4.21. Measurement set up for a sample cell with a round plate capacitor. 85

Figure 5.1. Temperature dependence of intensity of scattered light for 5CB confined in SBA-15 with 25 nm pores (fast run results). 91

Figure 5.2. Temperature dependence of intensity of scattered light for 8CB confined in SBA-15 with 25 nm pores (fast run results). 92

Figure 5.3. Temperature dependence of intensity of scattered light for 5CB confined in SBA-15 with 25 nm pores (slow run results). 93

Figure 5.4. Temperature dependence of intensity of scattered light for 8CB confined in SBA-15 with 25 nm pores (slow run results). 94

Figure 5.5. Temperature dependence of the scattering intensity of bulk 5CB. The inlet shows the temperature dependence of the inverse intensity and the fitting in isotropic phase. (Open circles, experiment; solid lines, fitting.) 96

Figure 5.6. Temperature dependence of the scattering intensity of bulk 8CB. The inlet shows the temperature dependence of the inverse intensity and the fitting in isotropic phase. (Open circles, experiment; solid lines, fitting.) 97

Figure 5.7. Temperature dependence of the scattering intensity of 5CB confined in 25 nm pores. The inlet shows the temperature dependence of the inverse intensity. 99

Figure 5.8. Temperature dependence of the scattering intensity of 8CB confined in 25 nm pores. The inlet shows the temperature dependence of the inverse intensity. 100

Figure 5.9. Temperature dependence of scattering intensity for bulk and confined 5CB. 101

Figure 5.10. Temperature dependence of scattering intensity for bulk and confined 8CB. 102

Figure 5.11. Intensity/intensity autocorrelation functions for bulk 5CB in nematic phase at different temperatures. Open symbols: experiment, solid lines:fitting. 108

Figure 5.12. Temperature dependence of relaxation times due to director fluctuations of bulk 5CB in nematic phase and supercooled state. ..110

Figure 5.13. Intensity/intensity autocorrelation functions for bulk 8CB in nematic phase at different temperatures. Open symbols: experiment, solid lines: fitting. 113

Figure 5.14. Temperature dependence of relaxation times due to director fluctuations of bulk 8CB in nematic phase and supercooled state. ..115

Figure 5.15. Intensity-intensity autocorrelation functions of 5CB in bulk nematic phase and nematic phase confined in 15 nm, 4.7 nm pores.....117

Figure 5.16. Intensity-intensity autocorrelation functions of 8CB in bulk nematic phase and nematic phase confined in 25 nm, 4.7 nm pores.....118

Figure 5.17. Intensity-intensity autocorrelation function of 5CB confined in 4.7 nm pores. Open symbols, experiments; solid line, double stretched exponential fit. 120

Figure 5.18. Intensity-intensity autocorrelation function of 8CB confined in 4.7 nm pores. Open symbols, experiments; solid line, double stretched exponential fit. 121

Figure 5.19. Temperature dependence of τ_1 for bulk and confined 5CB.....123

Figure 5.20. Temperature dependence of τ_1 for bulk and confined 8CB.....124

Figure 5.21. Pore size dependence of effective viscosity. 127

Figure 5.22. Dielectric spectra of bulk 5CB in nematic (1) and isotropic (2) phases. Symbols : experiment; solid lines : fitting. 129

Figure 5.23. Dielectric spectra for bulk and confined liquid crystal.....131

Figure 5.24. Relaxation time distribution functions for bulk and confined liquid crystal.....132

Figure 5.25. Temperature dependence of relaxation times of bulk 5CB. 133

Figure 5.26. Temperature dependence of relaxation times of 5Cb confined in 2.3 nm pores.....135

Figure 5.27. Intensity-intensity autocorrelation functions for bulk and 5cb confined in 2.3 nm pores. 137

CHAPTER 1 INTRODUCTION

1.1 Confined Liquids

Great attention has been given to unveil the abnormal behavior of confined fluids because of their importance in industrial applications such as catalysis and separation. It is well known that the thermal and dynamical properties of confined liquids are different from those of bulk liquids. As the pore size decreases and the surface to volume ratio increases, a combination of finite size effect and interface effect modifies the transport characteristics, phase transition behavior, and other physical properties.

Different confined fluids such as small inorganic molecules (water), small organic molecules (benzene, hexane, cyclohexane), liquid crystals (LCs), and polymers have been studied to reveal the confinement effects. Different confined systems might have dissimilar dynamic behavior, and the experimental results might seem controversial and hard to explain at first sight. Moreover, different techniques such as nuclear magnetic resonance (NMR), dielectric spectroscopy (DS), x-ray and neutron scattering have been widely employed to probe the properties of confined condensed materials. However, good agreement is not always obtained from various experimental techniques, and the results may

sometimes vary by a few orders of magnitude. How to differentiate the roles of the pure geometrical confinement and the liquid-substrate interaction is another realistic problem encountered in experimental studies.

From a theoretical perspective, there is still no universally accepted theory of properties of confined liquids, and the interpretation of experimental results is limited in a very weak theoretical framework. As a matter of fact, there is still a lack of general agreement about the confinement effects on the behavior of liquids among the theoretical predications, experimental data, and the results of computer simulation.

1.2 Confined Matrices

Numerous porous systems such as zeolites, different porous glasses (controlled porous glass, vycor glass), slica aerogels, anopore membranes, and mobil crystalline materials (MCMs) have been studied as model systems to reveal the properties of liquids in confined geometry. These microporous or mesoporous matrices have different pore characteristics such as pore size, pore shape, pore connectivity, volume of void space, surface smoothness, and boundary conditions, which add additional complexity to the studied systems.

Controlled porous glass and vycor glass with interconnected and randomly oriented pores are often used as substrates for thermodynamic studies of confined systems. They have excellent mechanical properties, and can be prepared with a

wide range of porosities and average pore sizes.

Silica aerogels are highly porous solids formed by aggregation and dehydration of suspensions of silica particles of nanometer size. Aerogel consists of a continuously connected network of pores, which can occupy a substantial fraction of the total volume.

Anopore membranes are another type of promising host material for experimental study because of their well-controlled pore size and highly reproducible structure. The cylindrical pores with narrow pore size distribution are aligned with their long axes perpendicular to the membrane surface. Uniformly oriented cylindrical pores can minimize random field effect, which always presents in random porous media.

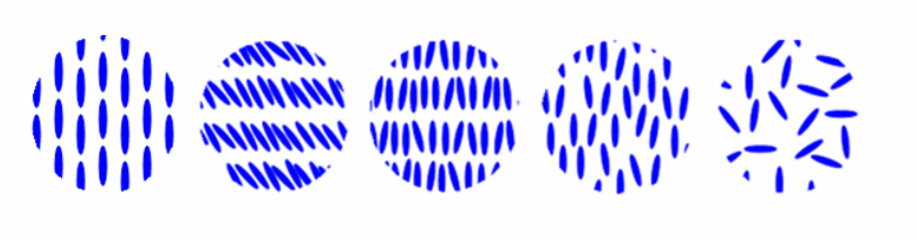
The **M41S** family of mesoporous molecular sieves was first discovered by Mobil scientists in 1992 [1]. By now, different surfactants such as quaternary ammonium surfactants, nonionic alkyl poly(oxyethylene) surfactants, and triblock copolymers have been used as structure-directing agents to synthesize mesoporous materials with various pore sizes, meso-structures, and morphologies [2, 3]. Among these materials, MCM-41 and SBA-15 have been studied in more detail because of their uniform size, cylindrical pore shape, high mesostructure stability, and easily tuned pore sizes.

1.3 Liquid Crystals

A liquid crystal (LC) is a state of matter whose order is intermediate between that of solid and that of liquid. LCs are subdivided into thermotropics and lyotropics depending on the mechanisms that drive their self-organization. The phase transitions of thermotropic LCs are brought out by a change in temperature, while those of lyotropic LCs are controlled by both temperature and solvent concentration.

We will focus on a particular class of thermotropic LCs, namely 4-n-alkyl-4-cyanobiphenyls, which are made up of molecules with a rod-like structure in this research. 4-n-alkyl-4-cyanobiphenyls are often abbreviated as *n*CB, where *n* is the number of carbon atoms in the alkyl chain. In each molecule, a nitrile group (-CN), is attached at one end. The molecules of this series of compounds have large dipole moments of about 5 debye.

There are different types of thermotropic LC phases, depending on the degree of order in the material. The main phases of thermotropic LCs are presented schematically in **Figure 1.1**. In the isotropic (I) phase, molecules are randomly positioned and oriented. In the nematic (N) phase, the molecules have no long range positional order, but have long range orientational order. That is, the molecules tend to align themselves along the same axis which allows us to define an average direction of the molecules called director and denoted by the unit vector **n**. In the smectic (S) phases, a further degree of order is gained. The



Crystal Smectic C Smectic A Nematic Isotropic

Figure 1.1. Common phases of a LC.

molecules have orientational order, and some degree of positional order. A layered structure with a well-defined interlayer spacing is formed, which can be detected by x-ray diffraction. In each layer, the molecules maintain the general orientational order of nematics, and there is no particular positional order inside the layer. More than one type of smectic phase can be formed. However, we only discuss the most distinct phases here. In the smectic A (SmA) phase, the nematic-like director in each layer is normal to the layer; while the molecules in the smectic C phase (SmC) are uniformly tilted with respect to the layer normal. It should be noted that these phases are temperature-dependent and a single LC material can exhibit multiple mesophases.

CHAPTER 2 REVIEW OF LITERATURE

2.1 Preparation and Characterization of Matrices

Both MCM-41 and SBA-15 are ordered mesoporous molecular sieves, which exhibit a 2-dimentional hexagonal array of uniform, straight, cylindrical mesopores.

The silica synthesis occurs by polymerization or condensation during alkolysis of an alkoxysilane precursor (e.g., tetraethoxysilane, TEOS), which can be catalyzed by either acid or base. MCM-41 materials are synthesized by using a quaternary ammonium surfactant as structure-directing agent in alkaline conditions; the interaction between the cationic surfactant head group and anionic silica species is a strong electrostatic interaction (denoted as S^+I^-) [4]. SBA-15 materials use a neutral triblock copolymer as structure-directing agent, which leads to bigger pore diameter (up to 30 nm) and thicker walls. They are prepared in acidic medium (pH < 2); the uncharged silica species interacts with the nonionic triblock copolymer surfactant via weak hydrogen bonding (S^0I^0) [5, 6].

A liquid crystal templating mechanism for the formation of mesoporous molecular sieves such as MCM-41 and SBA-15 has been proposed [1, 7], in which silicate material forms inorganic walls between ordered surfactant micelles.

That is, the silicate first interacts with the surfactant, forming micellar rods. The self-assembly of the silicate/micelle aggregates results in the hexagonal phase.

Surfactant molecules form a hexagonal array of cylindrical micelles, while inorganic silicate species occupy the spaces between the cylinders. Once the ordered silica structure is formed, the surfactant molecules can be removed by calcination or solvent extraction techniques. This synthesis pathway has been confirmed by various experimental techniques [8-10]. The pore diameter can be varied by choosing both the type and the chain length of the surfactant molecules. The pore size can be further expanded by adding a swelling agent such as 1, 3, 5-trimetheylbenzene, which can solvate in the hydrophobic regions of the micelles, causing an increase in micelle diameter [11-13].

Submillimeter-thick transparent silica monoliths can be synthesized by a solvent evaporation method developed by Nagamine, *et al.* [14], which has been widely used to synthesize either supported or self-standing thin films, hollow spheres, and fibers. In this method, a homogeneous solution of alkylsilane, surfactant, ethanol and water with the initial surfactant concentration c_0 less than the critical micelle concentration (cmc) is prepared first. Then, the evaporation of solvent will progressively increase the surfactant concentration, which induces the self-assembly of micelles and the formation of ordered mesophase. The drying time needed for synthesizing submillimeter-thick self-standing film is much longer than that of thin film; therefore effort should be made to retard the condensation rate of silicate to keep it from gelling before the formation of

surfactant mesophase. This can be achieved by decreasing the H_2O/TEOS ratio and lowering the drying temperature.

2.2 Prior Studies of Confined LCs

Numerous experimental works have been done to study the properties of confined fluids. Among these different fluids, the structure and dynamical properties of confined water are one of the most extensively studied topics because it plays a crucial role in a large variety of industrial applications such as mining, corrosion inhibition, enzymatic activity, and food conservation. Various experimental techniques such as differential scanning calorimetry (DSC) [15], Rayleigh light scattering [16], x-ray and neutron diffraction [17-19], quasi-elastic neutron scattering (QENS) [20, 21], and molecular dynamics (MD) simulation [22, 23] have been used to investigate confined water. A slowing down of the translational and rotational motion of water molecules confined in vycor glass has been observed via quasi-elastic and inelastic incoherent neutron scattering techniques [24]. The slowing down arises from both geometrical confinement (entropic trap) and water-substrate interaction (energetic trap). The confined water can be super-cooled to much lower temperature compared with the bulk state. Both experimental and computer simulation results suggest that there exists a thin layer of bound water close to the substrate as compared to bulk water [25]. The free water in the middle undergoes a sharp liquid-solid phase transition, while

bound water close to the pore wall shows glass-like behavior. If the pore size is small enough, only bound water is present. MD simulations [26-31] also established that water molecules close to both hydrophobic and hydrophilic substrates tend to form a double layer with higher density compared with bulk water, regardless of the specific water-substrate interaction and the pore shape. In the case of cylindrical SiO_2 pores, the hydrogen bond distribution of confined water is changed, and the orientational order of water molecule is disturbed. The molecules close to the pore wall are less hydrogen-bonded than in the bulk for hydrophilic confinement, while the number of hydrogen bonds is larger than the bulk value for hydrophobic confinement.

Small organic molecules such as cyclohexane and benzene confined in ordered mesoporous silicas MCM-41 and SBA-15 were studied by differential scanning calorimetry (DSC) and proton NMR experiments [32, 33]. The results show that the dynamics of the confined liquids are slowed down compared to bulk at room temperature, and the molecular mobility decreases with decreasing temperature but is still much faster than that in the bulk crystal. No sharp phase transition was found in the confined systems. This suggests that a highly diffusive solid or a highly viscous liquid is formed inside the pores and there is no obvious distinction between the surface molecules and molecules at the center of the pores. Both QENS and pulsed field gradient NMR (PFG-NMR) have been used to study the diffusivity of benzene and cyclohexane confined in a microporous silica powder [34]. These two techniques are complementary and provide more

complete information about the structure and dynamics of the confined molecules at different time and length scales. QENS (time scale ~1 ns) probes the molecular diffusion at a nanometer length scale, while PFG NMR (time scale ~ 1 ms) probes molecular diffusion at a micrometer length scale. The experimental results from these two techniques are in a good agreement. This suggests that there are no transport resistances with length scale above the nanometer scale.

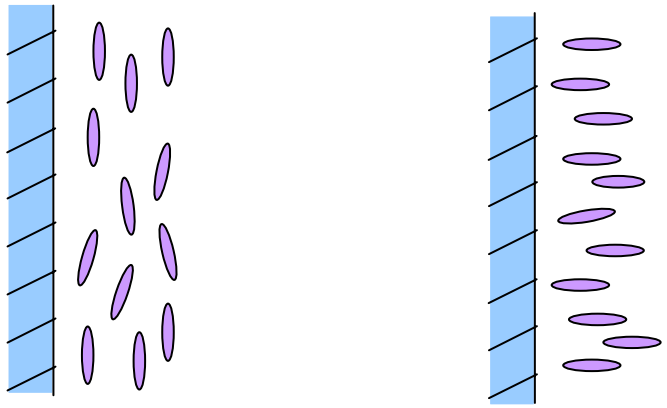
LCs are another kind of well-studied fluid system. In recent years, the study of intermolecular interactions and physical properties of different LCs has attracted great attention because of their wide application in electronic devices. Confined LCs are of particular interest because such systems allow us to investigate the interaction mechanism between LC and the surface active centers. Different systems, such as zeolites, mesoporous molecular sieves, porous glasses, and silica aerogel [35], with pore size ranging from a few angstroms to several tenths of micrometer have been investigated using different techniques. Infrared (IR) absorption spectroscopy and DSC methods have been used to investigate the intermolecular interactions between the LC molecules and the pore surface and the phase behavior of LCs respectively. Deuterium NMR (DNMR) is another well established technique being used to study the orientational order and dynamics of LCs in porous matrices [36-38].

2.2.1 LCs confined in porous glass

Vilfan *et al*. [39] used DNMR to study the surface induced disorder and diffusion coefficient of pentylcyanobiphenyl (5CB) LC confined in porous glass

with average pore diameter ranging from 7.5 nm to 140 nm. Their results show that an arrangement of molecules parallel to the wall is induced by the local molecular interactions between the LC and the solid wall, and the surface order parameter S_0 is found to be around 0.02 ± 0.01. No significant slowing-down of molecular diffusion was found near the wall.

Zidansek *et al*. investigated the nematic to smectic-A (N-SmA) phase transition of octacyanobiphenyl (8CB) LC confined in controlled porous glass with the aid of x-ray scattering. The host matrix, with average pore radius $R = 0.2\ \mu m$, consisted of cylindrically shaped voids that are strongly curved and interconnected. Both non-treated and silane-treated samples were measured. The orientational anchoring was found to be homogeneous and homeotropic, respectively. As seen in **Figure 2.1**, for homogeneous alignment, the director is parallel to the pore surface, while for homeotropic alignment, the director is perpendicular to the pore surface. In both samples, as the temperature decreases, the correlation length increases monotonically and approaches a maximum less than the pore radius *R*. This suggests that each smectic domain is surrounded by a nematic phase or the cavity wall. The domain size was found to increase monotonically with decreasing temperature. Pre-smectic behavior was observed in the silane-treated sample because the coupling interaction between the surface and LC is strong enough to form a few smectic layers at a temperature above the bulk N-SmA phase transition temperature, while such behavior is absent in the non-treated sample because of the relatively weak surface interaction [40].



(a) (b)

Figure 2.1. Schematic of homogeneous (a) and homeotropic (b) orientations on the surface of the pore wall.

2.2.2 LCs confined in anopore membranes

Finotello *et al.* [41] made specific heat measurements on the homologous alkylcyanobiphenyl (*n*CB) series confined to $0.2\ \mu m$ untreated and treated anopores. For untreated anopore, the LC molecules are aligned parallel to the channel long axis; after lecithin or aliphatic acid treatment, the alignment was homoetropic. The specific heat peaks at the weak first order isotropic to nematic (I-N) phase transition are suppressed, rounded, broadened, and shifted to lower temperature for both untreated and treated samples. These effects are severe for treated samples. The 8CB N-SmA phase transition in anonpore is affected even more than the I-N transition. In the non-treated sample, a shell of nematic material remains near the pore wall, which does not participate in the N-SmA phase transition. This shell of nematic material acts as a disordering surface for the enclosed smectic phase, lowering the transition temperature. In the lecithin-treated sample, fewer smectic layers are formed near the pore wall, leaving a nematic core in a nearly escape-radial configuration, as shown in **Figure 2.2**. The specific heat peak maximum is even smaller, and the smectic correlation length is much less than the pore size.

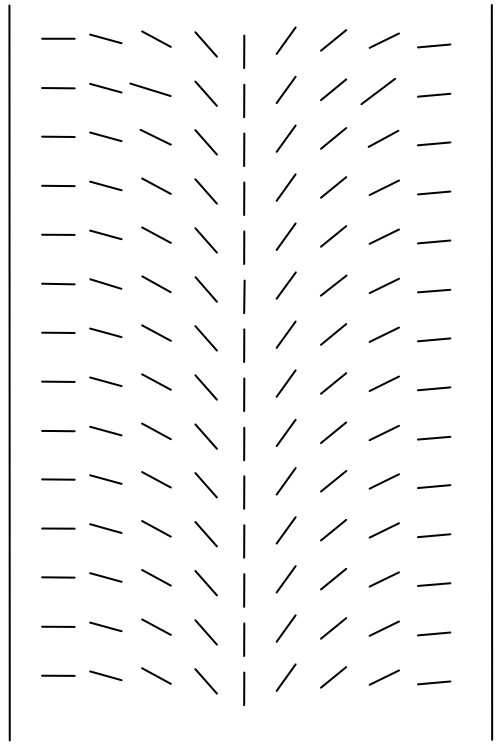


Figure 2.2. Escaped-radial structure in a cylindrical cavity.

Static and dynamic light scattering experiments were used to study the influence of boundary conditions and layer thickness of 8CB confined to $0.2\ \mu m$ anopores[42]. Different amounts of 8CB were impregnated into non-treated and lecithin-treated samples. The 8CB forms a thin layer on the pore wall with different layer thickness. The phase transition temperature of confined 8CB depends on the molecular orientation as well as the LC layer thickness. The influence of boundary conditions and LC layer thickness on the N-SmA phase transition is more prominent than that on the I-N phase transition. Static light scattering results indicated that the I-N phase transition temperature decreases with decreasing LC layer thickness. In the nematic phase, two well-defined relaxation processes were observed in dynamic light scattering experiments for 8CB confined to anopores. The first process is associated with bulk-like nematic director fluctuations, while the second, slower relaxation process is most likely due to the fluctuations of director orientations in layers close to the pore wall surface. For non-treated samples, the amplitude of the slower process is greater for thinner layers; while for treated samples, the amplitude of the slower process is greater for thicker layers because the surface-induced orientation extends for a longer distance toward the pore center in thicker LC layers. All these observations suggest that the slow process is a surface related relaxation.

Broadband dielectric spectroscopy was also applied to study the dynamic behavior of 8CB confined in anopores[43]. In low frequency measurements, the slow relaxation process of surface polarization arising at the pore wall-LC

interface was observed for both non-treated and treated anopores. The relaxation rate is slower for the homogeneous alignment than for the homeotropic alignment. This can be explained by the hypothesis that the viscosity of the surface layers with homogeneous alignment is greater that with homeotropic alignment. With the aid of high frequency measurements, the molecular relaxation due to orientations of molecules around their short axis and to librational motion can be observed in non-treated and treated samples, respectively. The relaxation process associated with librational motion of molecules in the lecithin-treated samples is faster than that in bulk and non-treated samples, and the process due to the rotation of molecules around the short axis is faster in confined LC than that in the bulk.

2.2.3 LCs confined in silica aerogels

Light scattering and precision calorimetry results show that in the aerogel the bulk first-order I-N phase transition of 8CB is replaced by a continuous nematic ordering, and the second-order N-SmA phase transition is absent or greatly broadened. Crystallization is suppressed to below $0°C$ in the aerogel [44].

The x-ray scattering method was used to study smectic ordering in a silica aerogel with pore volume fraction $\phi = 0.79$. It was found that the N-SmA phase transition was eliminated and replaced by a short range smectic ordering having a short correlation length, $\xi \sim 40$ Å, at the N-SmA phase transition temperature, T_{NA}, which is much smaller than the aerogel pore and nematic domain size,

$\xi_P \sim 200$ Å. As the temperature is lowered, this smectic disorder is eliminated from the pores, and correlation length increases continuously and saturates to ξ_P at $20°\text{C}$ below the T_{NA} [45].

Deuterium nuclear magnetic resonance (DNMR) was also used to study the behavior of 8CB nematic LC confined in silica aerogels with density range from 0.068 to 0.6 g/cm^3 [46]. The results show that 8CB molecules are primarily aligned perpendicular to the aerogel surface. The weak first-order N-I phase transition becomes less discontinuous with decreasing pore size, and it eventually becomes continuous at an aerogel density between 0.36 and 0.5 g/cm^3 because of the increase in available surface area.

2.2.4 LCs confined in MCM-41

Gavrilko and other researchers [35] investigated the intermolecular interactions of 5CB encapsulated in the mesoporous molecular sieves MCM-41 and the corresponding Cu containing Si, Al-MCM formula using both infrared (IR) spectroscopy and differential scanning calorimetry (DSC) methods. The host matrices in their study had a unidimensional mesoporous structure with regular, hexagonal arrangement of channels of 25 Å in diameter. The IR adsorption spectra indicated that hydrogen bonds $-C \equiv N \cdots H - O - Al(Si)$ were formed between 5CB molecules and the hydroxyl groups of the channel walls. In the MCM-41 + 5CB system, most of the 5CB molecules are anchored to the walls and arrange themselves perpendicular to the channel axis, which prevents further

filling of the channels. In the Cu-MCM-41 + 5CB system, most of the 5CB molecules are in the form of undisturbed dimers with their long axis parallel to the channel axis. DSC results show that the I-N phase transition was observed only in the Cu-MCM-41 + 5CB system, and no crystalline-nematic phase transition was found for either system. This suggests that, in the Cu-MCM-41 + 5CB system, the 5CB molecules are in a supercooled liquid state; whereas in the MCM-41 + 5CB system, most of the 5CB molecules are bound to channel walls through H-bonds.

2.3 Current Understanding

Confined LCs have attracted great attention because they are “soft” systems [41]. The weak orientational and transitional order is considerably influenced by the presence of surface. In addition, LCs exhibit rich phase transition behaviors with different order. Therefore, LCs offer a great opportunity to investigate how the confinement effects affect the dynamics of molecular motion, viscous properties and phase transition behaviors. The above review shows that a variety of unexplained physical properties and phase transition phenomena of LCs confined in both random porous matrices and cylindrical pores has been studied both experimentally and theoretically. The modifications of orientational order, elastic properties, and phase transition temperature arise from various molecular orientations in pores. The dynamic properties of confined LCs are affected by both finite size effect and surface effect. Either an increase or a

decrease of Isotropic-Nematic phase transition temperature of LCs confined in polyvinyl alcohol and SiO- treated substrate was observed depending on the ordering and disordering nature of the substrate [47]. The presence of surface may separate LC into distinct regions, each with its own dynamic features. It has been found that slow relaxation process and a broad spectrum of relaxation times are observed for confined LCs, which are absent for the bulk LCs. The slow dynamics suggests that an interfacial layer is formed on the pore wall. Although great success has been made to understand the physical and thermodynamic properties of confined LCs, little work has been done to systematically study how the confinement effects modify the dynamic behaviors of LCs. In this work, we use static and dynamic light scattering and dielectric spectroscopy as the main detecting techniques; systematically study how the confinement effects influence the behaviors of LCs as a function of pore diameter.

CHAPTER 3 OBJECTIVE OF THIS WORK

The confinement effect on the dynamic behaviors and the phase transitions of LCs confined by porous glass, silica aerogel, and polymer dispersed Liquid crystal have been well studied both theoretically and experimentally[48-52]. A wide distribution of relaxation times was observed in these systems as comparing with the well-defined exponential decay of relaxation rates in bulk LCs. A shift in the isotropic-nematic phase transition temperature has also been found which indicate a possible change from a first order to a continuous transition. However, the understanding of these phenomena is still in the initial stage. It is still hard to separate the roles played by surface effect and confinement effect which cause the unusual behaviors of LCs.

Novel nanoporous materials typified by MCM-41 and SBA-15 offer exceptional promise as media for separations and reaction. However, the molecular-level structure and the properties of liquids confined in nanoscopic pores are strongly affected by both the geometric confinement and the dominant interfacial force. Our goal is fundamental understanding of how these two factors control liquid structure and properties. To this end we have initiated coordinated molecular simulations and experiments probing the statics and dynamics of nanoscopically confined liquids. Preliminary DLS and DS results with confined

liquid crystals (small molecule LCs: 5CB and 8CB) suggest dramatic changes in the phase transition temperature. Previous studies have used samples with tortuous, non-uniform, and interconnected channels which lead to large variance in sample pore diameter and confound unambiguous theoretical understanding or have covered only a very narrow range of important variables. None of the previous studies has provided a broad set of systematic data for clear interpretation and understanding. Our suite of samples, synthesized just for these experiments, covers a wide range of pore diameters and each sample has a very small variance in the diameter of the straight, nonintersecting pores. We expect to gain fundamental understanding of how confinement affects the phase-change temperature and approach to criticality of liquid crystals of two sizes in pores over a range of sizes.

We propose to perform dynamic light scattering (DLS), dielectric spectroscopy (DS), and (if beamtime is available) x-ray scattering experiments to study the phase transition behavior and other physical properties of 4- n-pentyl-4'-cyanobiphenyl (5CB) and 4- n-octyl-4'-cyanobiphenl (8CB) confined in MCM-41 and SBA-15 as a function of pore diameter, with diameter varying systematically from 2.3 to 25 nm.

Confined liquid crystals (LCs) have been widely investigated because they are a soft system and their physical properties are more easily affected by the geometrical confinement effect (entropic) and the surface interaction (energetic) effect [53-56]. X-ray scattering techniques have been used to study the nematic to

smectic A phase transition of octylcyanobiphenl (8CB) confined in random porous media such as silica aerogel, aerosol gels, controlled porous glass [40, 45, 57, 58]. Such systems consist of an interconnected network of pores of varying shape, curvature, and size.

We are going to use MCM-41 and SBA-15 as host matrices. MCM-41 and SBA-15 are promising materials that can be used to study finite size and surface effects on confined fluids because MCM-41 and SBA-15 are composed of uniform 2-dimensional hexagonal arrays of cylindrical pores with a sharp pore size distribution. MCM-41 has non-interconnected pores, while only microporous interconnections are found in SBA-15 pores [59, 60]. Such simple geometry can reduce the confusion introduced by the varying pore size and pore interconnectivity in other matrices, which may alter the properties of interest and complicate the interpretation of the experimental results. Moreover, the pore size can be tuned easily by changing the synthesis conditions. This allows us to systematically study the pore size effect on the confined fluids. The surface of both materials contains hydroxyl groups, which may form hydrogen bonds with other appropriate molecules confined in the matrices. Specific surface interaction effects on the properties of the confined fluids may also be studied by surface modifications, which can be achieved by grafting hydrophobic groups on the surface. This would allow us to reveal how the geometric confinement and strong interfacial force affect the phase transition behavior, criticality, and other physical properties of LCs when effective dimensionality is changing from 3D to 1D.

According our knowledge, little work has been done to study the confinement effect in such well-defined geometries, and the systematic study of the effect of the pore radius on the phase transition behavior of LCs is still lacking.

The previous BET and X-ray diffraction experimental results show that both MCM-41 and SBA-15 mesoporous matrices have a crystal-like hexagonal arrangement of cylindrical pores with narrow pore size distribution. Also, from the results of the dynamic light scattering experiment we have done, we could deduce that almost all of the LC is confined inside the pores because the bulk phase transition is not observed; instead, the observed peak shape has been changed and shifted in the confined samples.

CHAPTER 4 MATERIALS AND METHODS

4.1 LCs

4-n-pentyl-4'-cyanobiphenyl (5CB, 98%), and 4-n-octyl-4'-cyanobiphenyl (8CB, 98%) are used in this work as model compounds for studying the modified mesogenic behavior and effects of confinement on properties of LCs. They are purchased from Sigma-Aldrich Company and used as received without further purification.

Both 5CB and 8CB are rod-like molecules with a strong dipole moment (~5 D) oriented along the molecular long axis. Bulk 5CB has a molar mass 249.36 g/mol, with a molecular length of around 1.9 nm and a diameter of around 0.7 nm [61]. It has a stable nematic phase in the temperature range 22.5 to 35 °C. Bulk 8CB has a molar mass 291.44 *g/mol* and molecular length around 2.2 nm [62]. For bulk 8CB, the weak first-order I-N phase transition occurs at about 40.5 °C, and the second-order N-SmA phase transition occurs at around 33.7 °C. Bulk 8CB crystallizes via a strong first-order phase transition at approximately 21.5 °C. Thus, the nematic phase is stable from about 33.7 to 40.5 °C.

4.2 Matrices

Different porous matrices such as porous silicate glass, anopores and so on have been used to investigate confinement effects on LCs. Silica mesoporous materials like MCM-41 and SBA-15 are ideal materials for such study because they are composed of hexagonal arrays of cylindrical pores with a narrow pore size distribution. At the same time, the pore size can be tuned easily by changing the synthesis conditions. Also, the dielectric permittivity of the silica mesoporous matrix is independent of the temperature and frequency for a wide range of frequencies. Moreover, the interpretation of the dielectric measurement results can be greatly simplified due to the negligible electrical conductivity of the silica matrix.

4.2.1 MCM-41 synthesis and characterization

MCM-41 was synthesized in a basic medium [4]. The typical synthesis procedure of MCM-41 is as follows: 16.7 ml 35% ammonia solution (NH_4OH) is mixed with 100 g distilled water. 2.3 g surfactant hexadecyltrimethylammonium bromide (CTAB) is then added to the solution with stirring until a homogenous solution is formed. 5.2 ml tetraethyl orthosilicate (TEOS) is dropped in slowly. The reaction temperature is kept at 80-90 $^{\circ}C$ for 2 h and white slurry is obtained. The resulting product is filtered, and washed with a large amount of distilled water, and dried at ambient temperature. The surfactant can be removed by calcinations in air at 873 K for 6 h.

A TEM image of the calcined MCM-41 powder sample is shown in **Figure 4.1**.

The nitrogen adsorption/desorption isotherm, and pore size distribution are shown in **Figure 4.2** and **Figure 4.3**, respectively.

4.2.2 SBA-15 synthesis and characterization

SBA-15 powders were synthesized as reported by Zhao, *et al.* [5, 6]. 8 g Pluronic P123 ($EO_{20}PO_{20}$ EO_{20}) is dissolved in 125 g H_2O and 50 g HCl solution (37.5 wt % aq). The mixture is stirred for about 3 hours until a homogenous solution is formed. Another 125 g H_2O is then added. After stirring for about 10 min, 17.2 g TEOS is added. The resulting mixture is stirred for 30 min and then kept at 308 K for 1 day without stirring. After that, the reaction temperature is increased to 373 K and kept at the same temperature for 1 more day. The resulting solid product is obtained by filtration, washed with water or ethanol, and dried in an oven for 6 h at 373 K. The surfactant can be removed by calcining the sample in air at 823 K for 6 h.

The pore size of SBA-15 with 2D hexagonal structure can be further increased to ~ 300 Å by increasing the hydrophobic volume of the self-assembled aggregates. This can be achieved by adding co-solvent organic molecules such as 1, 3, 5-trimethylbenzene (TMB).

TEM images of the calcined SBA-15 powder samples with different pore sizes are shown in **Figure 4.4**. As can be seen in **Figure 4.4** (b), the mesostructure of SBA-15 is less well-defined if the swelling agent is added to increase the pore

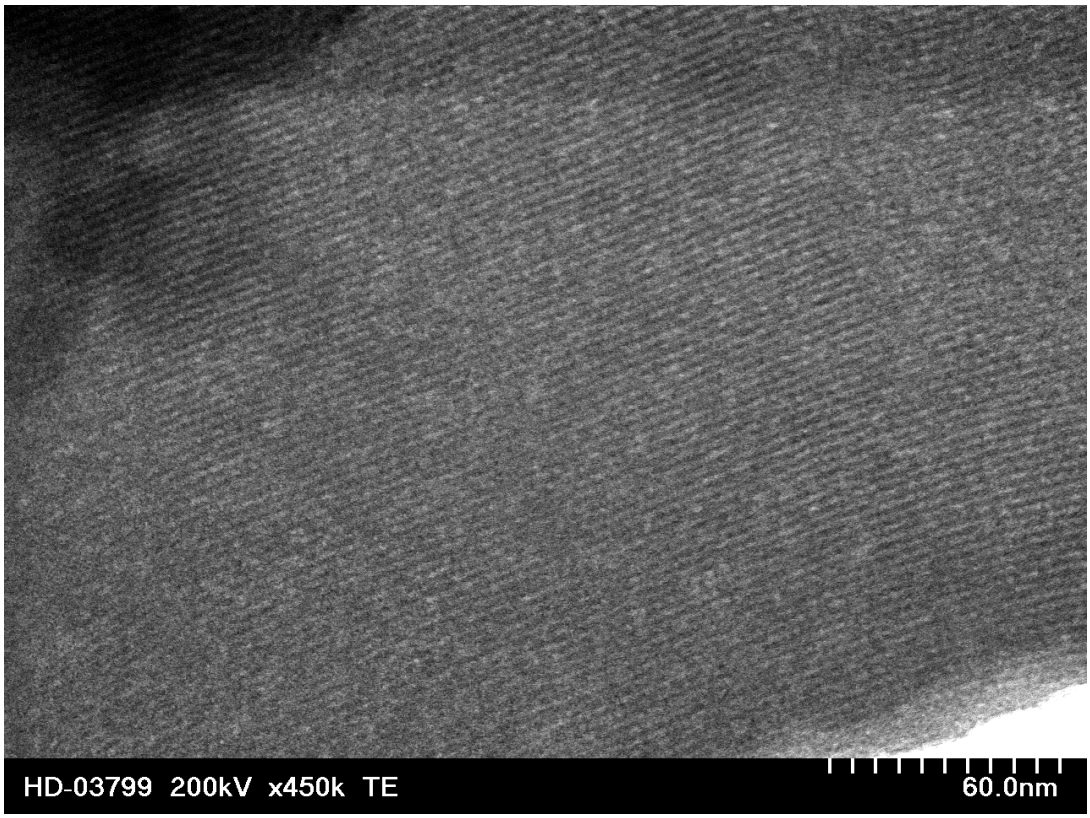


Figure 4.1. A TEM image of the calcined MCM-41 powder sample.

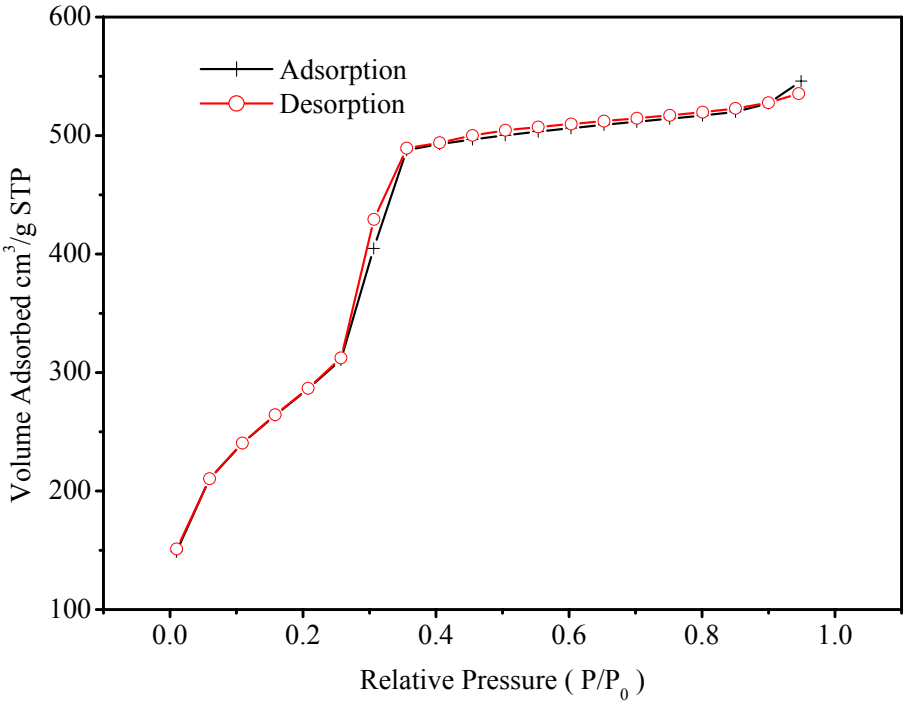


Figure 4.2. Nitrogen adsorption/desorption isotherm from MCM-41 powder sample.

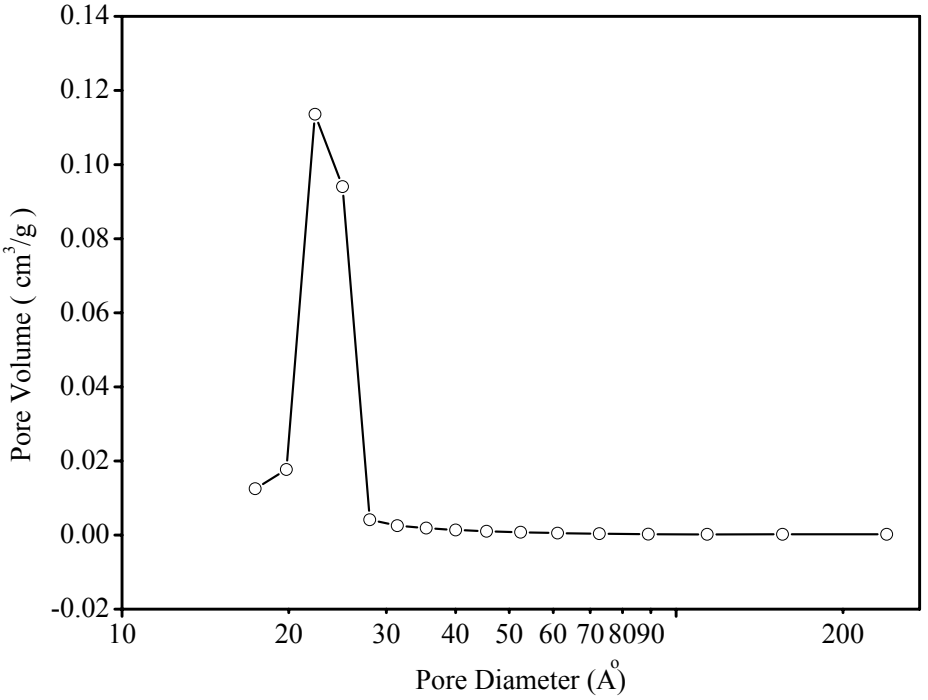
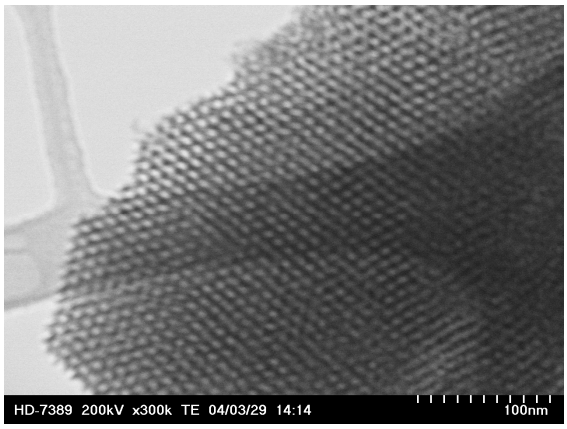
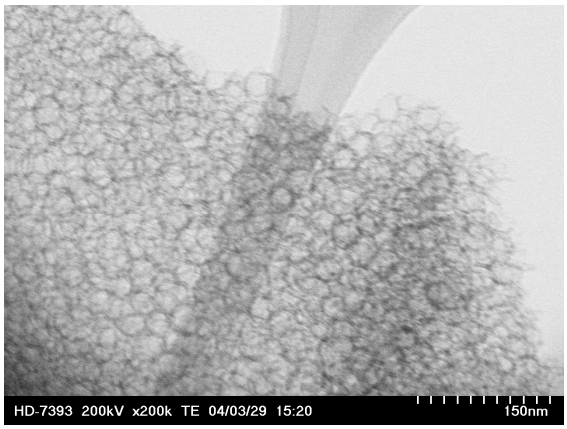


Figure 4.3. BJH Adsorption Pore size distribution from MCM-41 powder sample.



(a)



(b)

Figure 4.4. TEM images of the calcined SBA-15 powder samples. (a) Pore Diameter =7.3 nm. No swelling agent. (b) Pore diameter = 25 nm. TMB/surfactant (g/g) = 2.0.

size. The nitrogen adsorption/desorption isotherm, and pore size distribution are shown in **Figure 4.5** and **Figure 4.6**, respectively. **Figure 4.7** shows pore size distribution of MCM-41 and SBA-15 powder samples with different pore sizes.

Nitrogen adsorption isotherms of SBA-15 are in agreement with those reported earlier [5, 6]. A hysteresis loop with sharp adsorption and desorption branches was observed, and the capillary condensation occurs at higher relative pressures compare with MCM-41. The sharpness of the adsorption branch indicates a narrow pore size distribution.

4.2.3 Synthesis and characterization of the transparent silica monoliths

Transparent silica monoliths were synthesized according to the procedures described by Nagamine, *et al* [14], For a typical synthesis procedure, 2.08 g TEOS, 4.61 g ethanol, and 0.728 g hexadecyltrimethylammonium bromide (CTAB) were mixed and stirred until a homogenous solution was formed. 1.8 g HCl aqueous solution (0.003 M) was added to the mixture and stirred for 2 h at room temperature. The molar ratio of each component was 1 TEOS: 0.2 CTAB: 10 H_2O: 10 Ethanol: 5.4 $\times 10^{-4}$ HCL. After stirring, the solution was transferred to a Petri dish and dried at room temperature for several days. The initial depth of the solution was kept at ~3-4 mm. During the gelation process, the resultant self-standing film peeled off from the Petri dish, and broke into small pieces, ~5 mm. After the pieces of self-standing film were completely dried, they were calcined at 873 K for 6 h to remove the surfactant. A transparent mesoporous silica monolith

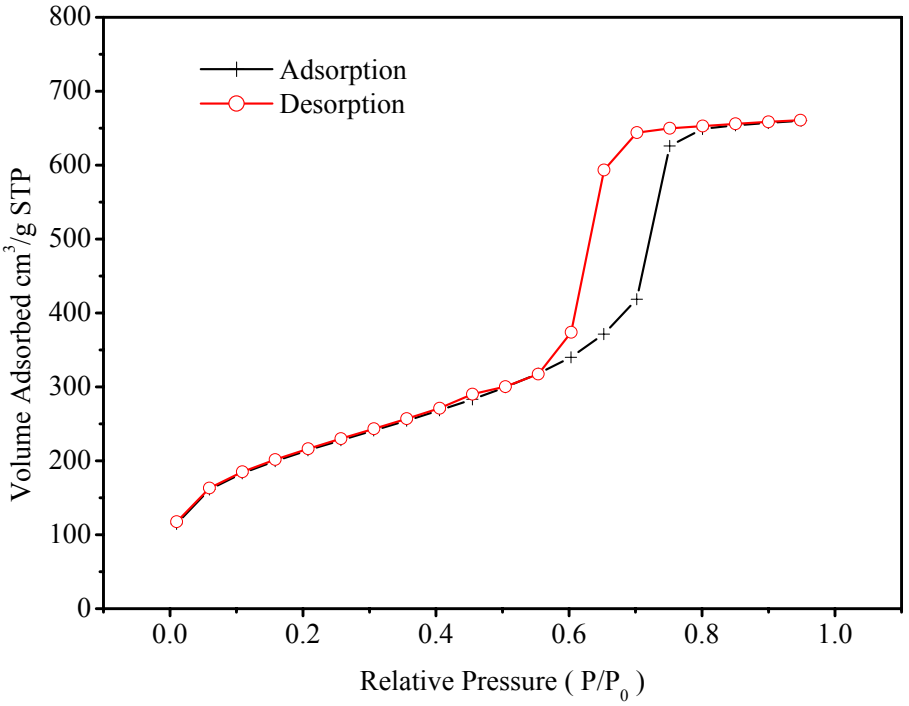


Figure 4.5. N_2 adsorption/desorption isotherm of 7.3 nm SBA-15 powder sample.

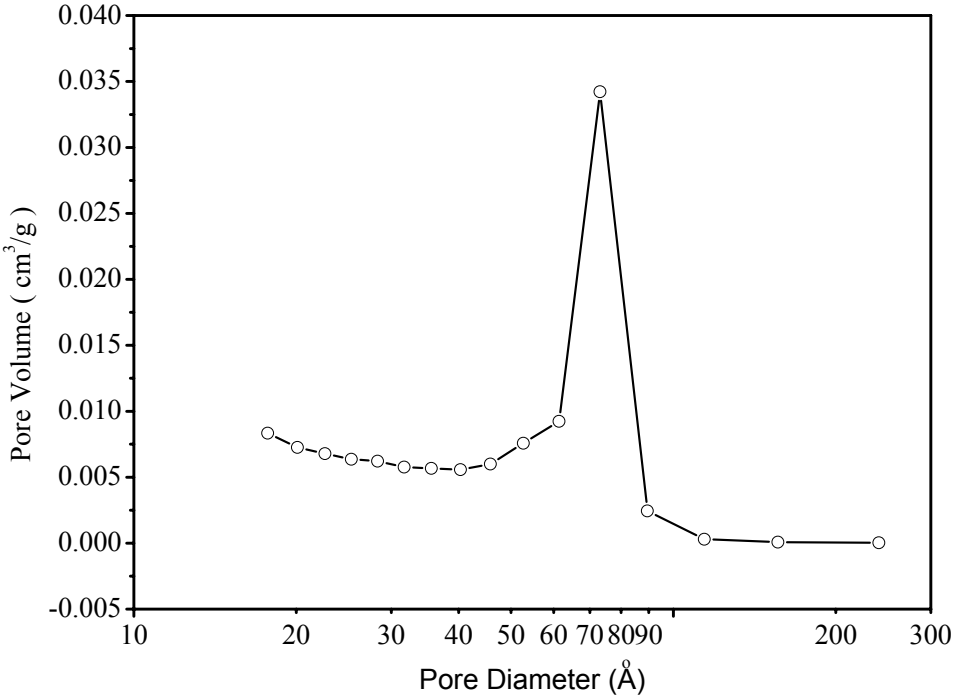


Figure 4.6. BJH Adsorption Pore size distribution from 7.3 nm SBA-15 powder sample.

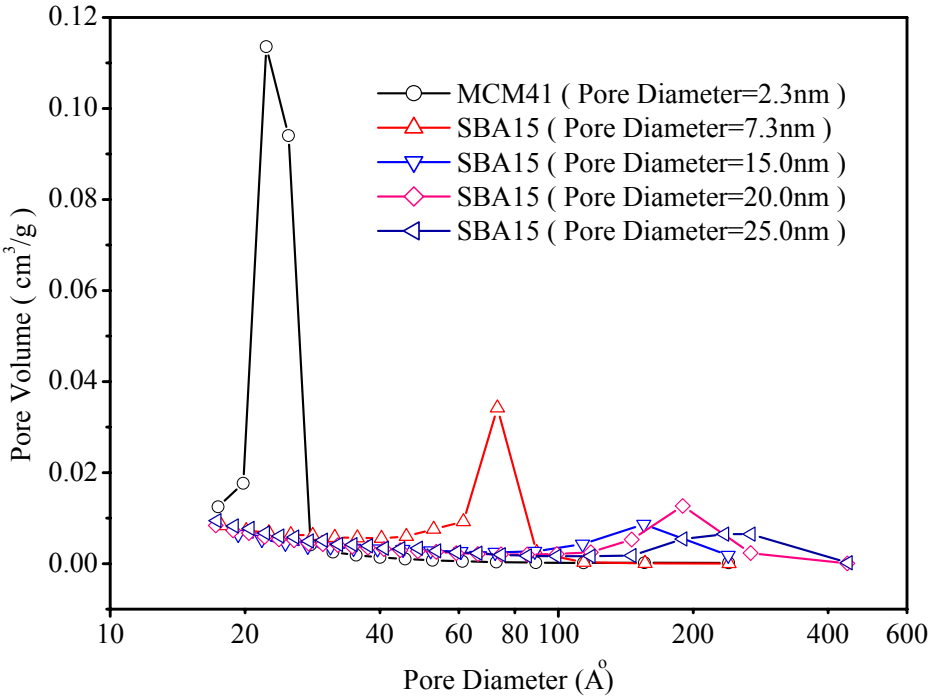


Figure 4.7. BJH Adsorption Pore size distribution from MCM-41 and SBA-15 powder with different pore sizes.

is formed.

We characterized the matrices used in this work by transmission electron microscopy (TEM), and nitrogen adsorption measurements. A TEM image of a calcined silica monolith is shown in **Figure 4.8**. The cylindrical silica channels are clearly observed; it should be noticed that the channels are aligned in different directions in different sub-regions, and the sample also includes non-structural parts as well.

Nitrogen adsorption experiments (BET analysis) were used to characterize the pore size distribution. Pore size was analyzed by the Barrett-Joyner-Halenda (BJH) method [63] with N_2 adsorption isotherms at 77 K. The BET surface area was found to be about 1139 m^2/g, and the pore volume was 0.52 cm^3/g. The nitrogen adsorption and desorption isotherms and pore size distribution are shown in **Figure 4.9** and **Figure 4.10**, respectively. The absence of hysteresis in the adsorption/desorption curve indicates that virtually all of the pores are accessible (negligibly few bottlenecks or dead-ended pores). The very narrow pore size distribution and the absence of significant pore volume at larger diameter reflect the uniformity of the cylindrical pore structure in these monoliths.

4.3 Static and Dynamic Light Scattering

Light scattering experiments are performed using a λ=0.6328 μm He-Ne laser and ALV-5000/Fast Digital multiple-tau correlator operating over delay

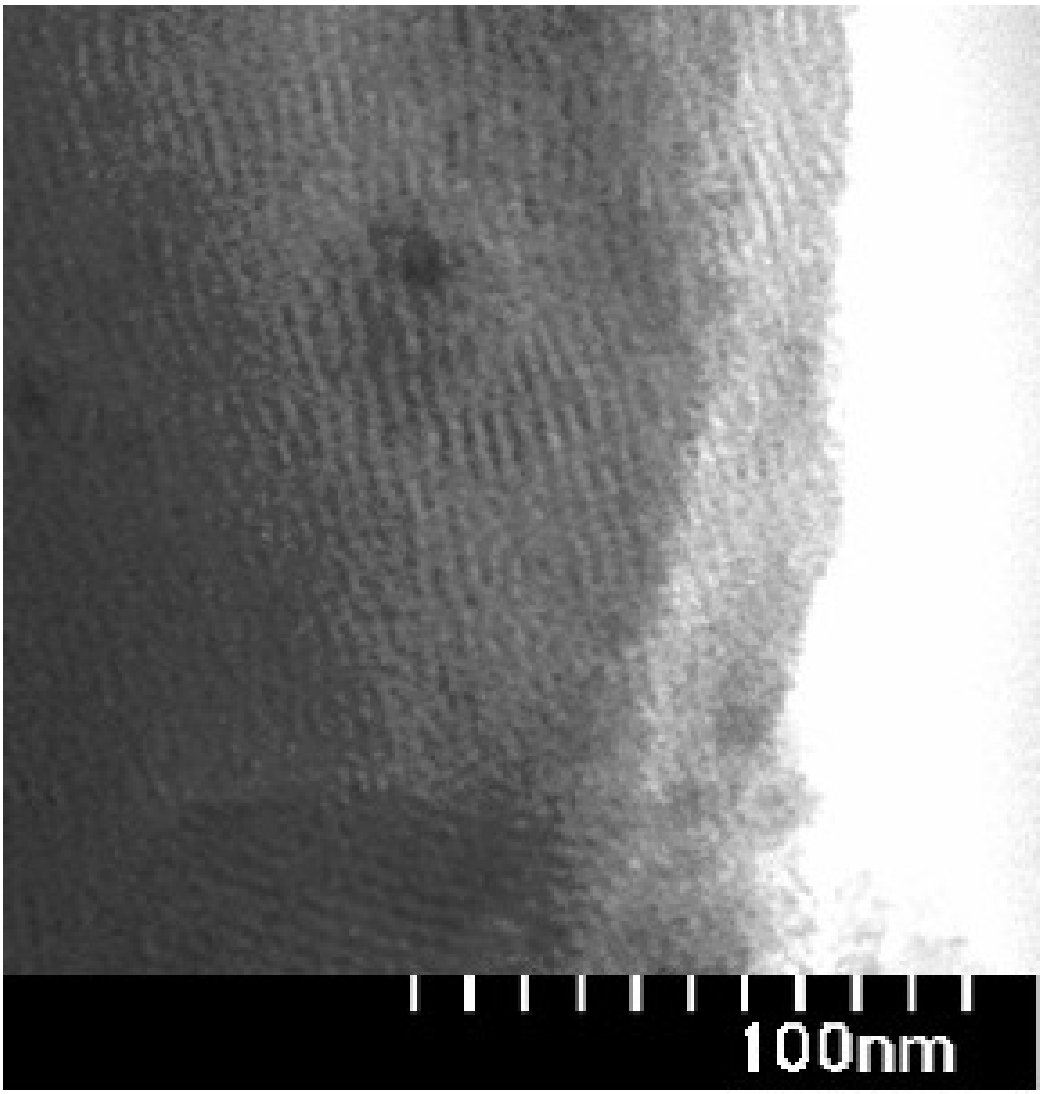


Figure 4.8. TEM image obtained from the calcined film prepared at the water to TEOS ratio of 10 at room temperature.

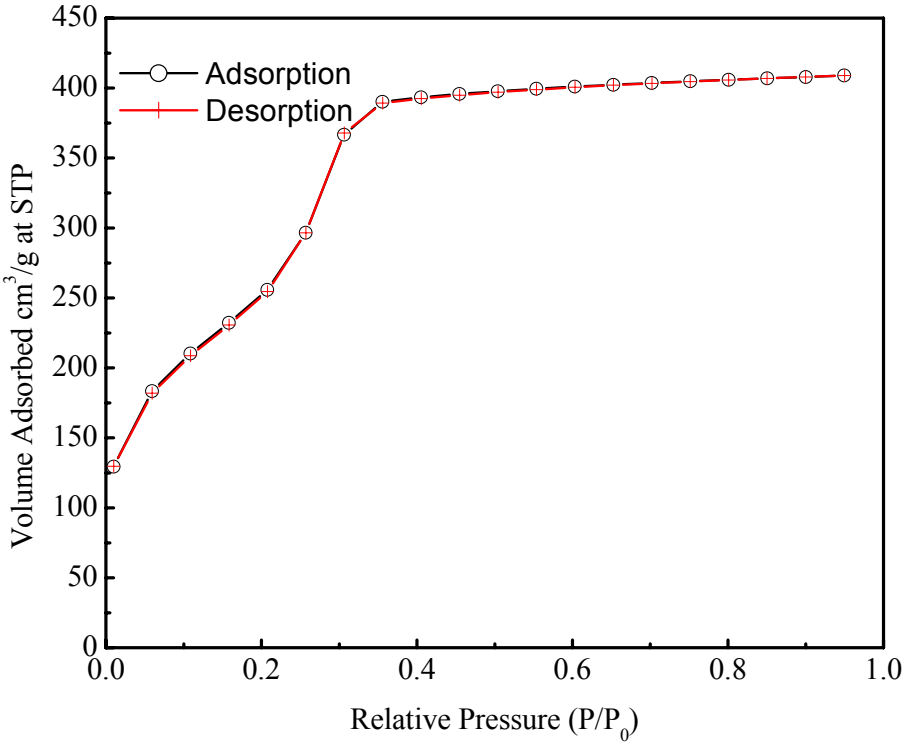


Figure 4.9. Nitrogen adsorption/desorption isotherm from the free-standing film prepared at the molar ratio of water to TEOS of 10 at room temperature.

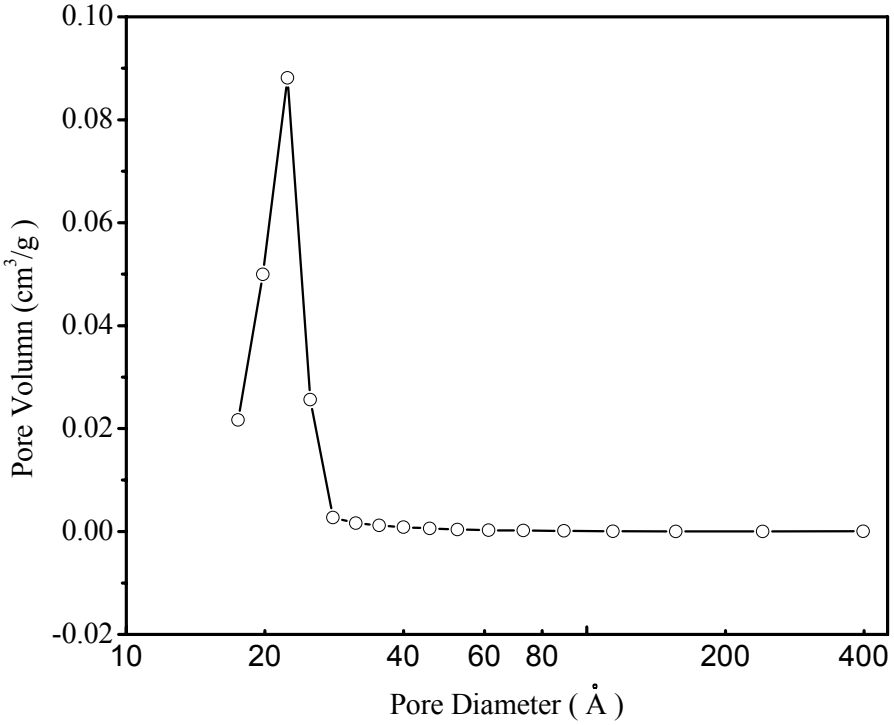


Figure 4.10. BJH Adsorption Pore size distribution from silica monolith.

times from 12.5 ns to 1000 s. The depolarized component of the scattered light is investigated in dynamic light scattering experiments. The static light scattering experiments provide information about the shift of nematic-isotropic phase transition temperature in the confined system compared to the bulk. The dynamic light scattering experiments measure the intensity-intensity autocorrelation function, $g_2(t)$, allowing the relaxation time of fluctuations of director orientations in confined nematic LCs to be obtained.

4.3.1 Light scattering in LCs

After the invention of lasers, light scattering became one of the most powerful tools for investigation of condensed systems. According to the fluctuation theory of light scattering, for conventional fluids, thermal density and concentration fluctuations give rise to inhomogeneities in the dielectric constant and refractive index of the medium. Light scattering is caused by these local inhomogeneities [64].

For LCs, the fluctuations of the order parameter are anomalously large; the intensity of scattered light is frequently stronger than that in conventional fluids by several orders of magnitude [65]. The large optical anisotropy and the large characteristic size of the regular periodic structure are the reasons for the high intensity of light scattering in the nematic phase [66]. In an LC experiment, the situation is also complicated by the fact that the nematic and smectic phases may be either uniaxial or biaxial, meaning that the incident and final momenta are determined by the direction of propagation and the polarization of the light.

Judicious choice of scattering geometry may facilitate different sorts of measurements on the same system.

Two different light scattering methodologies can be used to obtain static and dynamic information of the scattering media; they are called static and dynamic light scattering experiments, respectively. In static light scattering experiments, the time-averaged intensity of the scattered light is measured at different scattering angles. The intensity indicates the amplitude of the fluctuations, and the scattering amgle indicates the size of the fluctuations. In dynamic light scattering experiments, the correlation of light intensity is measured as a function of time, usually at different directions.

The scattering vector **q** is defined as the vector difference between incident and scattered wave vectors:

$$\mathbf{q} = \mathbf{k}_i - \mathbf{k}_f \qquad (4.1)$$

where, $|\mathbf{k}_i| = \frac{2\pi n}{\lambda_i}$ and $|\mathbf{k}_f| = \frac{2\pi n}{\lambda_f}$ are wave vectors specify the directions of propagation of incident and scattered light respectively. In isotropic liquids, we have $|\mathbf{k}_i| = |\mathbf{k}_f|$; then the magnitude of the scattering vector is:

$$|\mathbf{q}| = \frac{4\pi n}{\lambda}\sin\left(\frac{\theta}{2}\right) \qquad (4.2)$$

where n is the refractive index of the medium, λ is the wavelength of the light and scattering angle θ is the angle between $\mathbf{k}_i$ and $\mathbf{k}_f$. **q** has the dimensions of an inverse length, and it sets the length scale which will be probed by the light

scattered at an angle θ. Thus light scattered at a low angle will contain information on the gross dynamic and structural properties of the scatterers, whereas light scattered at high angle contains this information at a finer scale.

It should be note that, Eq. (4.2) is not valid for LCs. Because of the optical anisotropy of LCs, the refractive index depends on the direction of polarization and the wave vector relative to optical axis. Since the magnitude of the wave vector is proportional to the refractive index, the wave vectors $\mathbf{k}_i$ and $\mathbf{k}_f$ typically have different magnitudes, and the scattering wave vector should be evaluated in each specific case in accordance with Eq. (4.1).

The incident plane wave can be expressed as:

$$\mathbf{E}_i(r,t) = \mathbf{i}E_0 \exp i(\mathbf{k}_i \cdot \mathbf{r} - \omega t) \qquad (4.3)$$

where **i** is the unit vector in the direction of the incident electric field, E_0 is the field amplitude, and ω is the angular frequency.

The local dielectric constant of the scattering medium can be expressed by:

$$\boldsymbol{\varepsilon}(\mathbf{r},t) = \varepsilon_0 \mathbf{I} + \delta\boldsymbol{\varepsilon}(\mathbf{r},t) \qquad (4.4)$$

where $\delta\boldsymbol{\varepsilon}(\mathbf{r},t)$ is the dielectric constant fluctuation tensor at a position **r** and time, *t*; **I** is the second rank unit tensor, and ε_0 is the average dielectric constant of the scattering medium.

It can be shown that the magnitude of the scattered electric field, E_s, at a large distance, *R*, from the scattering volume, *V*, with polarization, **f**, and scattered wave vector, $\mathbf{k}_f$, is

$$E_s(R,t)=\frac{E_0}{4\pi R}\exp\left[i\left(k_f R-\omega t\right)\right]\iint_V d^3r\exp\left(i\mathrm{q}\cdot\mathrm{r}\right)\mathrm{f}\cdot\left\{\mathrm{k}_f\times\mathrm{k}_f\times\left[\delta\varepsilon\left(\mathrm{r},t\right)\cdot\mathrm{i}\right]\right\} \quad (4.5)$$

Introducing the spatial Fourier transform of the dielectric fluctuations, Eq. (4.5) can be simplified to:

$$E_s=\frac{k_f^2E_0}{4\pi R}\exp\, i\left(k_f R-\omega t\right)\delta\varepsilon_{if}\left(\mathrm{q},t\right) \quad (4.6)$$

where $\delta\varepsilon_{if}\left(\mathbf{q},t\right)\equiv\mathbf{f}\cdot\delta\varepsilon\left(\mathbf{q},t\right)\cdot\mathbf{i}$.

Then, the average intensity of the scattered light is obtained by Eq. (4.7):

$$I_s\left(\mathbf{q}\right)=\left\langle E_s^*\left(t\right)E_s\left(t\right)\right\rangle=\frac{k_f^4I_0}{16\pi^2R^2}\left\langle\delta\varepsilon_{if}^2\left(\mathbf{q}\right)\right\rangle \quad (4.7)$$

where I_0 is the intensity of the incident light.

Dynamic light scattering experiments are usually performed in homodyne mode for LCs in which only the scattered light impinges on the photocathode. The corresponding normalized time-correlation functions of the scattered field and the scattered intensity are given by:

$$g_1\left(\tau\right)=\frac{\left\langle E_s^*\left(t\right)E_s\left(t+\tau\right)\right\rangle}{\left\langle E_s^*\left(t\right)E_s\left(t\right)\right\rangle} \quad (4.8)$$

and

$$g_2\left(\tau\right)=\frac{\left\langle E_s^*\left(t\right)E_s\left(t\right)E_s^*\left(t+\tau\right)E_s\left(t+\tau\right)\right\rangle}{\left\langle E_s^*\left(t\right)E_s\left(t\right)\right\rangle^2}. \quad (4.9)$$

They are also referred as normalized first- and second-order autocorrelation functions, respectively. These autocorrelation functions obey the

Siergert relation,

$$g_2(\tau) = 1 + |g_1(\tau)|^2 . \quad (4.10)$$

4.3.1.1 Scattering in an isotropic phase

The properties of LCs in the isotopic phase are same as those of conventional organic liquids of anisotropic molecules. The light is scattered because of the fluctuations of the order parameters. Studying the pre-transitional behavior using light scattering as a probe is of primary interest. The I-N phase transition is a weak first order transition, but it behaves like a second-order transition. A huge increase in the intensity of scattered light, an increase in the magnetic birefringence, an anomalous rise of the heat capacity, and a critical retardation of the fluctuations were are observed experimentally in the vicinity of the transition point. These phenomena can be explained by the fact that the there is a small jump in the specific volume, an insignificant heat of transition, and an increase in the fluctuations of the order parameter in the vicinity of phase transition point. Previous study has already shown that the reciprocal of the intensity is proportional to temperature over a wide temperature range; this can be explained by the Landau-de Gennes mean field theory:

$$I_s^{-1}(\mathbf{q}) \propto T - T_{IN}^* \quad (4.11)$$

where T_{IN}^* is the apparent I-N phase transition temperature at which a second order phase transition would occur. The actual first order I-N phase transition usually occurs at temperature $T_{IN} = T_{IN}^* + 1.5K$.

4.3.1.2 Scattering in a nematic phase

Previous experimental results in nematic LCs [67] showed that the light scattering was strong and the scattered light was largely depolarized. In the nematic phase, the molecules in equilibrium align themselves along an average direction denoted by director, $\mathbf{n}_0$. However, thermal fluctuations cause the molecules deviate from this direction both temporally and spatially. These spontaneous thermal fluctuations cause fluctuations in the dielectric tensor which in turn cause the strong light scattering. It should be noted that the light scattering can be also caused by the hydrodynamic modes such as density fluctuations and order parameter fluctuations, but they are much weaker than that caused by orientational fluctuations.

According to the continuum theory, the local director, **n**, is given by:

$$\mathbf{n}(\mathbf{r}) = \mathbf{n}_0 + \delta\mathbf{n}(\mathbf{r}) \tag{4.12}$$

Let x_3-axis be along the direction of $\mathbf{n}_0$, and q be in the $x_1 - x_3$ plane, then $\delta\mathbf{n}$ has only two components $\delta\mathbf{n}_1$ and $\delta\mathbf{n}_2$, and the components of **q** are $q = (q_1, 0, q_3) = (q_\perp, 0, q_\parallel)$where $q_\perp$ and $q_\parallel$ are the scattering vector components perpendicular and parallel to the optic axis, respectively.

It can be shown that the averaged intensity of the scattered light is given by

$$I_s(\mathbf{q}) = \frac{k_f^4 I_0 \varepsilon_\alpha^2}{16\pi^2 R^2} \sum_{\alpha=1,2} (i_\alpha f_3 + i_3 f_\alpha)^2 \left\langle \left| \delta n_\alpha(\mathbf{q}) \right|^2 \right\rangle . \tag{4.13}$$

It is clear that the scattered intensity depends on the mean square amplitude of thermal fluctuations of the two uncoupled eigenmodes represented by $\delta\mathbf{n}_1$ and $\delta\mathbf{n}_2$. These fluctuations are the two Goldstone modes associated with nematic order, and they are related to the three basic types of orientational deformation that are present in a nematic phase, namely splay, twist, and bend as shown in **Figure 4.11**.

Under this specified geometry, the free energy per unit volume, F_N, in the nematic phase can be simplified to

$$F_N = \frac{1}{2}\left\{K_1\left(\partial_1 n_1 + \partial_2 n_2\right)^2 + K_2\left(\partial_2 n_1 - \partial_1 n_2\right)^2 + K_3\left[\left(\partial_3 n_1\right)^2 + \left(\partial_3 n_2\right)^2\right]\right\} \qquad (4.14)$$

where K_1, K_2 and K_3 are the Frank elastic constants for splay, twist and bend, respectively.

Integrating over the illuminated volume, we have:

$$\int_V F_N d\mathbf{r} = \frac{1}{2}\sum_q \left[\left(K_1 q_\perp^2 + K_3 q_\parallel^2\right)\delta n_1^2(\mathbf{q}) + \left(K_2 q_\perp^2 + K_3 q_\parallel^2\right)\delta n_2^2(\mathbf{q})\right] \qquad (4.15)$$

By applying the equipartition theorem, we have:

$$\left\langle \left|\delta n_1(\mathbf{q})\right|^2 \right\rangle = \frac{k_B T}{K_1 q_\perp^2 + K_3 q_\parallel^2}, \qquad (4.16)$$

$$\left\langle \left|\delta n_2(\mathbf{q})\right|^2 \right\rangle = \frac{k_B T}{K_2 q_\perp^2 + K_3 q_\parallel^2}. \qquad (4.17)$$

As can be seen from Eqs. (4.16) and (4.17), the first mode associated with $\delta\mathbf{n}_1$ is a combination of splay and bend distortions, while the second mode associated with $\delta\mathbf{n}_2$ is a combination of twist and bend distortions. When the

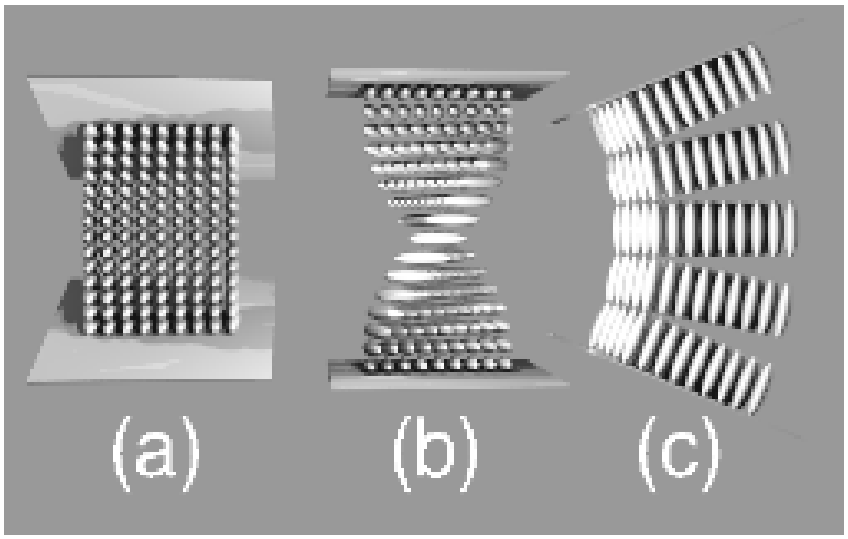


Figure 4.11. Elastic distortions of a nematic LC: (a) splay (b) twist (c) bend [68]

scattering vector is along the direction of $\mathbf{n}_0$, the two modes are degenerate and only the bend fluctuations are present.

As a result, the average intensity of the scattered light can be written in a generalized form:

$$I_s(\mathbf{q}) = \frac{k_f^4 I_0 \varepsilon_\alpha^2 k_B T}{16\pi^2 R^2} \sum_{\alpha=1,2} \frac{(i_\alpha f_3 + i_3 f_\alpha)^2}{K_\alpha q_\perp^2 + K_3 q_\parallel^2}. \tag{4.18}$$

A suitable choice of the direction of the scattering vector, **q**, and the polarization, **i** and **f** allows us to study the Frank elastic constants individually. For example, the polarization, **i** and **f** are chosen to be normal to and in the scattering plane respectively. As shown in **Figure 4.12** (a), the scattering plane is normal to the optical axis, and **q** is perpendicular to $\mathbf{k}_f$. The scattered intensity is given by:

$$I_s(\mathbf{q}) = \frac{k_f^4 I_0 \varepsilon_\alpha^2 k_B T}{16\pi^2 R^2 K_1 q^2}, \tag{4.19}$$

which depends only on the splay elastic constant K_1.

If the optical axis is in the scattering plane and q is normal to both $\mathbf{k}_i$ and the optical axis, as shown in **Figure 4.12** (b), the twist elastic constant K_2 can be obtained by:

$$I_s(\mathbf{q}) = \frac{k_f^4 I_0 \varepsilon_\alpha^2 k_B T f_3^2}{16\pi^2 R^2 K_2 q^2}. \tag{4.20}$$

If the optical axis is also in the scattering plane, and q is chosen to be normal to $\mathbf{k}_i$ but parallel to the optical axis, as shown in **Figure 4.12** (c), the scattered intensity

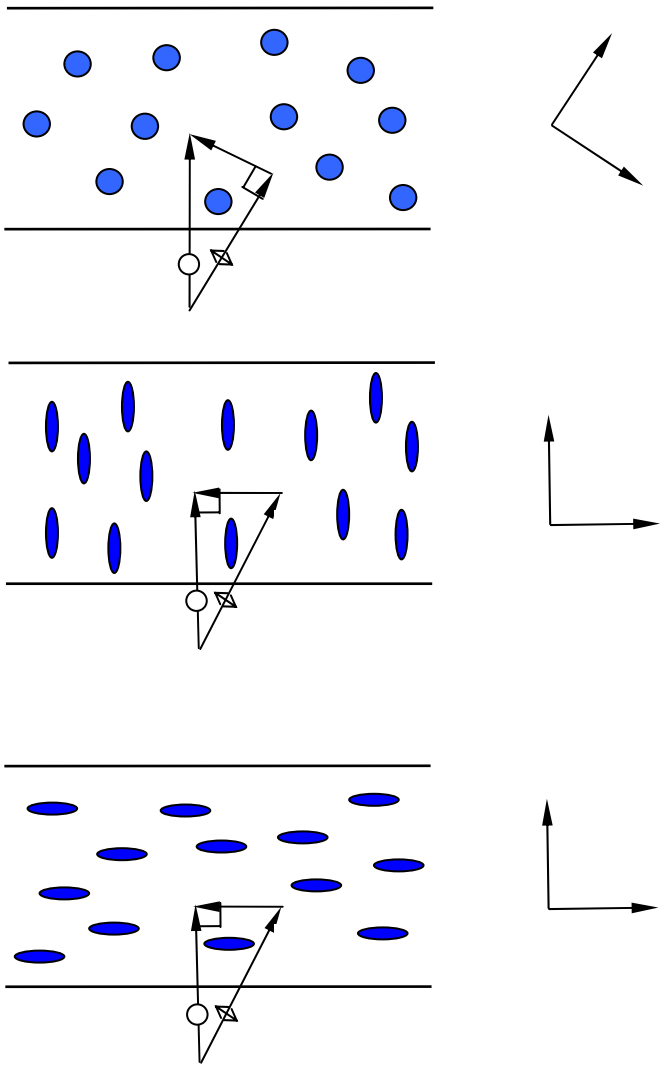


Figure 4.12. Light scattering geometries for the (a) splay, (b) twist and (c) bend modes.

is simplified to

$$I_s(\mathrm{q}) = \frac{k_f^4 I_0 \varepsilon_\alpha^2 k_B T f_3^2}{16\pi^2 R^2 K_3 q^2}. \tag{4.21}$$

In this case, the bend elastic constant K_3 can be determined.

As the intensity of scattered light reveal the behavior of the Frank elastic constants, more information about the viscosity coefficient can be extracted from the frequency spectrum of the scattered light. In LCs, the transitional motions are coupled to the orientational motions of molecules. In order to study the dynamics of a LC, new transport parameters corresponding to the director field $\mathbf{n}(\mathbf{r},t)$ should be included in addition to those corresponding to velocity field that are used in ordinary fluids. Many viscosity coefficients have been defined for a uniform incompressible nematic crystal. According to the macroscopic approach proposed by Ericksen [69, 70], Leslie [71, 72], and Parodi [73], only five are independent. The commonly used ones are the Liesowicz viscosities η_a, η_b and η_c, the Leslie coefficients α_1, α_2, α_3, etc., and the twist viscosity γ_1.

The relaxation rate for the two modes mentioned above can be expressed by:

$$\Gamma_1(\mathbf{q}) = \frac{K_1 q_\perp^2 + K_3 q_\parallel^2}{\eta_1(\mathbf{q})} \tag{4.22}$$

and

$$\Gamma_2(\mathbf{q}) = \frac{K_2 q_\perp^2 + K_3 q_\parallel^2}{\eta_2(\mathbf{q})}, \tag{4.23}$$

where $\eta_1(\mathbf{q})$ and $\eta_2(\mathbf{q})$ are effective viscosities defined by

$$\eta_1(\mathbf{q}) \equiv \gamma_1 - \frac{\left(\alpha_3 q_\perp^2 - \alpha_2 q_\parallel^2\right)^2}{\eta_b q_\perp^4 + (\alpha_1 + \alpha_3 + \alpha_4 + \alpha_5) q_\perp^2 q_\parallel^2 + \eta_c q_\parallel^4},$$

$$\eta_2(\mathbf{q}) \equiv \gamma_1 - \frac{\alpha_2 q_\parallel^2}{\eta_a q_\perp^2 + \eta_c q_\parallel^2}.$$

Similarly, by properly choosing the scattering geometry as mentioned above, we can study the dynamics of a specific Frank elastic distortion. A singe splay-mode relaxation rate is

$$\Gamma_{splay}(\mathrm{q}) = \frac{K_1 q^2}{\gamma_1 - \alpha_3^2/\eta_B}; \tag{4.24}$$

a singe twist-mode relaxation rate is

$$\Gamma_{twist}(\mathbf{q}) = \frac{K_2 q^2}{\gamma_1}; \tag{4.25}$$

and a single bend-mode relaxation rate is

$$\Gamma_{bend}(\mathbf{q}) = \frac{K_3 q^2}{\gamma_1 - \alpha_2^2/\eta_C}. \tag{4.26}$$

If we assume the five viscosity coefficients are of the same order of magnitude and are denoted by η (η is an average viscosity), and the three elastic constant are equal $(K_1 = K_2 = K_3 = K)$, then the relaxation time of director fluctuation is

$$\tau(T) = \frac{\eta(T)}{K(T) q^2} \tag{4.27}.$$

Therefore the variation of relaxation time with temperature is determined by the ratio of η to K.

4.3.1.3 Scattering in a Smectic A phase

In a smectic A phase, a layered structure with one-dimensional positional order along the director vector, $\mathbf{n}_0$, is formed. The layer spacing is given by

$$d = \frac{2\pi}{q_0}.$$

Two different modes give rise to director fluctuations in a smectic A phase. One is associated with deviations of the local director from the normal to the layer (so-called tilt mode), the other is related to a change of the layer thickness in the direction of the normal to the layer (the dilation mode). B and D are the elastic constants related to the restoring forces against deviations from uniformity in the layer thickness and against the molecular orientation pointing away from the normal to the layers, respectively. If the mean field theory is applicable, B and D should show linear temperature dependence near the N-SmA phase transition:

$$B \propto \left(T_{NA} - T\right),$$

$$D \propto \left(T_{NA} - T\right).$$

If deviation from the mean field and the presence of anisotropy are taken into account, the elastic constants, B and D, should have the following temperature dependence:

$$B \propto \left(T_{NA} - T\right)^{2\nu_\perp - \nu_\parallel},$$

$$D \propto \left(T_{NA} - T\right)^{\nu_{\|}}.$$

In principle, B and D can be measured relative to the Frank constants using a static light scattering method and relative to the viscosities using dynamic light scattering. Anisotropy in the critical behavior and an apparent absence of universality among the measured critical exponents have been observed for most materials.

The nematic-smectic A (N-A) phase transition is a second order phase transition in general, and most materials do not exhibit mean field behavior near the N-SmA transition. Our understanding of the critical phenomena near the N-SmA transition is still not complete.

Bend and twist distortions are excluded in the presence of a SmA phase. Therefore, near the N-SmA transition, a pre-transitional increase in the bend and twist elastic constant will be observed; the values of bend and twist elastic constants, K_2 and K_3, are expected to be enhanced above their normal values, K_2^0 and K_3^0, in the absence of the N-SmA transition:

$$K_2 = K_2^0 + \delta K_2$$

$$K_3 = K_3^0 + \delta K_3.$$

The increase in K_2 and K_3 are related to the size of the short range smectic-like clusters in the nematic phase, which grow as the N-SmA transition is approached. δK_2 and δK_3 can be represented by:

$$\delta K_2 \propto \xi_{\perp}^2 / \xi_{\parallel} \propto \left(T - T_{NA}\right)^{-\left(2\nu_{\perp} - \nu_{\parallel}\right)}$$

and

$$\delta K_3 \propto \xi_{\parallel} \propto \left(T - T_{NA}\right)^{-\nu_{\parallel}}$$

where $\xi_{\parallel}$ and $\xi_{\perp}$ are the SmA correlation length parallel and perpendicular to the normal to the layers respectively, and $\nu_{\parallel}$ and $\nu_{\perp}$ are corresponding critical exponents.

An increase in K_2 and K_3 would reduce the amplitude of the director fluctuations which in turn would decrease the intensity of scattered light in the vicinity of the N-SmA transition. Previous static light scattering results have established that the critical divergence in K_3 is generally stronger than that in K_2, which suggests an anisotropy in the behavior of the longitudinal and transverse correlation lengths. The critical exponents for δK_2 and δK_3 are found to be around 0.5 and 0.7 respectively, but no universality in the values of the critical exponents for different materials is found. A complete theoretical explanation for these results is still unavailable.

The dynamic behavior of LCs was also investigated in some experiments [74-77]. The twist viscosity γ_1 was the most well studied quantity by both dynamic light scattering and dynamic Frederiks deformation techniques [78, 79]. However, the question of whether the critical behavior should be mean field or non-mean field behavior has not been fully resolved.

4.3.2 Experimental setup

The DLS experimental setup contains the following components as shown in **Figure 4.13**:

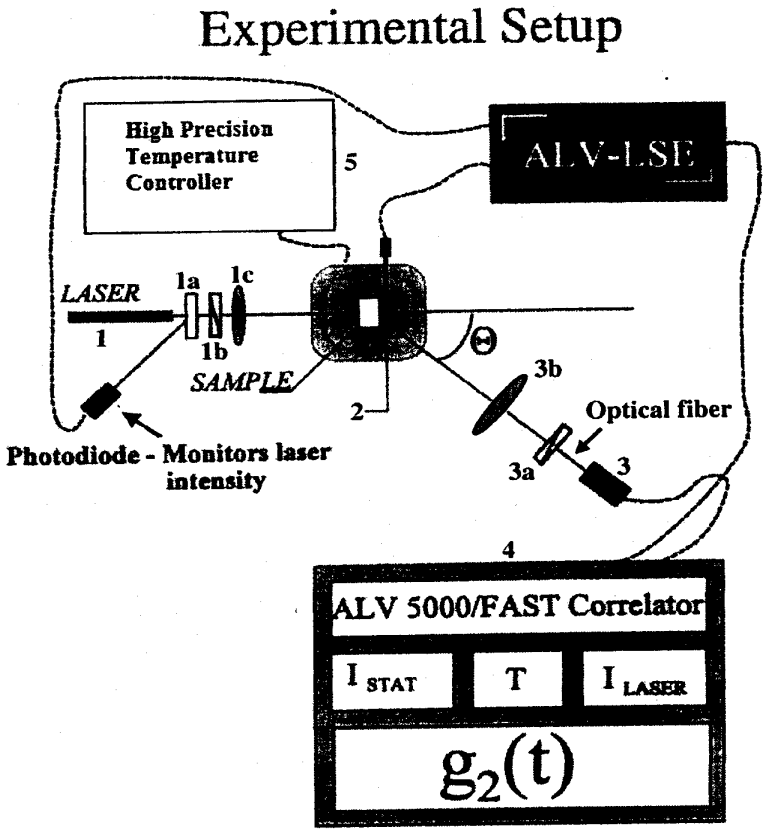
The incident laser light source and associated optics

Light scattering cell in the thermostat

Photon detection system with single mode fiber

ALV-5000 multi tau digital correlator with 256 channels connected to a PC used to obtain the intensity time autocorrelation function in the real time Digital temperature controller from PolyScience allowing the temperature to be set from $-10°C$ up to $100°C$ with a stability of $\pm 0.05°C$

A Melles Griot He-Ne laser tube was used to generate a continuous gas laser source with output power of 15mW and a wavelength of 632.8 nm, which could provide a plane-polarized incident beam with enough intensity for both static and dynamic light scattering experiments. The incident beam becomes vertically polarized to the scattering plane as it passes through the Gland-Thomson prism. After that the incident is focused on the middle of the sample located in the thermostat with the aid of the focusing lens. The thermostat is a hollow copper cylinder with an open-end in the upper side so that a metallic cell can be fitted in. The sample was mounted on the sample holder inside this metallic cell. The thermostat and the metallic cell have windows in them, which allow the vertically polarized incident beam to fall on the sample and the scattered light to be collected at different scattering angles. A fluid continuously circulating



1 - laser; 1a - Beam splitter; 1b, 3a - Polarizer; 1c, 3b - Lenses;

2 - Thermostat; 3 - Photon detection system with single mode optical fiber;

4 - ALV-LSE: light scattering electronics; 5 - Temperature controller.

Figure 4.13. Setup of the computer controlled dynamic light scattering experiments.

through the hollow portion of the thermostat is used to control the experimental temperature in the cell. A box made of plastic foam is also used to minimize heat exchange with the ambient. In this way, the temperature inside the sample cell could be controlled with an accuracy of $\pm 0.01°C$. A digital temperature controller is used to maintain or change the temperature of the fluids which in turn keep the sample cell at the set temperature. A temperature probe is positioned very close to the sample which gives the temperature readout of the sample. The time required to reach stabilization is about 20 minutes. The photo detection system consists of a photomultiplier tube (PMT), a pulse amplifier-discriminator, and a single mode optical fiber. A Thorn EMI photo-multiplier tube (type QL30F15/RFI) with PM28B power supply was used for our experiments. Since the gain of the PMT varies dramatically with the PMT voltage, the voltage fluctuations of the power supply must be reduced to a minimum. A PM28B power supply was used in our experiments to satisfy the requirement of tight regulation of voltage.

The output of the PMT is connected to the amplifier discriminator with a short and rigid connector in order to reduce noise from electronics. The overall gain of the amplifier discriminator is on the order of magnitude of 1000 or more, which might result in a spurious pulse and correlation. The photo-electron pulse, after careful amplification and discrimination, were fed into a digital correlator to obtain the intensity-intensity autocorrelation function.

An ALV-5000/FAST real time digital correlator was used in our

experiments to obtain the intensity-intensity autocorrelation function. The intensity of scattered light $I_s(t)$ obtained at time t is correlated to the intensity of scattered light $J_s(t+\Delta t)$ obtained at $(t+\Delta t)$ by this correlator. The autocorrelation function is defined as:

$$G(t) = \lim_{x\to\infty}(1/2\pi)\int_{-T}^{T} I_s(t)J_s(t+\Delta t)dt \qquad (4.28)$$

where $G(t)$ is called autocorrelation function or cross-correlation function depending on whether $I_s(t)$ and $J_s(t+\Delta t)$ are the same or different signals. The ALV-5000 digital correlator board (dimension: $340mm \times 120mm$, full-size AT board) turns PC/XT-AT compatible computers into state-of-art signal processors, ideally suited for photon correlation experiments. Signals are processed into a complete set of simultaneous correlation channels with a maximum input count rate of more than 100 MHz in real time. It has 280 digital real time correlation channels with fixed sampling time grid ranging from $0.2\mu s$ (single mode) or $0.4\mu s$ (dual mode) up to $2.7\times10^{10}\ \mu s$ in lag time. The width of the sampling interval is increased in proportion to the lag time to ensure optimum statistical accuracy. The dual correlation mode allows computing two independent correlation functions of two different input signals simultaneously. Cross-correlation functions may be computed as well as auto-correlations. With the ALV-5000/FAST Tau addition, the number of channels increases for the fast correlation mode to 320, with an initial lag time of 12.5 ns.

The ALV-5000/FAST Correlator Software allows full correlator control and real time display of all correlation experiment relevant data. Most major commands and pull-down menus are accessible by the function keys which provide fast and convenient interactive user control. Meanwhile, all commands are also accessible through short ASCII command words, in some cases followed by a numeric or a text string type argument. They are used to control the correlator setups, windows setups, data reductions, printer output and communication with temperature controller etc. Correct operation can be ensured by wisely selecting the control parameters such as overflow stop, auto-scaling, auto-saving of data, and so on. Context sensitive help-screens provide individual explanations for each command. A special error message window can help the user to locate to source of a problem quickly.

The intensity-intensity autocorrelation function is given by:

$$g_2(t) = \frac{\langle I(t)I(t+\Delta t)\rangle}{\langle I(t)^2\rangle}. \qquad (4.29)$$

The intensity-intensity autocorrelation function $g_2(t)$ can be converted to the field-field correlation $g_1(t)$ by:

$$g_2(t) = B + A|g_1(t)|^2 \qquad (4.30)$$

where $g_1(t) = \frac{\langle E(t)E^*(t+\Delta t)\rangle}{\langle E(t)E^*(t)\rangle}$, B is the base line, and A is a coherence factor that depends on signal to noise ratio and is generally of order 1.

A single mode optical fiber receiver is used in our experiments to get the best signal to noise ratio. The receiving lens integrated with the fiber was placed 90 cm away from the scattering center at different scattering angles. The other end of the single mode optical fiber is integrated with the output lens connected to the PMT. It can also collect the scattered light from the first coherence zone, and the signal to noise ratio is very close to theoretical limit for the bulk LCs.

4.3.3 DLS data analysis

Useful dynamic information about LCs such as characteristic relaxation times of different decay processes can be obtained by fitting the measured autocorrelation function with certain decay functions. Clearly, different physical processes cannot be explained by a single form. Therefore, the first step in data analysis is the selection of the right theoretical form expected in the correlation function. If the measured autocorrelation function includes only one relaxation process, the normalized electric field autocorrelation function has the form:

$$g_1(t) = \alpha \exp\left(\frac{-t}{\tau}\right) = \alpha \exp(-t\Gamma) \tag{4.31}$$

where τ is the relaxation time of the process and $\Gamma = \tau^{-1}$ is the decay rate.

Then, the corresponding normalized intensity autocorrelation function is:

$$g_2(t) = A \exp\left(\frac{-2t}{\tau}\right) + B \tag{4.32}$$

where A is the amplitude of the autocorrelation function and an instrument constant, B is the base line.

The relaxation time τ can be obtained by fitting the measured autocorrelation function with $g_2(t)$ using either a linear or a nonlinear method. If the baseline is well defined, then the linear method provides the simplest way to determine τ . By rearranging Eq.(1.30), we have:

$$\ln[g_2(t) - B] = \ln A - (2/\tau)t \qquad (4.33)$$

The experimental data can be fitted with above linear equation, and the relaxation time τ and the amplitude A can be obtained from the slope, $-2/\tau$, and the intercept, $\ln A$, respectively.

If the base line is not well defined, the nonlinear fitting method should be used. Also, if the contrast is very low $(A \to 0)$, the value of $g_2(t)$ is very close to B. In this circumstance, the data points become more spread, which in turn introduces more uncertainty in determination of the fitting parameters. Therefore, the linear fitting method should be used carefully.

If the decay function can not be described by single exponential function but by the stretched exponential function, or if more than one exponential decay process is present in the system, nonlinear fitting method should be used.

In our experiments, two different relaxation processes are observed in the autocorrelation function due to the confinement effects. Thus, we used the nonlinear fitting method for data analysis. The intensity-intensity autocorrelation function $g_2(t) - 1$was fitted by a double stretched exponential function with the help of the nonlinear least squares fitter in Origin. Origin's nonlinear least squares

fitter allowed us to take almost full control of the fitting process by selecting the best initial parameter values by plotting the curve before the actual fitting and comparing it to the data and imposing linear constraints on the values of parameters.

Confinement has a nontrivial effect on the condensed matter system due to the surface interaction, induced disorder, and finite size effects. Different techniques such as calorimetric measurement, dielectric spectroscopy, dynamic light scattering, and X-ray scattering as well as quasi-elastic neutron scattering have been widely used to study this important topic. Numerous experimental results have revealed that the physical properties of condensed matter in confined geometry are strikingly different from the bulk values. However, inconsistencies still exist among the theoretical predictions, experimental observations, and the results of computer simulations because of the complexity of the systems.

Studies of the influence of confinement on physical properties are particularly important for LC systems. LCs are soft systems that exhibit intermediate thermodynamic phases between the crystalline solid and simple liquid state, and they possess orientational or weak positional order and thus reveal several physical properties of crystals but flow like liquids. Their weak oriental and positional order are strongly influenced by the presence of a surface. Porous matrices, with extensive surface-LC contact area, have a more significant effect on the ordering, structure, and phase transitions of LCs. At the same time the long-range correlation near phase transitions and the presence of phase

transition of different order also made LCs rich systems to be studied in confined geometry.

Both surface effects and finite size effects will affect the dynamics of LCs in confinement. On the one hand, the confinement will break the symmetry of bulk LC phase and change viscosity, which, in turn, will change the dynamic properties of LCs. On the other hand, the pore wall will induce a polar order for the polar LC molecules that will result in a gradient of the order parameter and inhomogeneity of orientation.

Previous studies have shown that restricted geometry has a significant effect on the ordering, structure, and phase transitions of nematic LCs and on the isotopic phase of LCs. The dynamics of confined LCs and the second order phase transition have also been studied by different techniques.

4.4 Dielectric Spectroscopy

Dielectric spectroscopy (DS) is a powerful technique that can be used to study the confinement effect on the dynamic behavior of liquid crystals (LCs). It probes the relaxation due to the reorientations of polar molecules in the sample. Broad band dielectric spectroscopy can be applied for investigations of the dynamic behavior of liquid crystals in the isotropic, nematic, and smectic phases confined in porous matrices of different pore sizes.

DS measurements are performed using a broadband dielectric

spectrometer based on the Schlumberger Technologies 1260 Impedance/Gain-phase Analyzer, Novocontrol Broad Band Dielectric Converter with an active sample cell and Hewlett Packward 4291A RF Impedance Analyzer.

For bulk LCs, the dielectric relaxation process is of Debye type, which has a single relaxation time. Debye function is used to describe the relaxation process:

$$\varepsilon^* = \varepsilon_\infty + \frac{\varepsilon_s - \varepsilon_\infty}{1 + i\omega\tau} \tag{4.34}$$

where ω is the circular frequency $(\omega = 2\pi f)$ of the alternating field, ε_s is the static permittivity, ε_∞ is the permittivity at infinite frequency, and τ is the macroscopic relaxation time.

For confined LCs, relaxation processes are of non-Debye type, which have a distribution of relaxation times. The Havriliak-Negami [80] function is used to analyze the dielectric spectra quantitatively:

$$\varepsilon^* = \varepsilon_\infty + \sum_j \frac{\Delta\varepsilon_j}{\left[1 + \left(i2\pi f\tau_j\right)^{1-\alpha_j}\right]^{\beta_j}} - i\frac{\sigma}{2\pi\varepsilon_0 f^n}, \tag{4.35}$$

where ε_∞ is the high-frequency limit of the permittivity, $\Delta\varepsilon_j$ is the dielectric strength, τ_j is the mean relaxation time, and *j* is the number of the relaxation process. The exponents α_j and β_j describe the symmetric and asymmetric distribution of the relaxation times. The term $i\sigma/2\pi\varepsilon_0 f^n$ accounts the contribution of conductivity σ, with *n* as the fitting parameter. In the case of pure ohmic conductivity *n* = 1. If electrode polarization also contributes to the

imaginary part of dielectric permittivity ε'', then *n* is less than 1.

4.4.1 Dielectric properties of liquid crystals[81]

Dielectric properties measure the response of a charge-free system to an applied electric field and are a probe of molecular polarizability and dipole moment. The dielectric behavior of liquid crystals reflects the collective response of the mesogens as well as their molecular properties, and there is a coupling between the macroscopic polarization and the molecular response through the internal electric field.

In liquid crystal, the electric permittivity becomes a second rank tensor $\varepsilon_{\alpha\beta}$, and an electric susceptibility can be defined as:

$$\chi_{\alpha\beta}^{electric} = \frac{P_\alpha}{\varepsilon_0 E_\beta} = \frac{P_\alpha}{\varepsilon_0\left(\varepsilon_{\alpha\beta} - \delta_{\alpha\beta}\right)} \ . \tag{4.36}$$

where **P** is the induced polarization, **E** is the applied electric field and ε_0 is the permittivity of free space. Thus, the number of independent components of the permittivity tensor will depend on the symmetry of the liquid crystal phase. The frequency dependence of the permittivity also will be tensor quantities.

In an isotropic fluid, the dielectric relaxation of a rigid dipolar molecule is a single relaxation process, while in a liquid crystal phase, the rotational motion of a rod-like mesogen is no longer isotropic, and two rotational diffusion constants are needed to describe the process. They are parallel and perpendicular to the unique inertial axis respectively. Thus, an isotropic rotational model should be used to describe the dielectric response.

The electric permittivity of liquid crystals is frequency dependent and the origin of the frequency dependence is molecular motion associate with a dipole moment. According to Kramers-Krong relation, both the real and imaginary parts of the permittivity are frequency dependent and can be expressed as:

$$\varepsilon_i(\omega)' = \varepsilon_i(\infty)' + \frac{2}{\pi}\int_0^\infty \frac{\omega\varepsilon_i(\omega)''}{\left(\omega^2-\omega_0^2\right)}d\omega \tag{4.38}$$

$$\varepsilon_i(\omega)'' = \frac{2\omega_0}{\pi}\int_0^\infty \frac{\varepsilon_i(\omega)'}{\left(\omega^2-\omega_0^2\right)}d\omega\,. \tag{4.39}$$

where the integral excludes the singular point at $\omega = \omega_0$.

For a uniaxial liquid crystal, the effects of induced moments can be removed by subtracting the high frequency part of the permittivity ot square of the refractive index. The real parts of the permittivity are given by:

$$\varepsilon_{\parallel}(\omega) - n_{\parallel}^2 = \frac{NLF^2 g_1^{\parallel}}{3\varepsilon_0 k_B T}\left[\mu_1^2(1+2S) + \mu_t^2(1-S)\right] \tag{4.40}$$

$$\varepsilon_{\perp}(\omega) - n_{\perp}^2 = \frac{NLF^2 g_1^{\perp}}{3\varepsilon_0 k_B T}\left[\mu_1^2(1-S) + \mu_t^2\left(1+\frac{1}{2}S\right)\right] \tag{4.41}$$

Each components of $\varepsilon(\omega)'$ contains two contributions from molecular dipole moments, and each have different relaxation frequencies. The characteristic relaxation frequencies are related to the rotational motion of a molecule in an anisotropic environment. For a uniaxial molecule with two independent moments of inertia, the rotational motions can be assumed to have three different modes: end-over-end rotation (ω_1), precessional motion (ω_2), and

rotation about its own long molecular axis (ω_3). In a nematic environment, the magnitudes of the characteristic frequencies for the rotational frequencies is in the order $\omega_1 << \omega_2 < \omega_3$. Contributions to the permittivity will be lost above frequencies corresponding to $\omega_1, \omega_2, \omega_3$, and the variation of $\varepsilon_{\parallel}(\omega)^*$ and $\varepsilon_{\perp}(\omega)^*$ with frequency is shown in **Figure 4.14**. Experimental measurements of dielectric relaxation conform qualitatively the predictions of the rotational diffusion model. $\varepsilon_{\parallel}$ has both high and low frequency relaxation, while $\varepsilon_{\perp}$ only has low frequency relaxation.

Temperature is an important variable that affects the dielectric relaxation, and it is found that relaxation times decrease as the temperature increases. If rotational diffusion is an activated process, then Arrhenius equation can be used to express the relaxation time:

$$\tau = A \exp \frac{E_a}{k_B T} \qquad (4.42)$$

where E_a is the activation energy or barrier to dipole rotation, A is another parameter of the model. Experiments established that the activation energies for dipole reorientation often change at LC phase transitions due to the difference in the degree of order and local viscosity. The activation energies are expected to be higher in smectic phase. However, it is often observed that the end-over-end rotation has a lower activation energy in the smectic A phase than in the higher temperature nematic phase, this casts some doubt on the role of the order

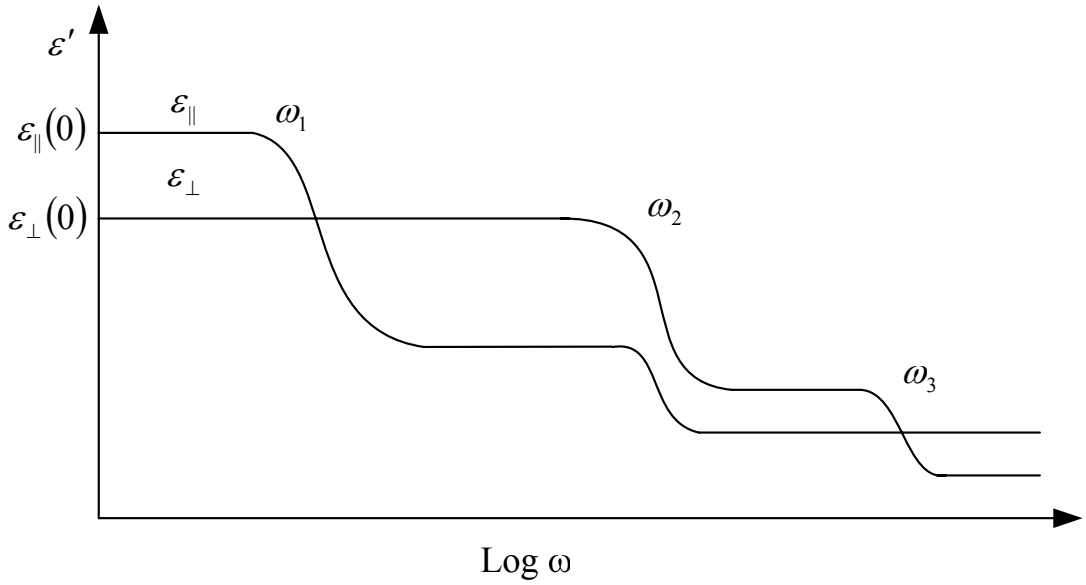


Figure 4.14. Schematic plot of $\varepsilon_{\parallel}'$ and $\varepsilon_{\perp}'$ against frequency

parameter and viscosity, which are both higher in smectic phase than the nematic phase. A free –volume model due to Vogel and Fulcher was used to explain the results for τ measured for nematic and SmA phase. The relaxation time is expressed by:

$$\tau = B\exp\frac{E_a}{k_B(T - T_0)} \quad . \qquad (4.43)$$

Thus, the relaxation frequencies decrease by nearly a decade on going from the nematic phase to the smectic phase, but the activation energies are approximately the same.

4.4.2 Experimental equipments

Broadband dielectric spectroscopy is an ideal technique that can be used to explore dielectric relaxation processes in the frequency range from 10^{-5} ~10^{9} Hz. This frequency range covers all molecular and collective mode motions of liquid crystals.

In a real experiment, one measures the frequency dependent real (ε') and imaginary (ε'') parts of complex dielectric permittivity $(\varepsilon^* = \varepsilon' - i\varepsilon'')$ as a function of temperature, time and DC bias to evaluate the different physical quantities.

The broadband dielectric spectrometer consists of the following components (see **Figure 4.15**)[82]:

The Schlumberger Technologies Impedance/Gain-Phase(SI) 1260 Analyzer

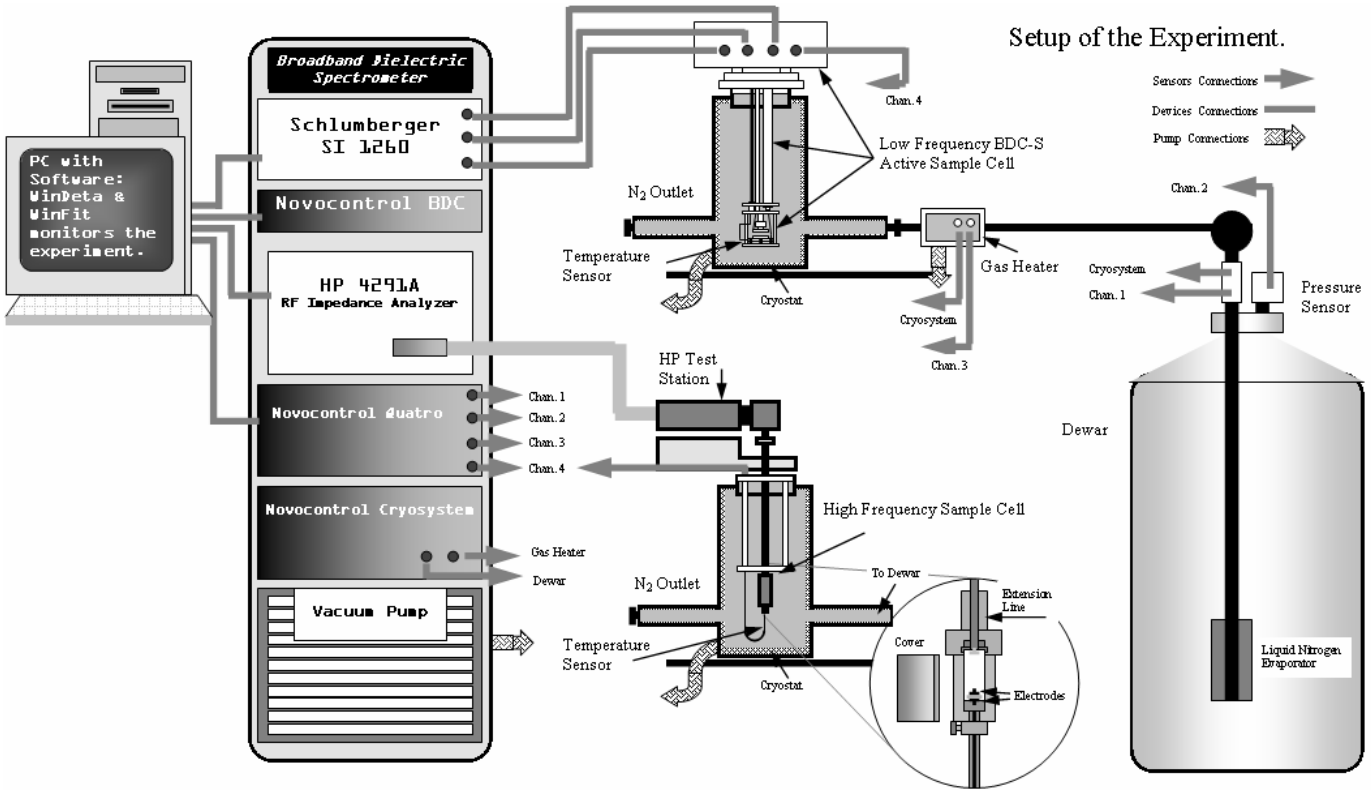


Figure 4.15. Experimental setup of the computer controlled broadband dielectric spectrometer.

Novocontrol Broad Band Dielectric Converter(BDC-S)

Active sample cell with sample holder, sample capacitor and reference capacitors

Hewlett-Packard 4291A re Impedance Analyzer

A rf sample cell with the sample capacitor

A high precision microwave extension line connecting the sample cell to the impedance analyzer

Quatro temperature control system

PC with the MS-Windows software package WinDETA and WINFIT that controls the measurement flow, operates all devices and evaluates the measured data

Novocontrol Broadband Dielectric Converter BDC and Solartron SI 1260 are used for low frequency test. This device combination allows us to measure the impedances from 10 $Ohms$ to 200 $TOhms$ with a resolution in loss factor $\tan(d) < 0.1 mrad$. The frequency range is from $10 \mu Hz$ to $10 MHz$. The SI 1260 is a two-channel vector voltage meter. A vector voltage analyzer measures the amplitude and phase of a harmonic ac voltage V_s directly using two signal channels, BDC-S is used to avoid the contribution of inductive impedance of the BNC cables connecting the sample holder with the analyzer, especially at low frequencies. The second voltage channel of SI 1260 is used instead of the current channel. The current to voltage conversion is done in the active sample cell of the

BDC, with an amplifier handling impedance up to $2\times10^{14}\Omega$. The current to voltage converters, the reference capacitors and an additional current buffer amplifier are mounted on the top of the sample holder in the sample cell and connected by air-insulated solid lines to the sample capacitor in order to get better performance in the frequencies around 1*MHz*. The sample cell fits directly into the cryostat for temperature control of the sample. The sample is mounted between two gold plated parallel round plates and placed in the shielded cell.

Impedance Analyzer Hewlett Packard 4291 used for high frequency test can measure the impedances from $0.1\ Ohms$ to $50\ kOhms$ with a resolution in loss factor $\tan(d) < 2mrad$. The frequency range is from $1MHz$ to $1.8GHz$. Above 10 *MHz* coaxial connecting cables always bring errors to the impedance measurements. Above 30 *MHz* additional standing waves arise at the line made a direct measurement of the sample impedance impossible. HP 4291 based on microwave techniques can achieve this goal by taking the measurement line as the main part of the measured impedance. A coaxial precision line with defined and nearly temperature independent propagation constants is used to connect the analyzer test head to the sample cell. The microwave signal of the analyzer is transmitted through the material under test and the magnitude and phase of the reflected signal is measured by the analyzer.

Novocontrol Quatro Cryosystem consists of the quartro temperature controller BDS 1340, a cryostat BDS 1100 in which the sample cell BDS 1200 fits in, a gas heating module BDS a320, a liquid nitrogen dewar with pressure

sensor and a vacuum system. The liquid nitrogen evaporator heats the liquid nitrogen until a specified pressure in the dewar is reached. Channels 1 and 2 of the Quarto controller control the actual pressure. The pressure is automatically adjusted according to the set value of the sample temperature. The cold liquid nitrogen flow out of the dewar through the gas jet to the cryostat. In the case of heating experiment, dried and purified air is supplied by a JUN-AIR compressor set at 80-120 psi. Humidity and CO_2 are removed by a Balston filter by 99%. The purified air is fed through the gas heater to the cryostat. The gas jet is controlled by channel 3 and 4 of the Quatro controller in order to match the actual temperature at the sample cell to the specified temperature point. The flow of either evaporated liquid nitrogen or dried heated air keep the sample chamber away from humidity. Due to the high stability of the gas pressure, and the two-circuit arrangement of the gas heating, the temperate can be controlled between $-150^{\circ}C$ and $+500^{\circ}C$ with a high precision of $0.01^{\circ}C$.

4.4.3 Experimental procedure

4.4.3.1 Setting up a measurement

Select the appropriate device configurations from the **Analyzer** menu. **Novocontrol BDC + Solatron SI 1260** and **Hewlett Packard 4291** are for the low and high frequency tests respectively.

Select the temperature controller **Quatro Version >= 4.0** from the **Temp. Controller** menu.

4.4.3.2 Running a measurement

Select Sample **Specification** from the **measurement** menu in order to enter a comment to the measurement. Fill in the sample size and sample thickness.

Select **Averaging** from the **Measurement** menu, set to average over 300 points in a given frequency interval.

Select **List Order** from the **Measurement** menu in order to define which of the independent variables will be used in the measurement and their execute order. Add **Frequency** and **Temperature** in the lists.

Select **Value List** from the **Measurement** menu to enter values in all lists defined in the **List Order** dialogue. For this purpose, choose **Standard Frequency List** from the sub-menu **frequency.** Generate temperature value list from the submenu **Temperature** according to the following rules: start at temperature about $20^{\circ}C$ away from the phase transition point; keep the temperature increment at $2^{\circ}C$. After three or four temperature points, change the temperature increment to $1^{\circ}C$ and in the vicinity of the phase transition $\left(T_C \pm 2^{\circ}C\right)$, change the temperature increment to $0.2^{\circ}C$.

Select Start from Measurement menu.

4.4.4 Calibration

In order to perform high frequency test, we need do calibration manually. The calibration procedure includes calibration line and calibration sample cell two steps. As the sample cell calibration depends on the line calibration, a new sample

cell calibration should always be done after each line calibration.

4.4.4.1 Calibration line

Before starting a calibration, a blank floppy disk must be inserting into the analyzer drive.

Firstly, select **Calibration Line (HP4291).** Replace the sample cell by open (0S) calibration termination and start the open calibration by click **OK.**

After the open calibration is complete, connect the short $(0\ Ohm)$ calibration termination, and select **OK** to start short calibration.

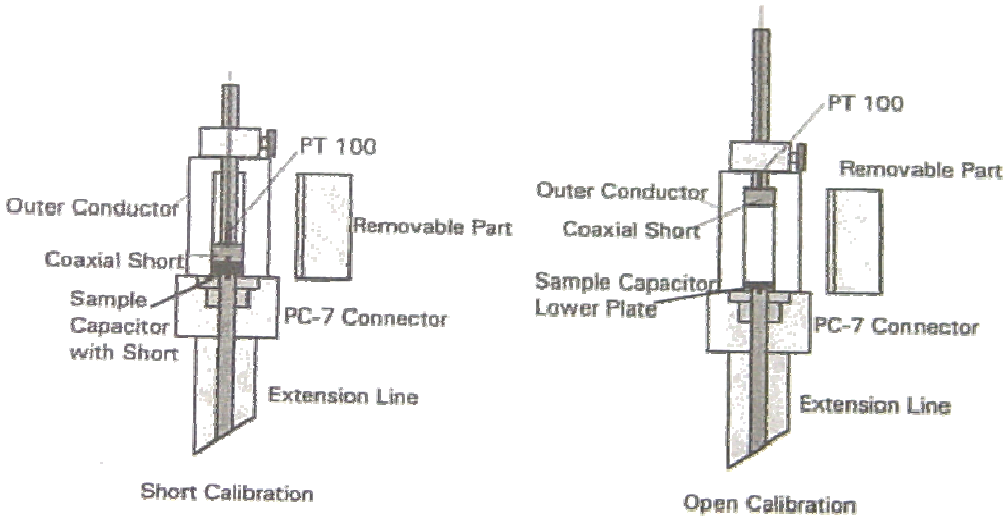
After the short calibration is done, connect the $50\ Ohm$ calibration termination $(0\ Ohm)$, and select **OK** to start short calibration.

Finally, connect the low loss capacitor calibration termination, and start the calibration.

After the end of the low loss capacitor calibration, save the calibration into the file WINDETA.STA on the analyzer floppy disk drive.

4.4.4.2 Calibration the sample cell

After selecting **Calibrate Sample Cell (HP 4291)**, remove any sample out of the cell and insert a sample capacitor with a short (two capacitor plates without a sample or spacers) as shown in the **Figure 4.16** (a). In order to get a good electrical contact, push down the coaxial short with a certain amount of pressure while fixing it with the screw. Then close the sample cell window. Select OK to start the short sample cell calibration.



(a) (b)

Figure 4.16. Calibration of sample cell

After the short calibration is complete, prepare the open sample capacitor by removing the upper plate of the sample capacitor out of the sample cell and moving the coaxial short to its upper position as shown in **Figure 4.16** (b). Then close the sample cell window and stat the open calibration.

After the open calibration is complete, WinDETA opens a file dialog to save the calibration.

4.4.5 The principle of the operation

4.4.5.1 Low frequency measurement

The basic principle of measurement of the BDC at low frequencies is shown in **Figure 4.17**. The ac voltage from the generator is applied to the sample and measured in amplitude and phase as U_1. The resistor R_0 protects the BDC electronics from damage if the sample impedance becomes too low. The sample current I_S feeds in the inverting input of an operational amplifier, which has the variable capacity C_X and the resistor R_X in its feed back loop. C_X can be switched between 200pF and 2200pF. R_X can be switched between 10Ω and 1TΩ in logarithmic intervals of a factor of 10.

The BDC selects a combination of C_X and R_X in such a way that the out put voltage U_2 of the amplifier is in a good measurement range of the analyzer. For ideal components, U_2 is related to the sample current I_S with

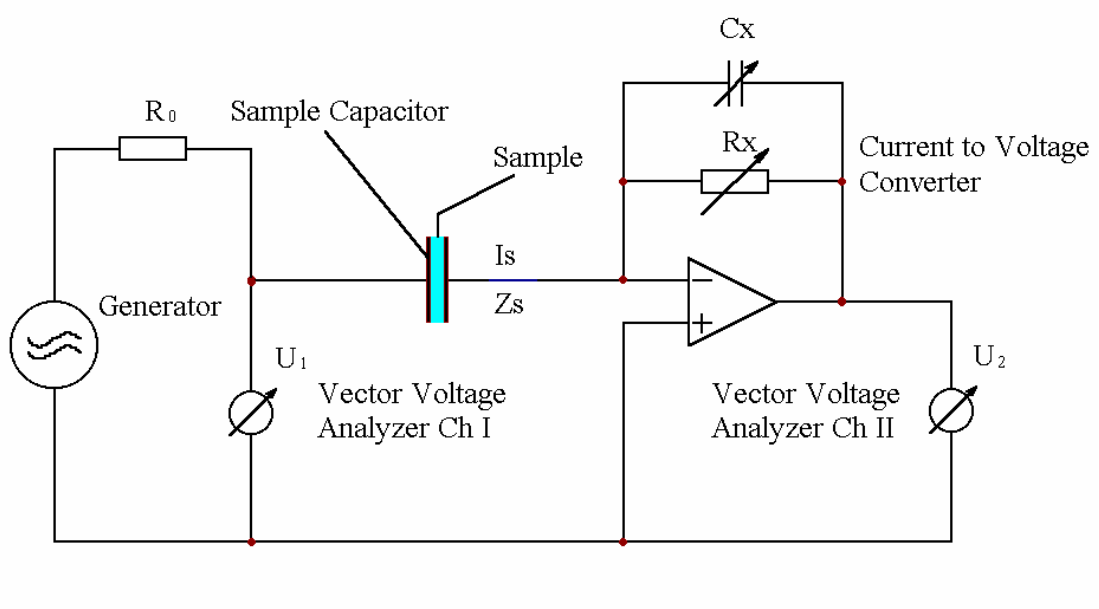


Figure 4.17. Principle of the impedance measurement at low frequencies.

$$I_S = -\frac{U_2}{Z_X} \tag{4.44}$$

where

$$Z_X = \frac{1}{R_X{}^{-1} + i\omega C_X} \tag{4.45}$$

For an ideal operational amplifier (infinite open loop gain), the input impedance is 0Ω and therefore U_1 corresponds to the voltage over the samplecapacitor. Thus, the sample impedance Z_S is give by:

$$Z_S = \frac{U_1}{I_S} = -\frac{U_1}{U_2} Z_X \tag{4.46}$$

The build in operational amplifier is limited to frequencies below approximately 100kHz.

4.4.5.2 High frequency measurement

The principle of the impedance measurement at high frequencies is shown in **Figure 4.18**.

The ac voltage of the analyzer generator drives the buffer amplifier, which decouples the sample current from the analyzer. The resistor R_0 limits the sample current if it is shorted. In contrast to low frequency measurement, the active current to voltage converter is replaced by a passive parallel combination of the variable resistor R_X and capacity C_X. Here C_X has a fixed value of 1000pF, and R_X can be switched between 10Ω and $100k\Omega$ in logarithmic intervals of a factor

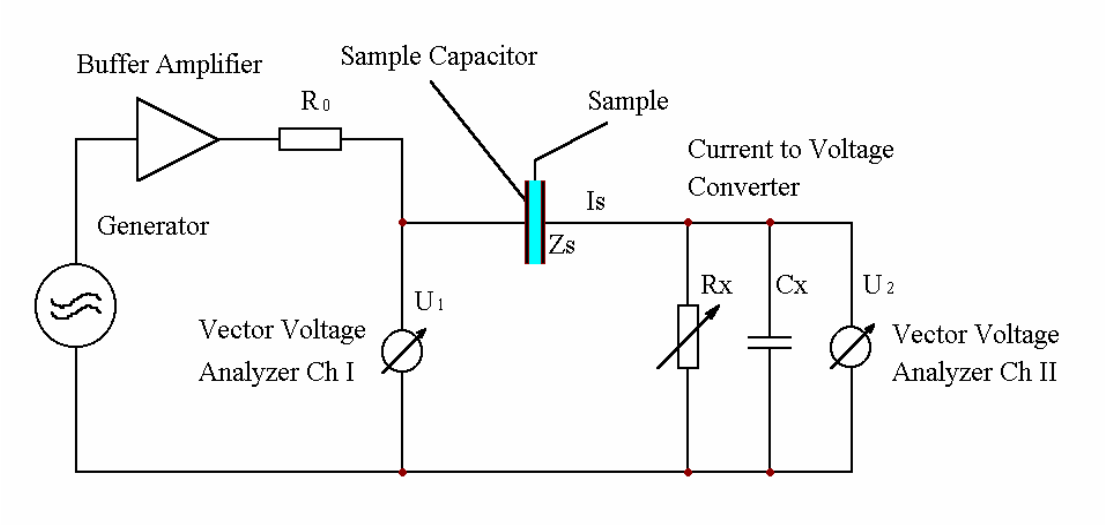


Figure 4.18. The principle of the impedance measurement at high frequencies.

of 10. For ideal componets and neglected line effects, Z_S is given as

$$Z_S = \frac{Z_X}{U_2}(U_1 - U_2) = Z_X \frac{1 - m_S}{m_S} \qquad (4.47)$$

where

$$m_S = \frac{U_2}{U_1}.$$

In practice, non ideal component, additional impedance due to measurement lines and effects of the internal BDC electronics limit the accuracy of measurement to a few percents. The errors due to these effects can be reduced if a reference measurement under the same conditions is made for Z_R. More specifically, the principle of reference measurement at low frequency is shown in **Figure 4.19**. The current to voltage converter is switched to the variable reference capacitor and the voltages U_{1R} and U_{2R} are measured after each sample measurement.

Z_X can be obtained from the reference measurement as:

$$Z_X = -m_R Z_R \qquad (4.48)$$

where

$$Z_R = -\frac{i}{\omega C_R},$$

$$m_R = \frac{U_{2R}}{U_{1R}}$$

By substituting Eq. (4.44) into Eq. (4.46), we have:

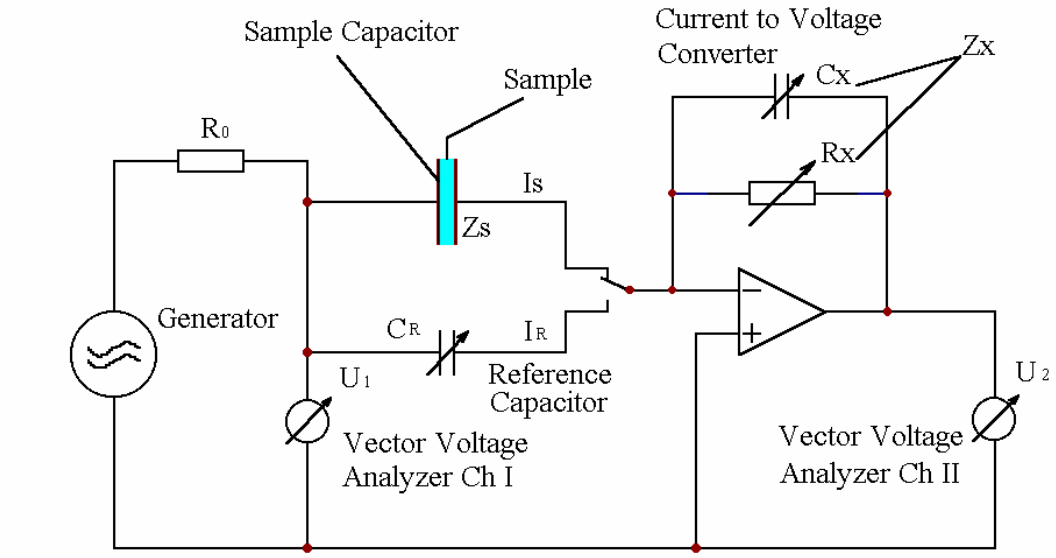


Figure 4.19. Principle of reference measurement at low frequencies.

$$Z_S = \frac{m_R}{m_S} Z_R \tag{4.49}$$

where

$$m_S = \frac{U_{2S}}{U_{1S}}.$$

Calculating the sample impedance from Eq. (4.46) and (4.47) gives more accurate results. However, some sources of the systematical errors as nonlinear distortions in the BDC and the analyzer remain active. To reduce these systematical errors the difference between the sample and the reference impedance must be minimized. Therefore, The BDC reference impedance can be adjusted in 64 steps between 25pF and 2nF which allows us selecting the matched reference capacity to the sample.

Similar to the low frequency measurement, the principle of the reference measurement at high frequencies is shown in **Figure 4.20**. In this case, Z_X is given by:

$$Z_X = \frac{m_R}{1 - m_R} Z_R. \tag{4.50}$$

The sample impedance can be derived as:

$$Z_S = \frac{1 - m_S}{m_S} \frac{m_R}{1 - m_R} Z_R. \tag{4.51}$$

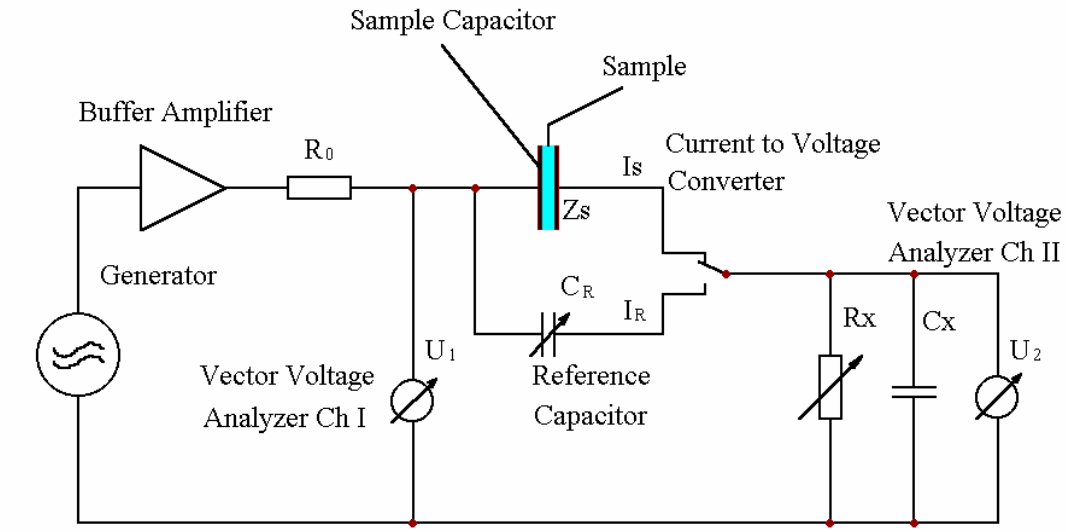


Figure 4.20. Principle of reference measurement at high frequencies.

4.4.6 Evaluation of data

The measurement set up for a sample cell consisting of a round plate capacitor is shown in **Figure 4.21**.

U^* and I^* denote the complex voltage and current respectively.

C_P^* denotes the complex parallel capacity of the filled sample capacitor without the influence of spacers.

C_S denotes the additional capacity caused by spacers in the sample capacitor volume.

The sample capacity is related to the measured voltage and current by:

$$C_P^* = -i\frac{I^*}{\omega U^*} - C_S . \qquad (4.52)$$

The sample impedance can be calculated from the complex parallel sample capacity C_P^* by:

$$Z_S = -\frac{i}{\omega C_P^*} . \qquad (4.53)$$

The complex dielectric constant ε^* is calculated by:

$$\varepsilon^* = \varepsilon' - \varepsilon'' = \frac{C_P^*}{C_0} . \qquad (4.54)$$

where C_0 is the empty cell capacity. For a sample cell consisting of a round parallel plates with diameter D and spacing d, C_0 is given by:

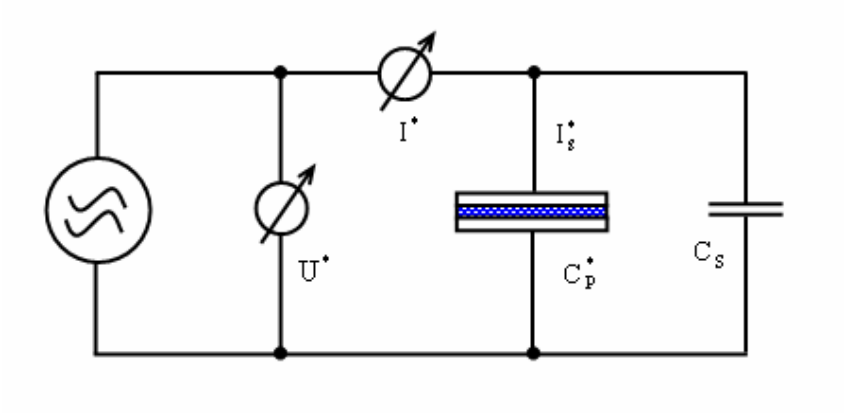


Figure 4.21. Measurement set up for a sample cell with a round plate capacitor.

$$C_0 = \varepsilon_0 \frac{\pi\left(\frac{D}{2}\right)^2 - Aspacer}{d}. \qquad (4.55)$$

where Aspacer designates the average area inside the sample capacitor occupied by the spacer material.

The loss factor $\tan(\delta)$ is calculated by:

$$\tan(\delta) = \frac{\varepsilon''}{\varepsilon'} = -\frac{Z_S'}{Z_S''} \qquad (4.56)$$

The loss angle δ is obtained as $\delta = \frac{180°}{\pi} \arctan\left(\frac{\varepsilon''}{\varepsilon'}\right)$.

In contrast to the loss angle δ, the phase angle $\varphi = \frac{180°}{\pi} \arctan\left(\frac{Z_S''}{Z_S'}\right)$ specifies the applied voltage U^* and the sample cell current I_S^*, and is shifted by $90°$ with respect to δ.

CHAPTER 5 EXPERIMENT RESULTS AND DISCUSSION

Both dielectric spectroscopy (DS) and dynamic light scattering (DLS) are powerful techniques that can be used to study the confinement effect on the dynamic behavior of LCs. The two techniques provide complementary information on the relaxation processes in LCs. DS measures the dynamical properties integrated over the whole sample, while the DLS provides information at different length scale by scattering measured at different angles. More specifically, DS probes the relaxation due to the reorientations of polar molecules in the sample while DLS measures the fluctuations of director reorientations in nematic LC.

DLS experiments were performed using a $\lambda = 0.6328\mu m$ He-Ne laser and ALV-5000/FAST Digital multiple Tau correlator operating over delay times from 12.5 ns up to 1000 s. The ALV/ LSE unit allowed monitoring the laser beam intensity and the stability of its space position as well as monitoring the intensity of scattered light integrated over all frequencies. The depolarized component of the scattered light was investigated. This allowed us to detect the contribution from the order parameter in isotropic phase of bulk LC, and, for the confined LC, the scattering from the host matrix was also blocked out.

In the DLS experiment, the intensity-intensity autocorrelation function was measured:

$$g_2(t) = \langle I(t) \cdot I(0) \rangle / \langle I(0) \rangle^2 . \quad (5.1)$$

This function is related to dynamic structure factor $f(q,t)$ of the sample by:

$$g_2(t) = 1 + kf(q,t)^2, \quad (5.2)$$

where *k* is a contrast factor that determines the signal to noise ratio, $q = 4\pi n \sin(\theta/2)/\lambda$, n is the refractive index, and θ is the scattering angle. The intensity-intensity autocorrelation functions were observed to be q-independent for LCs in mesoporous materials. Therefore, all the dynamic scattering data were obtained at $\theta = 35°$. The lowest accessible temperature was 265 K. The temperature stabilization was better than $0.01°C$.

5.1 Static Light Scattering Results

The static light scattering method is one of the most effective procedures for the investigation of the N-I phase transition in LCs. In static light scattering experiments, the time-averaged intensity of the scattered light is measured.

The order parameter measures how well the molecules are aligned with the director. It is defined as:

$$S = \frac{1}{2}\langle 3\cos^2\theta - 1 \rangle \quad (5.3)$$

where <> denotes a thermal averaging and θ is the angle between each molecule and the director.

In the isotropic phase of LCs, the equilibrium value of order parameter is zero without any perturbation from an external field, but the fluctuations of the order parameter, which are the main sources of the light scattering, are anomalously large. As a result, the intensity of the scattered light is frequently larger than that of usual organic liquids by several orders of magnitude. The scattering due to density fluctuations can be neglected in this case.

In the nematic phase of LCs, the scattering of light generates from the orientational fluctuations of the director, from order parameter fluctuations, and from density fluctuations. However, the director fluctuation is the main contribution to the intensity of the scattered light, and the influences of the other two factors can be neglected. Usually, the intensity of scattered light in a nematic phase exceeds that in an isotropic phase by several orders of magnitude. Therefore, a sharp increase in the intensity of the scattered light should be observed at the temperature of N-I phase transition. Thus, static light scattering measurements can be used to determine the N-I phase transition temperature precisely.

The N-I phase transition is a weak first-order phase transition; some characteristics of second-order transitions are also observed. The phase transition has a small jump in the specific volume, an insignificant heat of transition, and an increase in the order parameter fluctuation in the vicinity of T_c. As a result, an

increase in the intensity of scattered light, an anomalous behavior of the heat capacity, an increase in the magnetic birefringence, and a critical retardation of fluctuations are observed [65].

In static light scattering measurements, the intensity of depolarized light scattered at scattering angle $35°$ was recorded as a function of temperature. The samples were heated to the isotropic phase at temperature about $5°C$ above the phase transition temperature. After temperature equilibration, the measurements were started. The temperature was decreased at a constant rate of 0.0833 K/min until the temperature was about $5°C$ below the phase transition temperature. For each data point, the averaged intensity of scattered light was collected for duration of 10 s. In this process, the corresponding change of temperature is 0.0139 K, which was negligibly small, and the measurements could be considered to be performed under quasi-equilibrium conditions.

Subsequently, a heating run was performed, and the temperature range and the heating rate were exactly same (but of opposite sign) as those of the previous run. As shown in **Figure 5.1**, and **Figure 5.2**, a hysteresis was observed for each sample, and the phase transition temperature was shifted to higher temperature in the heating measurements. Finally, the cooling measurement was undertaken again at even slower rate of 0.0187 K/min at which the temperature change for each data point was less than 0.0031 K. In this way, the phase transition region was narrower, and the phase transition temperature could be determined more precisely. The corresponding results were shown in **Figure 5.3** and **Figure 5.4** for

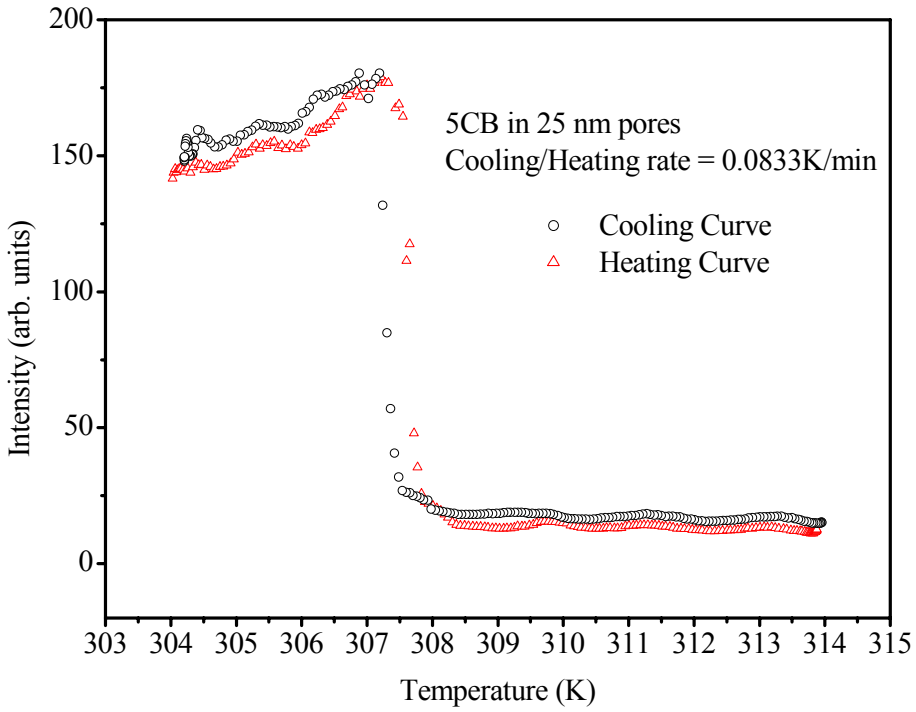


Figure 5.1. Temperature dependence of intensity of scattered light for 5CB confined in SBA-15 with 25 nm pores (fast run results).

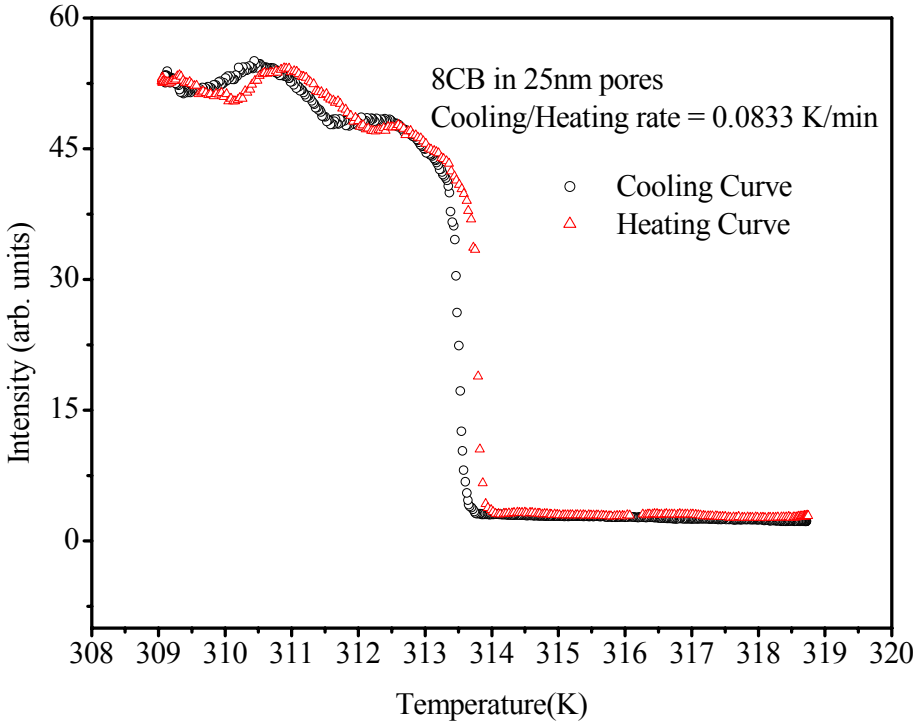


Figure 5.2. Temperature dependence of intensity of scattered light for 8CB confined in SBA-15 with 25 nm pores (fast run results).

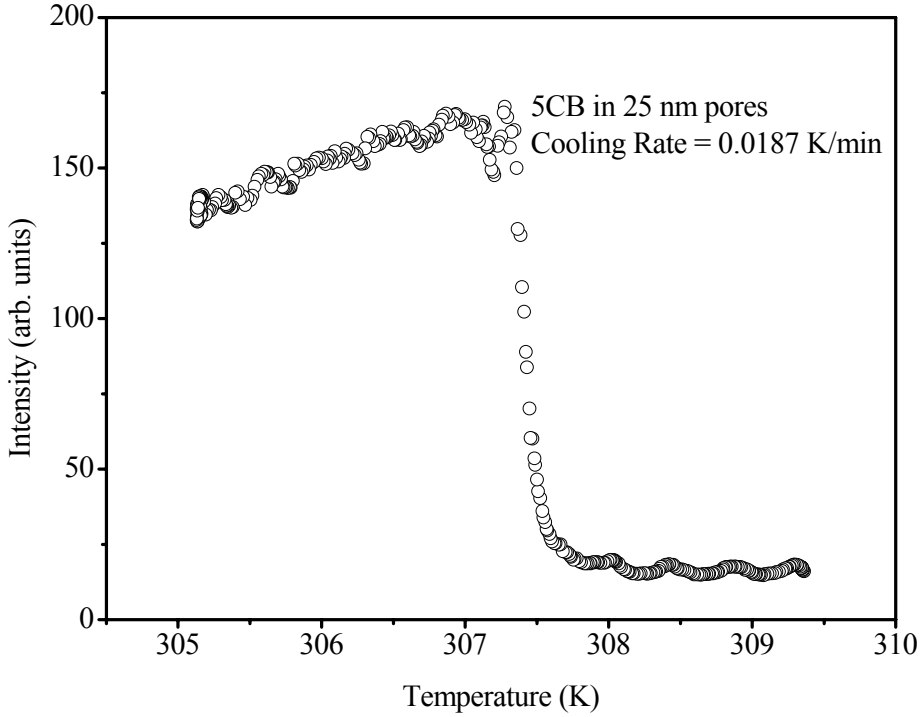


Figure 5.3. Temperature dependence of intensity of scattered light for 5CB confined in SBA-15 with 25 nm pores (slow run results).

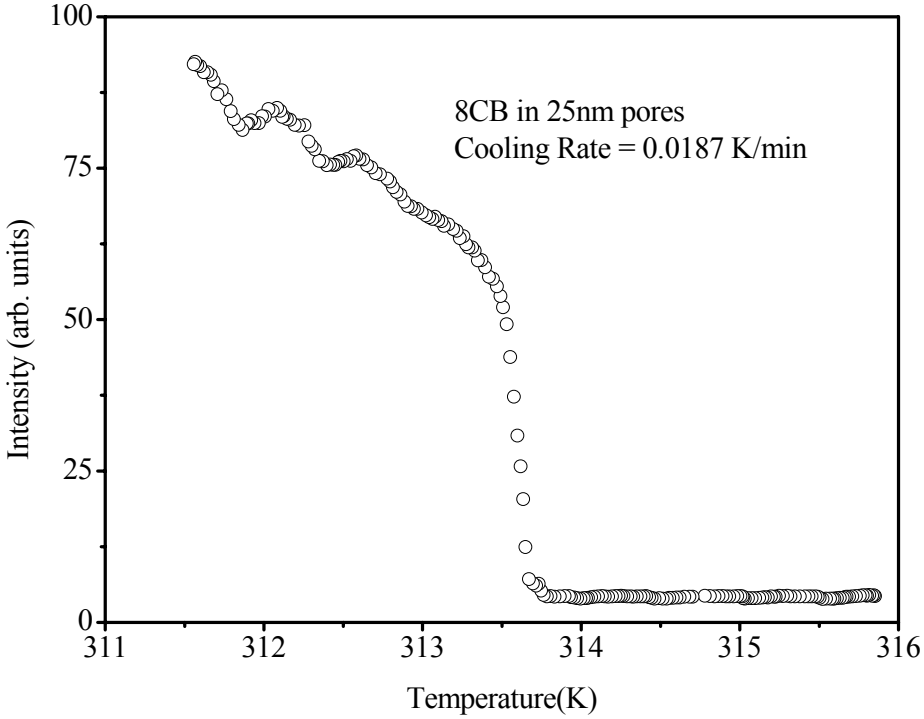


Figure 5.4. Temperature dependence of intensity of scattered light for 8CB confined in SBA-15 with 25 nm pores (slow run results).

5CB and 8CB confined in 25 nm pores.

The temperature dependences of the scattering intensity I_{SC} for bulk 5CB and 8CB are shown in **Figure 5.5** and **Figure 5.6**, respectively. A strong increase in the scattering intensity I_{SC} was observed at the phase transition temperature T_{IN} as expected. The isotropic-nematic phase transition temperature of bulk 5CB and 8CB are determined as 308.33 K and 314.15 K, respectively.

The temperature dependence of the inverse scattering intensity for bulk 5CB and 8CB in isotropic phase and their linear fits are shown in the inlets of **Figure 5.5** and **Figure 5.6**. It is well-known that in bulk isotropic phase, I_{SC} is mainly due to order parameter fluctuations, and the temperature independence of I_{SC} is described by Landau-de Gennes theory, namely:

$$I_{sc} = \frac{1}{\left(T - T^*\right)^{\gamma}} \tag{5.4}$$

where γ is the critical exponent of susceptibility which is equal to 1 in Landau-de Gennes theory, and T^* is slightly below the N-I phase transition temperature T_{NI} and can be determined by investigating the near–critical behavior of the LC in the isotropic phase. The LCs behave in the isotropic phase as if there would be a second order phase transition at T^*. T^* is the maximum super cooling temperature of the isotropic phase. When temperature approaches T^*, the size of fluctuation or the correlation length ζ, becomes infinity. In other words, T^* represents the absolute limit of stability of the isotropic phase. Typically,

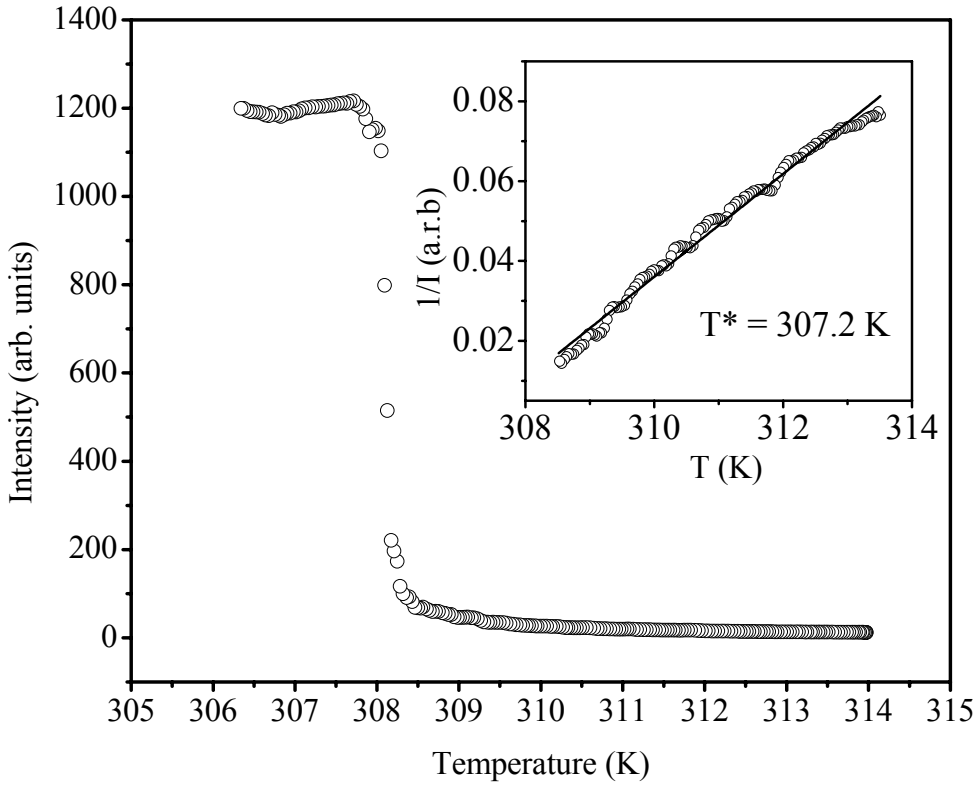


Figure 5.5. Temperature dependence of the scattering intensity of bulk 5CB. The inlet shows the temperature dependence of the inverse intensity and the fitting in isotropic phase. (Open circles, experiment; solid lines, fitting.)

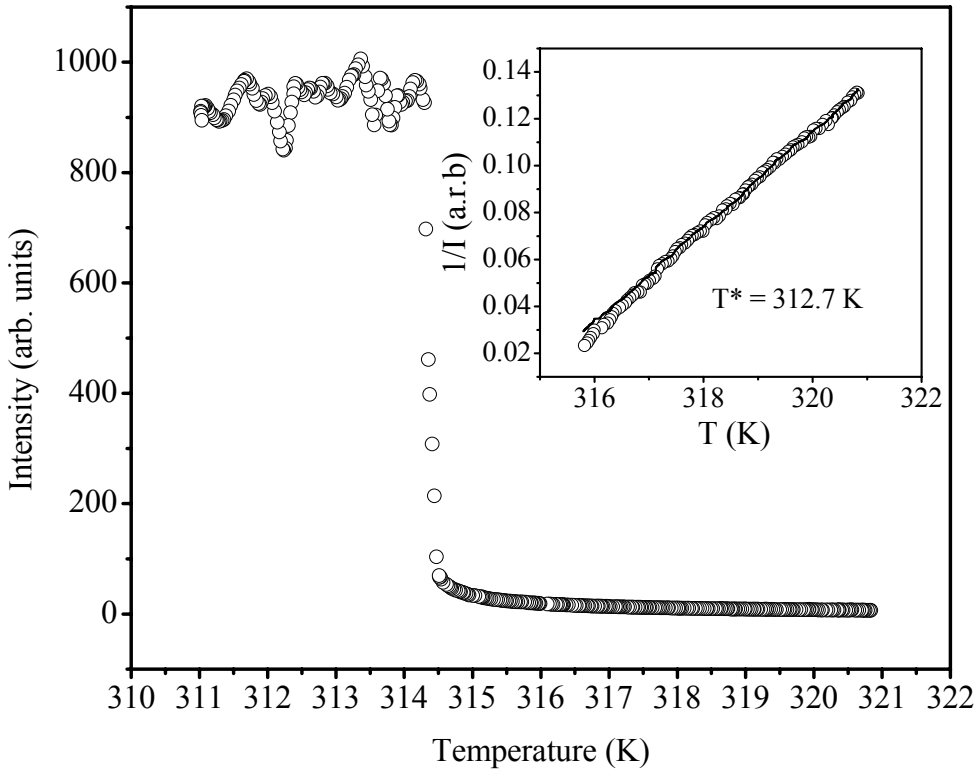


Figure 5.6. Temperature dependence of the scattering intensity of bulk 8CB. The inlet shows the temperature dependence of the inverse intensity and the fitting in isotropic phase. (Open circles, experiment; solid lines, fitting.)

$T_{NI} - T^* \cong 1.5K$.

From the inlets of **Figure 5.5** and **Figure 5.6**, we could see clearly that in the bulk isotropic phase, I_{SC} is temperature dependent and exhibits the mean field theory critical exponent $(\gamma = 1)$ expected near a second-order transition at a temperature T^* preempted by a first order phase transition at T_{NI}. The value of T^* for bulk 5CB and 8CB can be determined by linear fitting results which are equal to 307.2 K and 312.7 K, respectively.

A strong increase in the intensity of the scattered light I_{SC} was also observed in the vicinity of bulk phase transition temperature for each confined sample. The temperature dependences of the I_{SC} for 5CB and 8CB confined in 25 nm pores were presented in **Figure 5.7** and **Figure 5.8**, respectively.

The inverse of *Isc* vs. temperature data of confined 5CB and 8CB are plotted in insets of **Figure 5.7** and **Figure 5.8**. It should be note that the temperature dependence of I_{SC} in the isotropic phase of the confined LC is different from that in the bulk for all the pore sizes which have been explored. In pores, I_{SC} is almost independent of temperature in the temperature range corresponding to the isotropic phase, and only small fluctuations were observed.

Figure 5.9 and **Figure 5.10** present the temperature dependence of depolarized component of intensity of scattered light *Isc(T)* measured at a scattering angle $35°$ for bulk and confined 5CB and 8CB, respectively. All the experiments were done at the same cooling rate. It is clearly seen that the increase

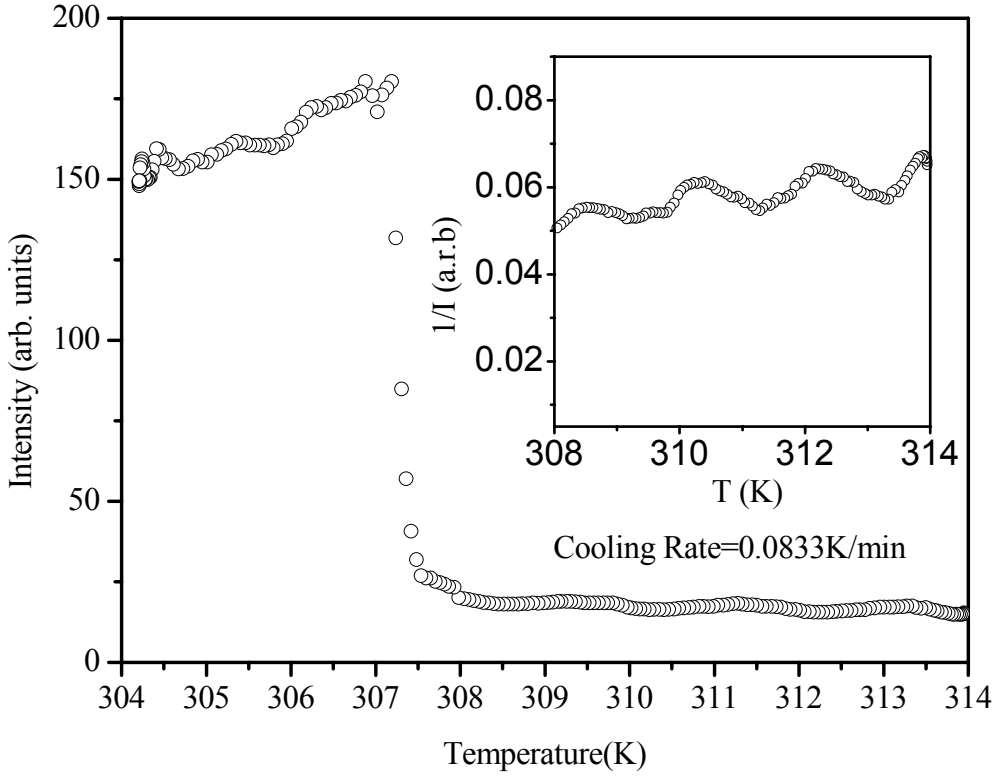


Figure 5.7. Temperature dependence of the scattering intensity of 5CB confined in 25 nm pores. The inlet shows the temperature dependence of the inverse intensity.

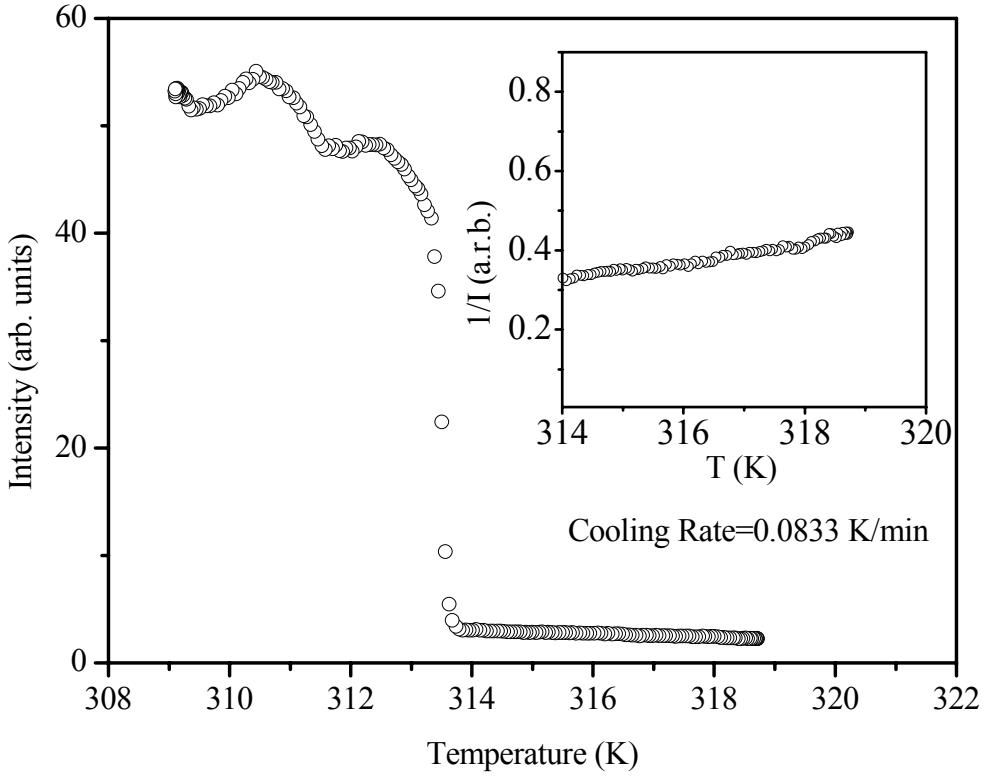


Figure 5.8. Temperature dependence of the scattering intensity of 8CB confined in 25 nm pores. The inlet shows the temperature dependence of the inverse intensity.

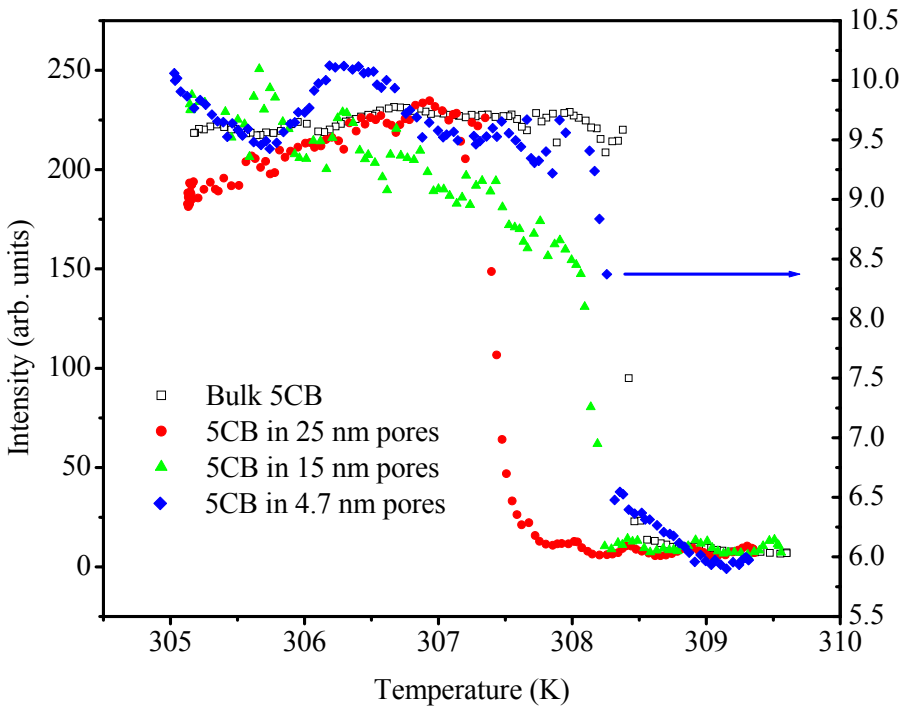


Figure 5.9. Temperature dependence of scattering intensity for bulk and confined 5CB.

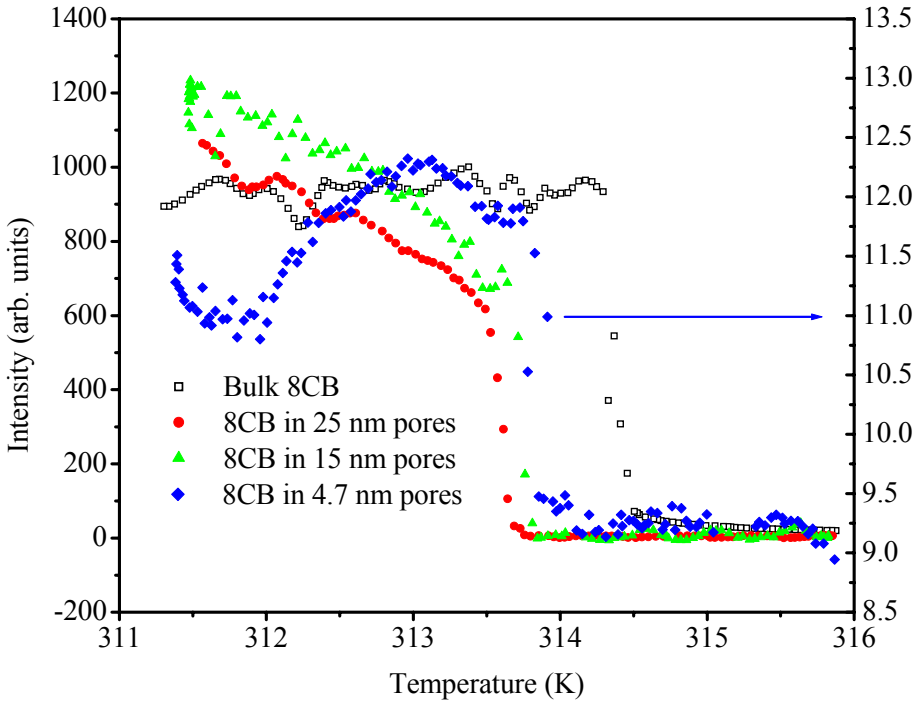


Figure 5.10. Temperature dependence of scattering intensity for bulk and confined 8CB.

of scattering intensity of bulk 8CB is sharp; whereas, for the confined sample, the phase transition region is broad and the phase transition temperature is shifted away from bulk transition temperature.

Determination of phase transition temperature of the confined LC became more difficult because the temperature range of the phase transition is broader, and it is hard to tell precisely which temperature should be regard as phase transition point. Static and dynamic light scattering methods are commonly used together to determine the phase transition temperature of confined LCs.

In the dynamic light scattering experiment, only one relaxation process due to fluctuations of the order parameters should be present in the isotropic phase. In the nematic phase, the decay of $g_2(t)$ is due to the director fluctuations. The relaxation times of these two processes are quite different. Therefore, it is easy to differentiate the nature of the relaxational process and to identify the corresponding phase transition point. The N-I phase transition temperature was considered to be a temperature below which no order parameter fluctuation was observed. This temperature was found to coincide with the temperature at which the intensity of the scattered light does not increase any more with decreasing temperature.

The N-I phase transition temperature of bulk and confined 5CB and 8CB are obtained and shown in **Table 5.1**.

As can be seen from the table, T_{IN} of confined 5CB was shifted to lower temperature in comparison with that of bulk 5CB, whereas T_{IN} increases with

Table 5.1. N-I phase transition temperature of bulk and confined 5CB and 8CB.

	T_{NI} (bulk) (K)	T_{NI} (25 nm pores) (K)	T_{NI} (15 nm pores) (K)	T_{NI} (7.3 nm pores) (K)	T_{NI} (4.7 nm pores) (K)
5CB	308.3	307.3	308.0	308.1	308.1
8CB	314.2	313.5	313.6	313.7	313.7

decreasing pore size.

If pore size is extremely small (less than 7.3 nm in diameter), the phase transition temperature is almost independent of pore size. For 8CB, similar phenomena were observed. This can be explained as follows. There are at least two effects, namely a finite size effect and a surface effect, which affect the phase transition behavior simultaneously. The finite size effect will shift the phase transition temperature to a lower temperature since the temperature shift is proportional to the inverse of pore radius, namely:

$$\Delta T = \left(T_{bulk} - T_{confined}\right) \sim \frac{1}{r}, \tag{5.3}$$

where T_{bulk} and $T_{confined}$ are the phase transition temperature of the bulk LCs and the confined LCs respectively, and r represents the pore radius. As the pore size decreases, the difference of between the phase transition temperature of the bulk and that of the confined LCs increases. As a result, $T_{confined}$ shifts to lower temperature. On the other hand, we can consider the surface interaction effect to be like that of an external applied field, which usually increases $T_{confined}$. The phase transition temperature either increases or decreases with decreasing pore size depending on which factor plays a dominant role. For both 5CB and 8CB in confined geometry, the phase transition temperature is shifted to lower temperature in comparison with the bulk because the role of finite size effect exceeds the role of surface effect. However, as the pore size decreases, the surface effect becomes more and more important. As a result, the phase transition

temperature is shifted to higher temperature with decreasing pore size. When the pore size reaches certain small value, two effects counteract each other, therefore the phase transition temperature also keeps at certain value.

5.2 Dynamic Light Scattering (Photon Correlation Spectroscopy) Results

DLS measures dynamic fluctuations of intensity of scattered light. The molecules in a liquid medium undergo fluctuations of the local density, alignment, or order, resulting in local inhomogeneities of the refractive index. This in turn results in fluctuations of intensity of the scattered light.

For bulk LCs in the isotropic phase, the intensity-intensity autocorrelation function of the depolarized component of scattered light is determined by order parameter fluctuations and the corresponding decay is described by a single exponential function. In the nematic phase, the relaxation process due to the director fluctuations is described by the macroscopic equations of nematodynamics, and the relaxation time is determined by viscoelastic properties of nematic LCs, the geometry of an experiment, and light polarization.

5.2.1 Properties of bulk 5CB

DLS properties of bulk LCs are well known. The present DLS experiments were performed over a wide temperature range from 300.15K to 308.8K. Both the nematic phase and supercooled state of bulk 5CB were studied.

Figure 5.11 shows typical intensity/intensity autocorrelation functions and their fittings of bulk nematic 5CB at different temperatures. The contrasts of the autocorrelation functions are about 99.5%, which is very close to the theoretical limit 1 because single mode optical fiber was used for detection of scattered light. All the autocorrelation functions can be fitted very well with a single stretched exponential function:

$$g_1(q,t) = \alpha \exp\left[-\left(\frac{t}{\tau}\right)^{\beta}\right] \qquad (5.1)$$

where α is the amplitude of the decay function, τ is the relaxation time of director fluctuations, and β is a fitting parameter which determines the spread of the decay function. Small deviation of β from 1 is due to the fact that a multi-domain sample was used.

The fitting results at different temperatures are shown in **Table 5.2**. It is clear that the relaxation time increases and director fluctuation process become slower as the temperature decreases. This can also be observed in **Figure 5.11**. The temperature dependence of relaxation times of director fluctuations of 5CB in both the nematic phase and the supercooled state are presented in **Figure 5.12**.

In the bulk nematic phase, the main contribution to the intensity of scattered light is the director fluctuations. There are two modes associated with these fluctuations. They are a combination of splay and bend distortions and a combination of twist and bend distortions, respectively. Each of these modes is

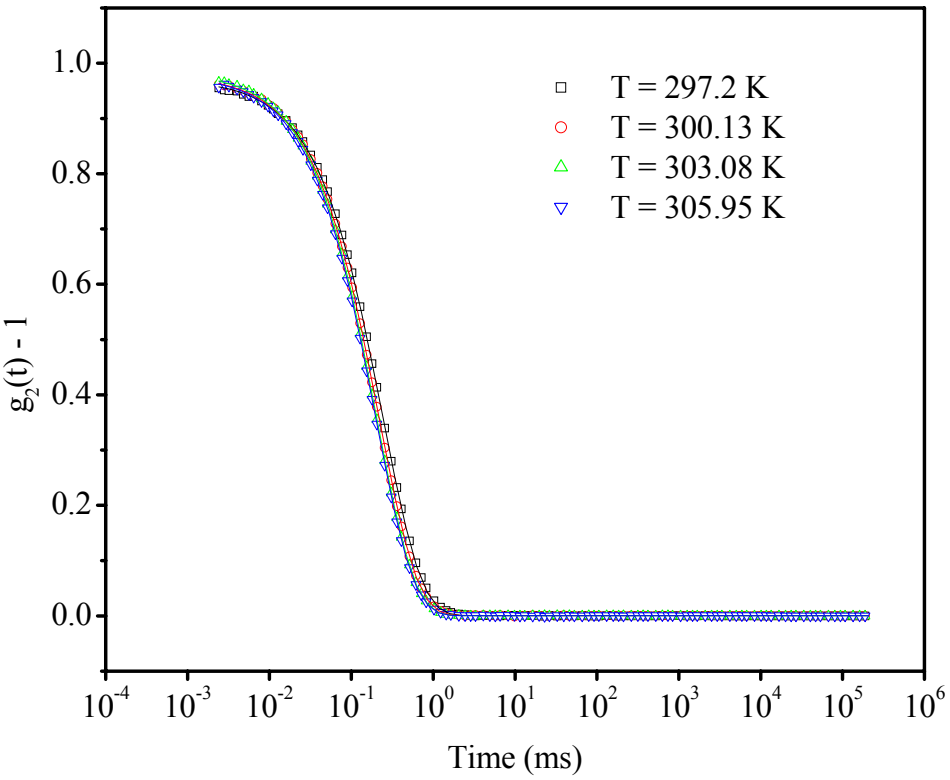


Figure 5.11. Intensity/intensity autocorrelation functions for bulk 5CB in nematic phase at different temperatures. Open symbols: experiment, solid lines:fitting.

Table 5.2. Fitting results of autocorrelation function for bulk 5CB at different temperature using single stretched exponential equation.

	α	Error	$\tau 1$(ms)	Error	β	Error
T = 297.20 K	0.98515	0.00021	0.51794	0.00075	0.92224	0.00139
T = 300.13 K	0.9887	0.00012	0.45802	0.00036	0.92777	0.00078
T = 303.03 K	0.99146	0.00012	0.42351	0.00032	0.93314	0.00076
T = 305.95 K	0.98884	0.00014	0.41461	0.00038	0.93522	0.00092

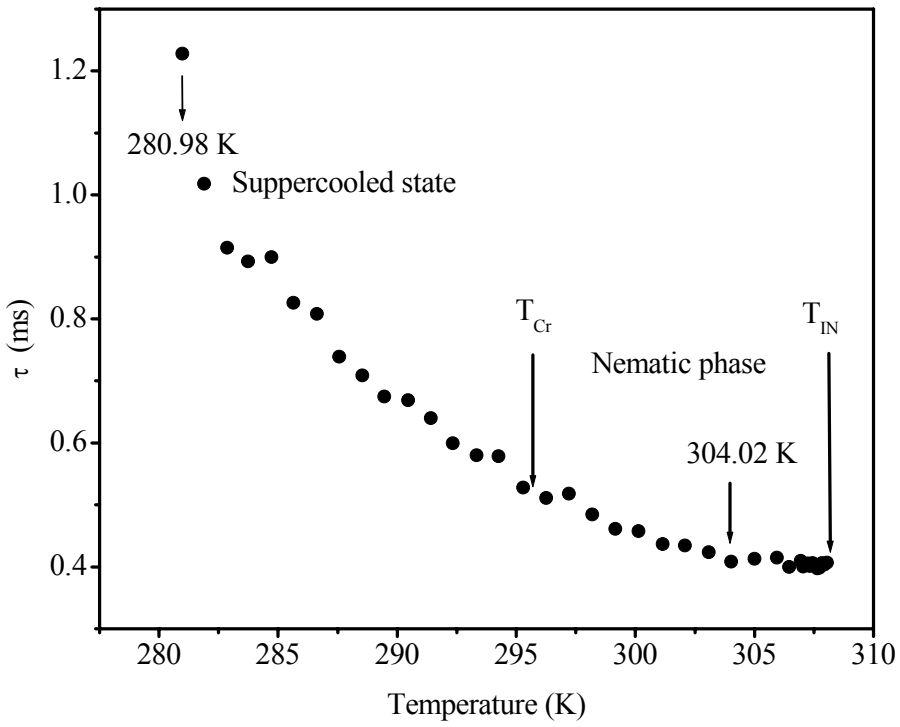


Figure 5.12. Temperature dependence of relaxation times due to director fluctuations of bulk 5CB in nematic phase and supercooled state.

described by a single exponential decay function. For simplicity, we assume the six Leslie coefficients are of the same order of magnitude, we take the average value of viscosity, η, and we assume the three elastic constants (bend, splay and twist) to be the same, *K*. The relaxation time of director fluctuations is [66]

$$\tau = \frac{\eta}{Kq^2} \qquad (5.2)$$

and has the order of magnitude 10^{-5}.

When the temperature approaches the N-I phase transition point, the elastic constant, K, decreases and approaches 0. The effective viscosity, η, also decreases, but the change of η is much less evident than that of K. As a result, the relaxation time related to the director fluctuation increases with the increasing temperature. When temperature falls within the range of 304.02 K to 308.15 K, the ratio of η to K remains constant. Therefore, the relaxation time τ is almost temperature-independent in this temperature range. When temperature is lower than 304.02 K, bulk 5CB which is approaching the supercooled state, becomes more viscous. The effective viscosity, η, increases with decreasing temperature, whereas the elastic constant, K, does not change as much as viscosity. As a result, the relaxation time, τ, increases slowly and steadily with decreasing temperature.

5.2.1.1 Properties of bulk 8CB

It is well known that 8CB has two distinct LC phases, namely nematic and smectic-A phase. The N-I phase transition temperature and the SmA-N phase transition temperatures are 313.95 K and 306.65 K, respectively. Here we only

discuss the autocorrelation functions of 8CB in the nematic phase. **Figure 5.13** shows the autocorrelation function and fitting curves of bulk nematic 8CB at different temperatures. The autocorrelation functions can be well fitted with single stretched exponential functions, and the parameters obtained from the fitting results are presented in **Table 5.3**.

The temperature dependence of relaxation time of director fluctuations in bulk nematic 8CB is shown in **Figure 5.14**. As can be seen, the relaxation process slows down in the vicinity of the N-I phase transition point because of the rapid decrease of the elastic constant, K. In the temperature range between 313.5K and 308.3K, the relaxation time is almost temperature-independent because the ratio of η to K remains constant. When temperature approaches the N-A phase transition temperature, K increases, but η increases much more. As a result of the rapid increase of the viscosity, the relaxation time increases, and the process slows down.

5.2.1.2 Properties of confined LCs

Intensive research work has been done to investigate the confinement and surface effects on the behaviors of confined LCs. A variety of new properties and phenomena such as a modification of phase transitions, orientational order, elastic properties, director field and so on have been established [83]. Although the physical properties of LCs in porous media with different sizes and various shapes of pores have been explored, little work has been done to investigate the confinement effects on the static and dynamic behavior of confined LCs. It is well

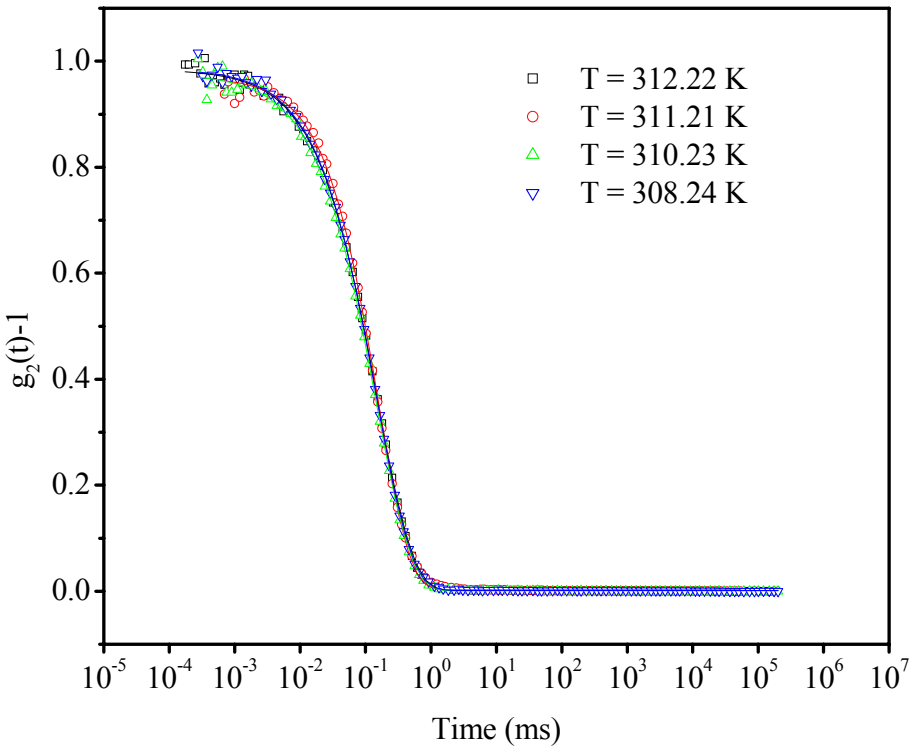


Figure 5.13. Intensity/intensity autocorrelation functions for bulk 8CB in nematic phase at different temperatures. Open symbols: experiment, solid lines: fitting.

Table 5.3. Fitting results of autocorrelation function for bulk 8CB at different temperature using single stretched exponential equation.

	α	Error	τ1(ms)	Error	β	Error
T = 308.24 K	0.9915	0.00062	0.3607	0.0023	0.79952	0.00408
T = 310.23 K	0.98393	0.00099	0.33721	0.00273	0.90287	0.00693
T = 311.21 K	0.98756	0.00079	0.34115	0.00257	0.80666	0.00505
T = 312.22 K	0.99206	0.00057	0.34936	0.00191	0.8121	0.0037

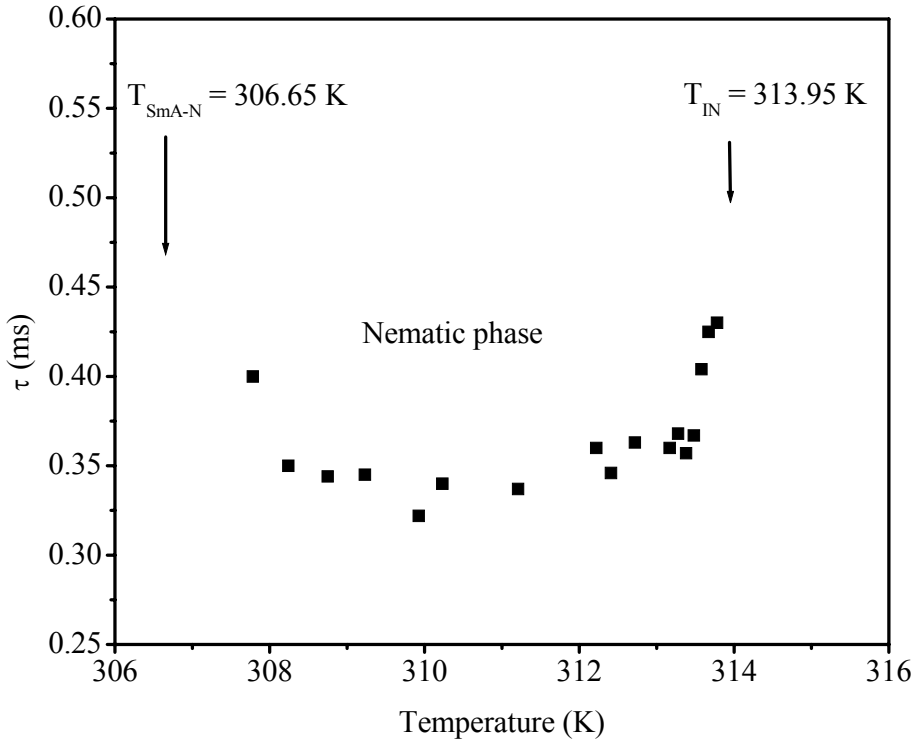


Figure 5.14. Temperature dependence of relaxation times due to director fluctuations of bulk 8CB in nematic phase and supercooled state.

known that confinement will affect the properties of LCs in two different aspects, namely finite size effect and surface effect. The confinement will break the symmetry of the bulk phase and change the effective viscosity, which in turn will modify the dynamics. Two effects mentioned above will work together to affect the whole system, and it is hard to separate the two influences. This adds additional complication to the problem. Also, the pore sizes available from commercial porous media are limited. The variety of porous media introduces different pore surfaces to the system. These make the comprehensive understanding of the characteristics of confined LCs a difficult task, and the results might seem puzzling and contradictory.

In the current work, we use SBA-15 mesoporous material as a tool to investigate the confinement and surface effects on the confined LCs. The easily-tuned pore size, narrow pore size distribution, and identical pore wall-LC interface allow us study this topic systematically.

In our experiments, SBA-15 mesoporous matrices with pore diameter 4.7 nm, 7.3 nm, 15 nm and 25 nm impregnated with 5CB and 8CB were used as porous media to investigate the dynamic behavior of confined LCs.

The intensity-intensity autocorrelation functions of 5CB in nematic phase, confined in 15 nm and 4.7 nm pores are shown in **Figure 5.15**. Similarly, the intensity-intensity autocorrelation functions of 8CB in nematic phase, confined in 25 nm and 4.7 nm pores are shown in **Figure 5.16**. For confined LCs in the nematic phase, two well-defined relaxation processes are observed. The first

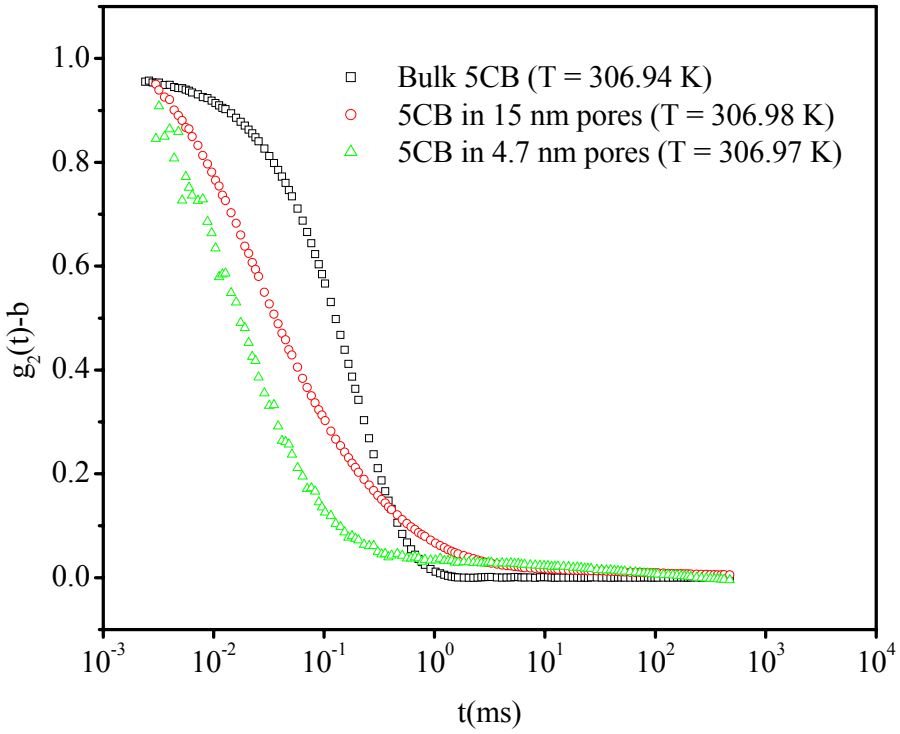


Figure 5.15. Intensity-intensity autocorrelation functions of 5CB in bulk nematic phase and nematic phase confined in 15 nm, 4.7 nm pores.

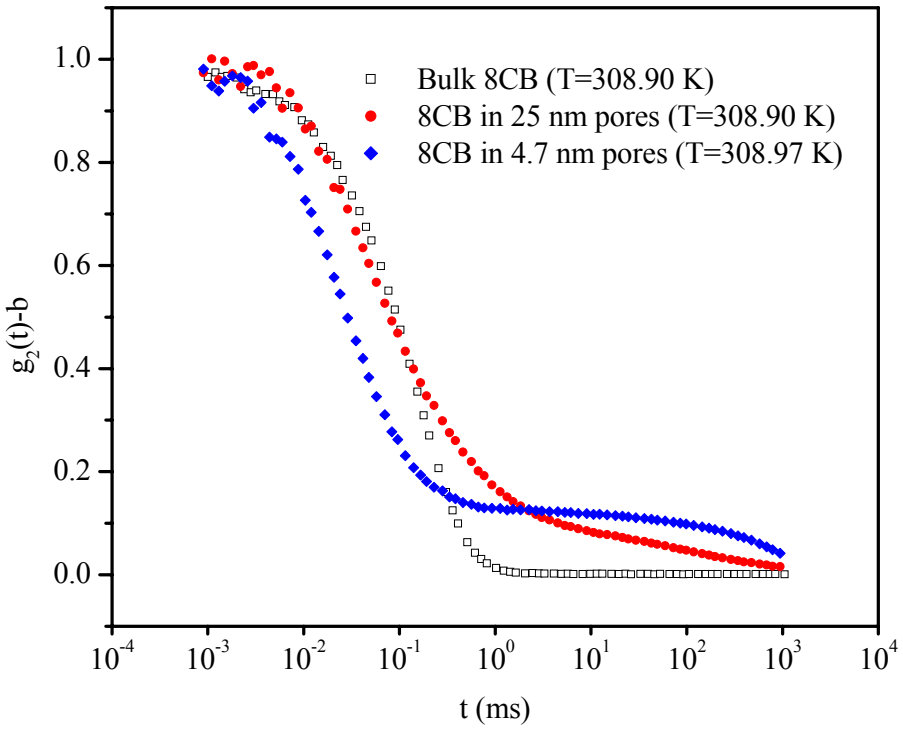


Figure 5.16. Intensity-intensity autocorrelation functions of 8CB in bulk nematic phase and nematic phase confined in 25 nm, 4.7 nm pores.

relaxation process is qualitatively associated with bulk-like nematic director fluctuations. The second relaxation, absent in bulk LCs and with relaxation time slower than the first one, is most likely due to the fluctuations in the layers nearest to the pore surface.

A comparison of normalized autocorrelation functions of bulk and confined 5CB and 8CB are shown in **Figure 5.17** and **Figure 5.18**, respectively. We found that for both 5CB and 8CB, the autocorrelation functions of bulk LCs can be fitted with a single stretched exponential function, whereas the relaxation processes of confined LCs have a broader range of decay times, and a slow relaxation process not shown in the bulk is observed. The second process is most likely related to the director fluctuations in LC layer close to the pore wall surface. The autocorrelation functions can be fitted with a double stretched exponential function:

$$g_1(q,t) = \alpha \exp\left[-\left(t/\tau_1\right)\right]^{B_1} + (1-\alpha)\exp\left[-\left(t/\tau_2\right)\right]^{B_2} \qquad (5.3)$$

where α is the amplitude of the first process due to the relaxation process of bulk-like director fluctuations; 1-α is the amplitude of the slow process; τ_1 and τ_2 are the relaxation times corresponding to the first and second decay process, respectively; and B_1 and B_2 represent the degree of the stretching of the decay functions. The observed two processes are strongly coupled to each other; therefore, the determination of the relaxation time of each process cannot be done independently.

The temperature dependence of the relaxation time for bulk-like director

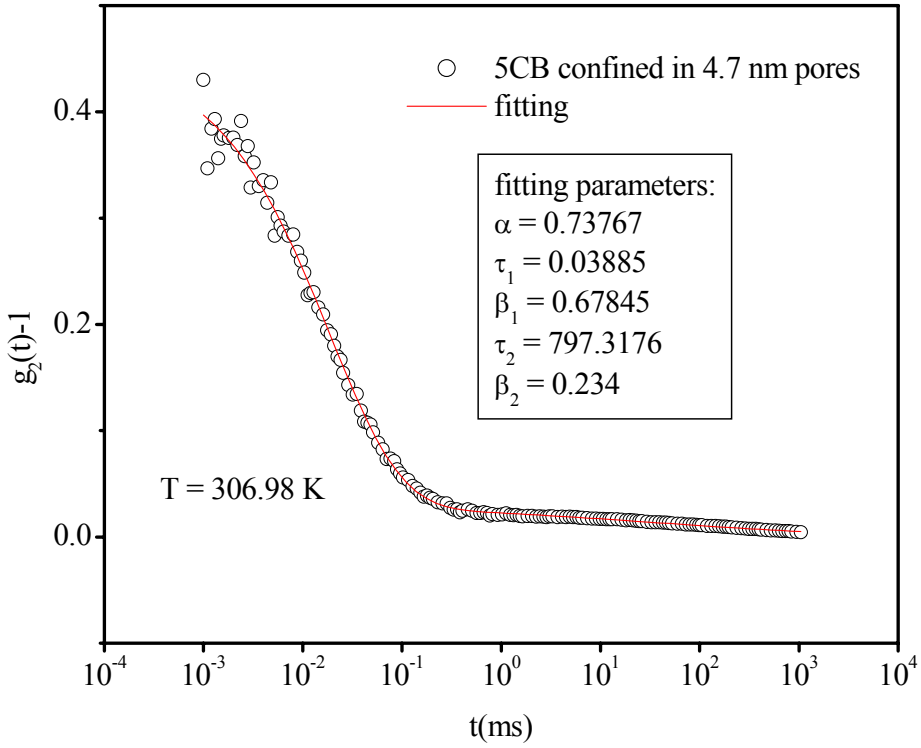


Figure 5.17. Intensity-intensity autocorrelation function of 5CB confined in 4.7 nm pores. Open symbols, experiments; solid line, double stretched exponential fit.

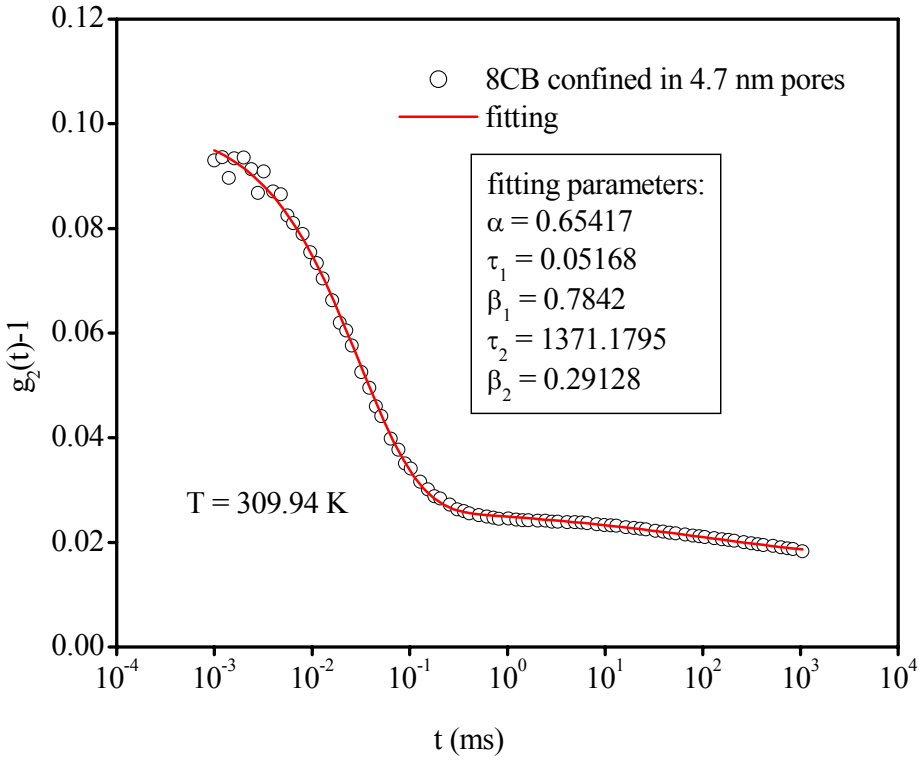


Figure 5.18. Intensity-intensity autocorrelation function of 8CB confined in 4.7 nm pores. Open symbols, experiments; solid line, double stretched exponential fit.

fluctuations of bulk and confined 5CB and 8CB are shown in **Figure 5.19** and **Figure 5.20**, respectively. As shown in these figures, the variation of τ_1 is qualitatively the same for both confined 5CB and 8CB in comparison with bulk LCs. In the case of confined 5CB, τ_1 decreases steadily with increasing temperature when 5CB is in its supercooled state. In the nematic phase, there is no temperature dependence of τ_1 since the ratio of η / K remains constant in this temperature range. A slight increase of τ_1 was observed in the vicinity of the N-I phase transition region due to the rapid decrement of the elastic constant, *K*. In the case of confined 8CB, τ_1 remain constant when 8CB is in the nematic phase. When temperature approaches the N-A phase transition point, τ_1 increases slightly with decreasing temperature. This is due to the tremendous increase of viscosity with the decrease in temperature. Similarly, τ_1 also increases in the vicinity of N-I phase transition temperature.

However, the confinement effect does change the static and dynamic properties of LCs quantitatively. For example, τ_1 is larger in confined samples than that in the bulk in the whole temperature range, and the relaxation processes are slower. A clear shift of T_{NI} is also observed for confined LCs. The phase transition region of confined sample becomes broader, and the change of *Isc* is less prominent; whereas, there is a sharp increase in *Isc* for bulk LCs at the phase transition temperature.

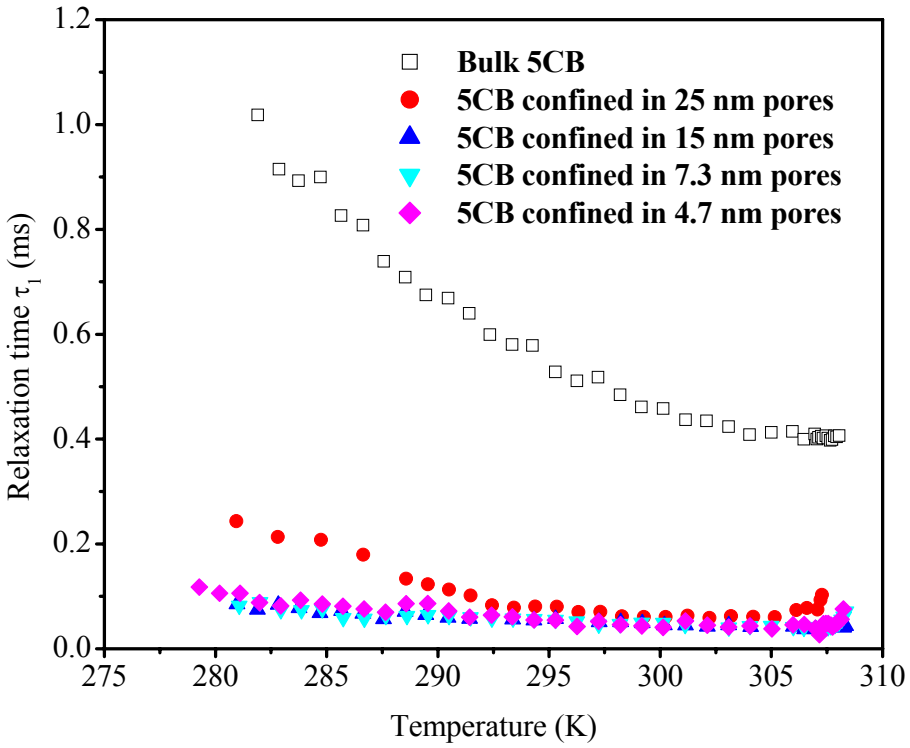


Figure 5.19. Temperature dependence of τ_1 for bulk and confined 5CB.

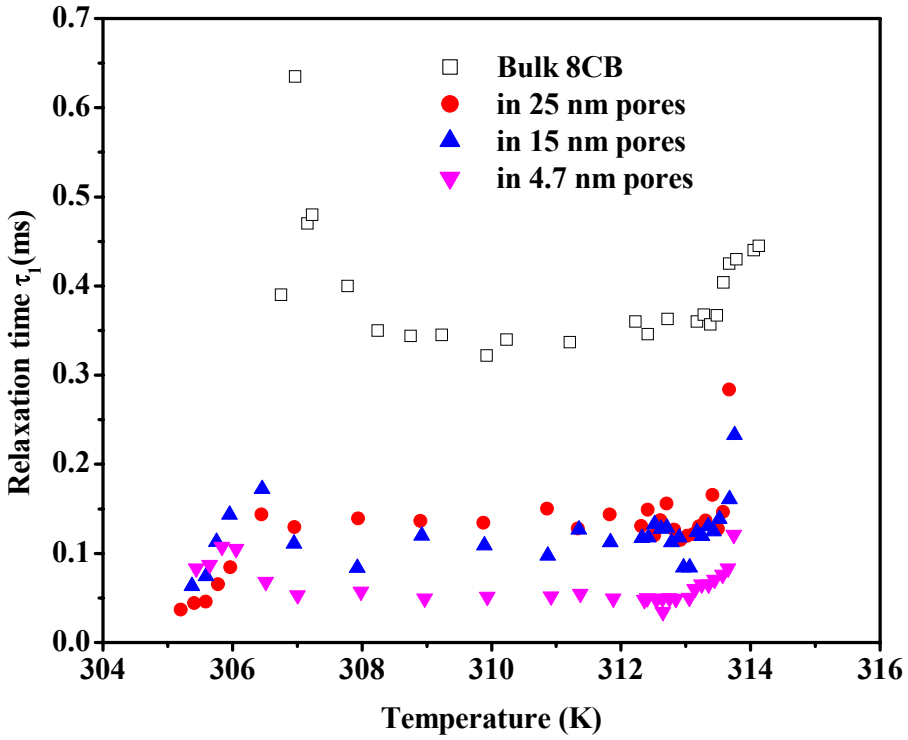


Figure 5.20. Temperature dependence of τ_1 for bulk and confined 8CB.

We might note that the relaxation time τ_1 of bulk-like director fluctuations for confined LCs is larger than that in the bulk LCs. This phenomenon can be explained as follows: For bulk LCs, τ_1 can be expressed as:

$$\tau_1(bulk) = \langle \eta \rangle / Kq^2 \tag{5.4}$$

For both bulk and confined sample, the measurements are performed at wave number corresponding to the linear size:

$$L = 2\pi / q \tag{5.5}$$

where q is the scattering vector defined as:

$$q = \frac{4\pi n}{\lambda} \sin\left(\frac{\theta}{2}\right) \tag{5.6}$$

Therefore, we can calculate L if the values of n, λ, θ are known. In our experiments, L is equal to 760 nm. This means that the size L is much larger than the pore diameter of SBA-15 used in our experiments. In this case, q should be replaced by $2\pi / R$ for a confined sample, and τ_1 is expressed by:

$$\tau_1(confined) = \langle \eta \rangle R^2 / 4\pi^2 K \tag{5.7}$$

We can further write:

$$\frac{\tau_1(confined)}{\tau_1(bulk)} = \frac{R^2 q^2}{4\pi^2} = 0.015 \tag{5.8}$$

That means $\tau_1(bulk) \approx 67\tau_1(confined)$. Our experiments results show that in the nematic phase, $\tau_1(bulk) \approx 67\tau_1(confined)$ for 5CB and $\tau_1(bulk) \approx 67\tau_1(confined)$ for 8CB, respectively. Since the local elasticity does

not change much with the pore size, this discrepancy between the theoretical estimation and experimental results can only be explained by the increment of effective viscosity of LCs due to the confinement effects.

If we denote the effective viscosity of bulk and confined sample by η_b and η_c, respectively, we have:

$$\frac{\tau_1(confined)}{\tau_1(bulk)} = \left(\frac{\eta_c}{\eta_b}\right)\left(\frac{R^2q^2}{4\pi^2}\right) \qquad (5.9)$$

Therefore, the change of the effective viscosity can be written as:

$$\left(\frac{\eta_c}{\eta_b}\right) = \frac{\tau_1(confined)}{\tau_1(bulk)}\left(\frac{4\pi^2}{R^2q^2}\right) \qquad (5.10)$$

By substituting the experimental value, we can deduce that the effective viscosity of the confined LCs is larger than that in the bulk. The ratios for both 8CB and 5CB under different confinement geometry are presented in **Figure 5.21**.

5.3 Dielectric Spectroscopy

The dielectric properties of bulk 5cb have been well studied[84-87]. 5CB molecules have the dipole moment in parallel to the molecular long axis. When the probing electric field is parallel to the director of the liquid crystal; we observe the relaxation process due to the restricted rotation of molecules around their short axes in *MHz* range at the temperature corresponding to the bulk nematic phase. In the isotropic phase, the same relaxation process shifted to the higher frequencies.

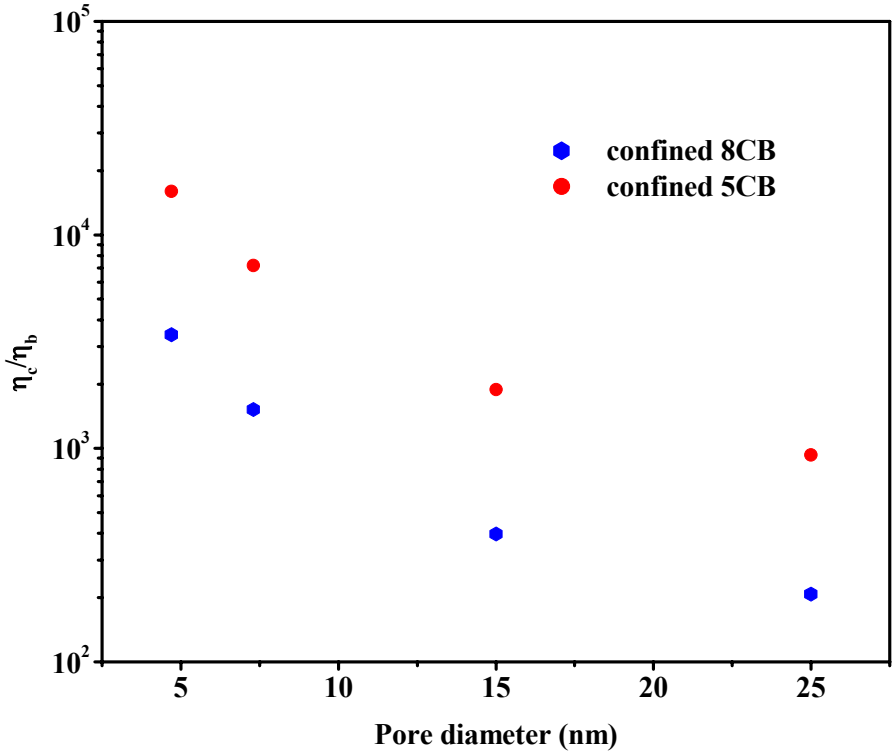


Figure 5.21. Pore size dependence of effective viscosity.

Dielectric spectra of bulk 5CBin nematic phase and isotropic phases are shown in **Figure 5.22**. Dielectric spectroscopy is used to study the relaxation process due to molecular reorientation around molecular short axis. Non-Debye relaxation processes with a distribution of relaxation times were observed for all confined LC systems. The confinement strongly influences the dynamical behaviors of the LCs and has resulted in qualitative changes in their properties. Previous studies[82, 88-92] showed that 5CB confind in 100 nm and 200 nm pores has lower isotropic-nematic phase transition temperature, and the phase transition region was broader. While in 10 nm pores[91], the relaxation processes are not frozen even at temperatures about 20 degrees below the bulk crystallization temperature, the smooth and small change of relaxation time at the phase transition temperature suggests that the "isotropic" phase of LCs in pores is not bulklike isotropic phase with complete disorder in molecular orientations, and some degree of orientational order still persists. If the pore size is much less than the correlation length of the liquid crystal, the system can be considered as quasi-one dimensional system.

If the pore size is much less than the correlation length of LCs, and the pores are of cylindrical shape, the system can be considered as quasi-1-dimensional system. One-dimensional systems are interesting, in particular, because according to Landau theory[93-95], no phase transition should occur. 5CB confined in 2.3 nm pores is such a system. We found that in this extreme confined system, the relaxation process due to molecular reorientations around

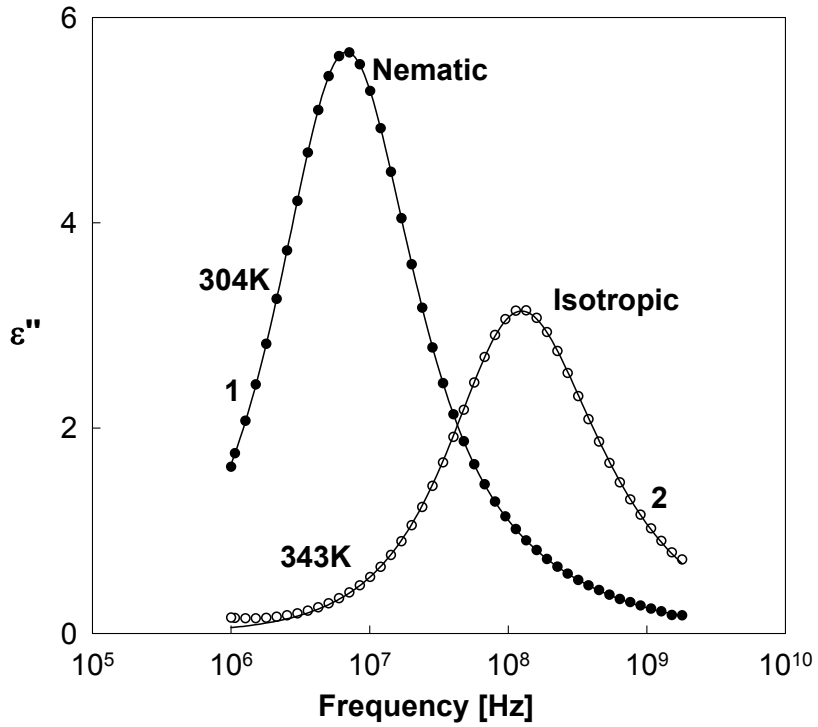


Figure 5.22. Dielectric spectra of bulk 5CB in nematic (1) and isotropic (2) phases. Symbols : experiment; solid lines : fitting.

short axis is dielectrically active at temperatures much above the bulk I-N transition temperature. However, the relaxation rate is much slower and the dielectric spectrum is much broader than that in the bulk. The difference of dielectric spectra between bulk 5CB and 5CB confined in 2.3 nm pores at temperature corresponding to bulk isotropic phase temperature is shown in **Figure 5.23**. The broadening of the relaxation time distribution and slowing down of relaxation process in confined 5CB is clearly seen in **Figure 5.24**. The dielectric spectra were analyzed using the Havriliak-Negami function[80]:

$$\varepsilon^* = \varepsilon_\infty + \sum_j \frac{\varepsilon_S - \varepsilon_\infty}{\left[1 + \left(i2\pi\omega\right)^\alpha\right]^\beta}$$

The parameters α and β in Havriliak-Negami function for confined 5CB are determined as $\alpha \approx 0.65$ and $\beta \approx 0.67$ respectively, while their values are very close to 1 for bulk 5CB.

Also, we observed that, instead of undergoing the I-N phase transition in very narrow pores, LC inside pores solidifies; relaxation of molecular orientations freezes out upon cooling the sample from the isotropic phase. Neither I-N nor N-SmA phase transition is observed in this extreme confined system, while in larger pores, these transitions are observed with a shift and broadening of the phase transition as compared to bulk liquid crystal. The broadening of dielectric spectra is observed in confined LCs. The broadening increases with decrease of pore size of the confining matrix.

As shown in **Figure 5.25**, for bulk 5CB, the temperature dependence of

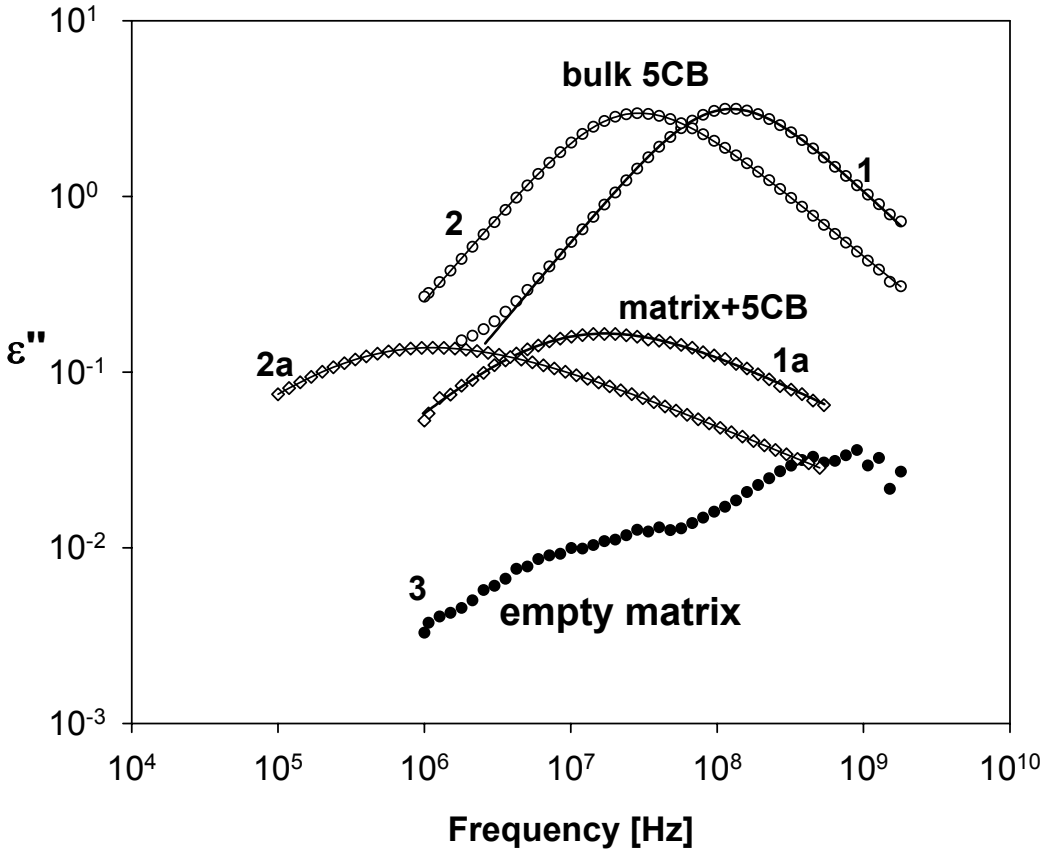


Figure 5.23. Dielectric spectra for bulk and confined liquid crystal.

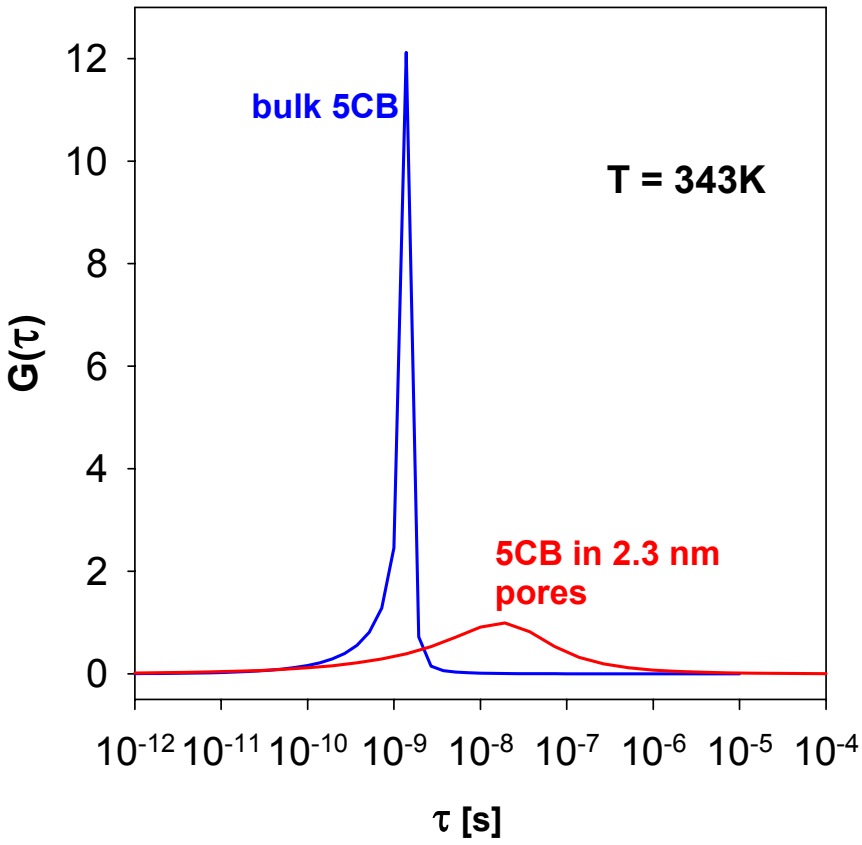


Figure 5.24. Relaxation time distribution functions for bulk and confined liquid crystal.

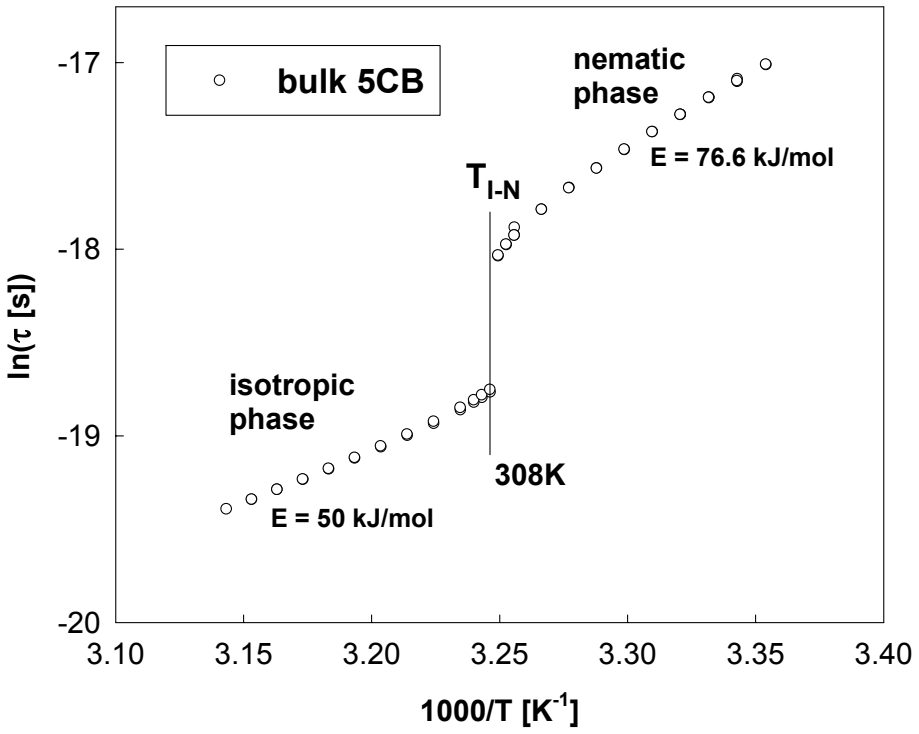


Figure 5.25. Temperature dependence of relaxation times of bulk 5CB.

relaxation time follows Arrhenius equation:

$$\tau = \tau_0 \exp(E/RT), \qquad (5.1)$$

where E is the activation energy, or the barrier to the dipole reorientation. The activation energy is larger in the nematic phase than that in the isotropic phase, because molecules encounter more hindrance in the nematic phase. Therefore, there is a jump in relaxation time at the phase transition temperature.

As shown in **Figure 5.26**, for 5CB confined in 2.3nm pores, temperature dependence of relaxation times cannot be described by an Arrhenius function. It shows Vogel- Fulcher temperature dependence [96] instead, with B = 1050K, T_0 = 250 K and $ln(\tau_0)$ = -25.39.

$$\tau = \tau_0 \exp[B/(T - T_0)]. \qquad (5.2)$$

If we determine the glass transition temperature T_g as the temperature at which τ = 100 s [96], then we obtain T_g = 285 K. This is the typical characteristic of glass-forming materials. Although bulk 5CB is not a glass-forming material, the confined 5CB shows glass-like behavior. We suggest that the slowing down of the mode may be due to the enhancement of the effective viscosity of 5CB under such narrow confinement and resulting glass-like dynamics.

Besides the dielectric spectroscopy experiments, we also performed static and dynamic light scattering experiments. In static light scattering experiment, we did not observe an isotropic-nematic phase transition in this quasi-1-dimensional

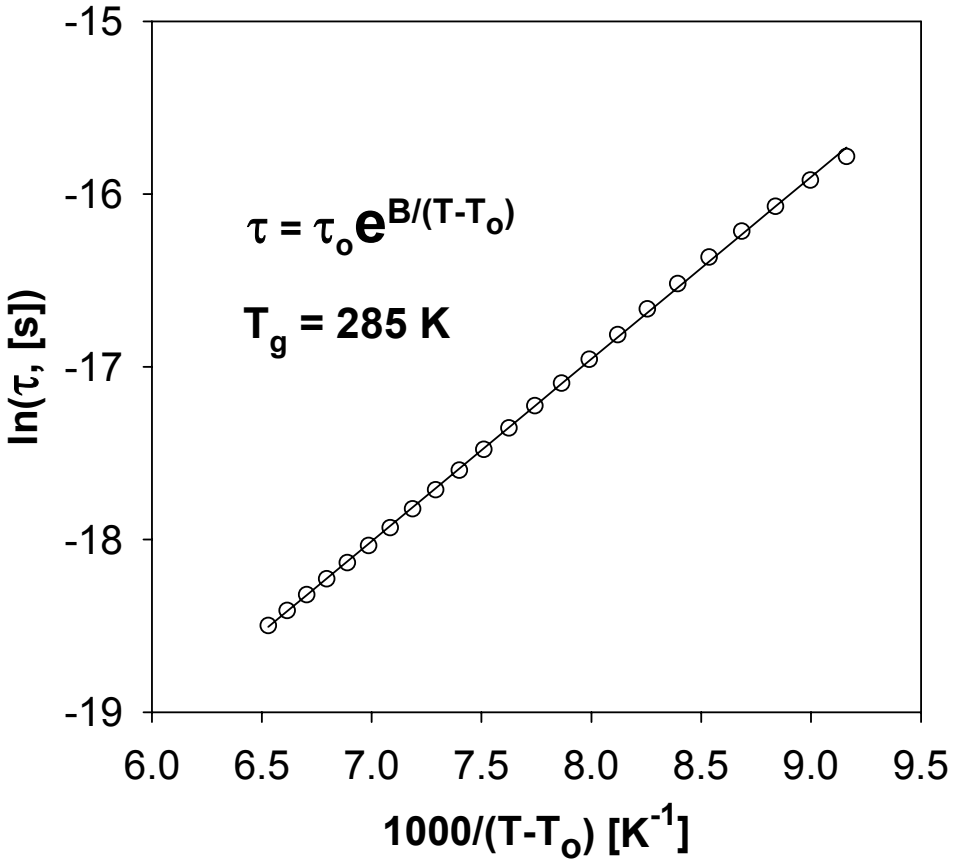


Figure 5.26. Temperature dependence of relaxation times of 5Cb confined in 2.3 nm pores.

system. In dynamic light scattering experiment, we investigate the fluctuations of director orientations. **Figure 5.27** shows the intensity-intensity autocorrelation function of bulk 5CB and a confined sample. For bulk 5CB, a well-defined relaxation process was observed; whereas the relaxation process of director orientational fluctuations was not observed for 5CB confined in 2.3 nm pores. In other words, the nematic phase is not formed, and therefore there is no director associated with nematic order.

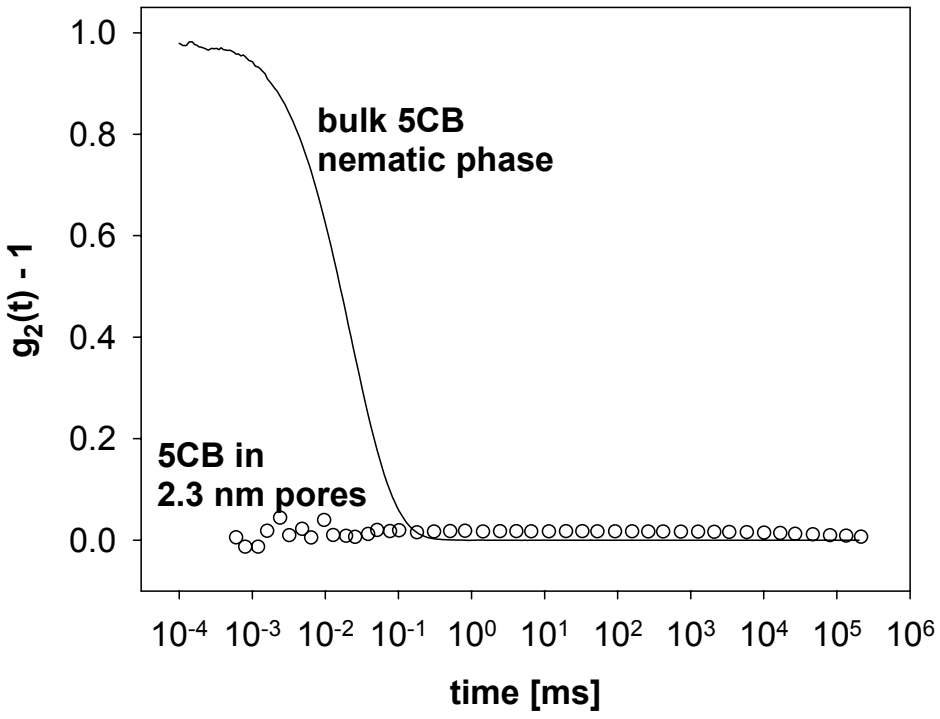


Figure 5.27. Intensity-intensity autocorrelation functions for bulk and 5cb confined in 2.3 nm pores.

CHAPTER 6 CONCLUSIONS AND FUTURE WORK

6.1 Static and Dynamic Light Scattering Conclusions

Significant changes in the physical properties of LCs impregnated in SBA-15 and MCM-41 were observed. For confined LCs in the nematic phase two well-defined relaxation processes were observed. The first relaxation process is qualitatively associated with bulk-like nematic director fluctuations. The second relaxation absent in bulk LCs (with relaxation time slower than the first one) is most likely due to the fluctuations in the layers nearest the wall surface. Neither relaxation process in confined LCs can be described by a single stretched exponential decay function. The separation between the first and the second (slow) process was clearer for LCs confined in matrices with smaller pore sizes and the amplitude of the slow process was greater for thinner layers. This suggests that the slow process was related to surface relaxation of director fluctuations. The pore size dependence of the nematic-isotropic phase transition temperature and the relaxation time of the first decay were revealed.

6.2 Dielectric Spectroscopy Conclusions

We have investigated the influence of confinement of 5CB (LC) on the N-I phase transition and the dynamics of molecular reorientations due to the rotation of molecules around their short axes under extreme confinement. The silica monolith used in this study has pore diameter of 2.3 nm, which is much less than the correlation length of LC. The nematic-isotropic phase transition does not occur in quasi 1D system. In other words, order parameter and director are not formed, and the dynamics is similar to that of supercooled liquids. Molecular reorientations were dielectrically active at temperatures much above the bulk N-I transition temperature, and the relaxation rate is much slower than that in the bulk material. The temperature dependence of relaxation time is described by Vogel – Fulcher formula that is typical for glass forming liquids. We suggest that the slowing down of the mode, which is molecular in the bulk material, may be due to enhancement of the effective viscosity of 5CB under such narrow confinement and result in glass-like dynamics.

6.3 Future Works

We have performed static and dynamic light scattering experiments and dielectric spectroscopy experiments for 5CB and 8CB confined in 2.3 nm, 4.7 nm , 7.3 nm 15 nm, and 25 nm pores. Thus, we have gotten a complete set of data to investigate how the geometric confinement and surface effect affect physical

properties and I-N phase transition of LCs. Further theoretical explanation need to be done.

Small-angle and wide-angle x-ray scattering techniques could be used to study Nematic-Smectic phase transitions of liquid crystals. We expect the geometric confinement and strong interfacial force to affect the phase change temperature, and the narrowest geometric confinement to alter the effective dimensionality (3-D -> 1-D) and hence the critical scaling of the liquid crystal. Therefore, it would be interesting if we could using this powerful technique to characterize the nematic to Smectic A phase transition of liquid crystal 5CB and 8CB in confined geometry as a function of the temperature and the pore size.

Also, we could also reveal the secret of the confinement effect and surface effects more clearly by varying the alignment of LC molecules near the surface. DSC is another technique that could be used to determine phase transition temperature precisely and test our results.

References Cited

1. Kresge, C.T., Leonowicz, M.E., Roth, W.J., Vartuli, J.C., and Beck, J.S., *Ordered Mesoporous Molecular-Sieves Synthesized by a Liquid-Crystal Template Mechanism.* Nature, 1992. 359(6397): p. 710-712.

2. Polarz, S. and Smarsly, B., *Nanoporous materials.* Journal of Nanoscience and Nanotechnology, 2002. 2(6): p. 581-612.

3. Stein, A., *Advances in microporous and mesoporous solids - Highlights of recent progress.* Advanced Materials, 2003. 15(10): p. 763-775.

4. Cai, Q., Luo, Z.S., Pang, W.Q., Fan, Y.W., Chen, X.H., and Cui, F.Z., *Dilute solution routes to various controllable morphologies of MCM-41 silica with a basic medium.* Chemistry of Materials, 2001. 13(2): p. 258-263.

5. Zhao, D.Y., Feng, J.L., Huo, Q.S., Melosh, N., Fredrickson, G.H., Chmelka, B.F., and Stucky, G.D., *Triblock copolymer syntheses of mesoporous silica with periodic 50 to 300 angstrom pores.* Science, 1998. 279(5350): p. 548-552.

6. Zhao, D.Y., Huo, Q.S., Feng, J.L., Chmelka, B.F., and Stucky, G.D., *Nonionic triblock and star diblock copolymer and oligomeric surfactant syntheses of highly ordered, hydrothermally stable, mesoporous silica structures.* Journal of the American Chemical Society, 1998. 120(24): p.

6024-6036.

7. Beck, J.S., Vartuli, J.C., Roth, W.J., Leonowicz, M.E., Kresge, C.T., Schmitt, K.D., Chu, C.T.W., Olson, D.H., Sheppard, E.W., Mccullen, S.B., Higgins, J.B., and Schlenker, J.L., *A New Family of Mesoporous Molecular-Sieves Prepared with Liquid-Crystal Templates.* Journal of the American Chemical Society, 1992. 114(27): p. 10834-10843.

8. Cheng, C.F., Luan, Z.H., and Klinowski, J., *The Role of Surfactant Micelles in the Synthesis of the Mesoporous Molecular-Sieve Mcm-41.* Langmuir, 1995. 11(7): p. 2815-2819.

9. Cheng, C.F., He, H.Y., Zhou, W.Z., and Klinowski, J., *Crystal Morphology Supports the Liquid-Crystal Formation Mechanism for the Mesoporous Molecular-Sieve Mcm-41.* Chemical Physics Letters, 1995. 244(1-2): p. 117-120.

10. Chen, C.Y., Burkett, S.L., Li, H.X., and Davis, M.E., Microporous Mater., 1993(2): p. 27.

11. Beck, J.S., *U. S. Patent, 5,057,57296*. 1991.

12. Branton, P.J., Dougherty, J., Lockhart, G., and White, J., W., Charact. Porous solids, 1997. IV: p. 668.

13. Desplantier-Giscard, D., Galarneau, A., Di Renzo, F., and Fajula, F. *Abstracts of Posters*. in *15th Annual Meeting of French Zeolite Association*. 1999. IFP: CarryLe Rouet.

14. Nagamine, S., Endo, A., Nakaiwa, M., Nakane, T., Kurumada, K., and Tanigaki, M., *Synthesis of submillimeter-thick films of surfactant templated mesoporous silica.* Microporous and Mesoporous Materials, 2001. 43(2): p. 181-189.

15. Sartor, G., Hallbrucker, A., Hofer, K., and Mayer, E., *Calorimetric Glass Liquid Transition and Crystallization Behavior of a Vitreous, but Freezable, Water Fraction in Hydrated Methemoglobin.* Journal of Physical Chemistry, 1992. 96(12): p. 5133-5138.

16. Crupi, V., Magazu, S., Majolino, D., Maisano, G., and Migliardo, P., *Dynamical response and h-bond effects in confined liquid water.* Journal of Molecular Liquids, 1999. 80(2-3): p. 133-147.

17. Morishige, K. and Nobuoka, K., *X-ray diffraction studies of freezing and melting of water confined in a mesoporous adsorbent (MCM-41).* Journal of Chemical Physics, 1997. 107(17): p. 6965-6969.

18. Morishige, K. and Kawano, K., *Freezing and melting of water in a single cylindrical pore: The pore-size dependence of freezing and melting*

behavior. Journal of Chemical Physics, 1999. 110(10): p. 4867-4872.

19. Li, J.C., Ross, D.K., and Benham, M.J., *Small-Angle Neutron-Scattering Studies of Water and Ice in Porous Vycor Glass.* Journal of Applied Crystallography, 1991. 24: p. 794-802.

20. Zanotti, J.M., Bellissent-Funel, M.C., and Chen, S.H., *Relaxational dynamics of supercooled water in porous glass.* Physical Review E, 1999. 59(3): p. 3084-3093.

21. Crupi, V., Majolino, D., Migliardo, P., Venuti, V., and Bellissent-Funel, M.C., *Structure and dynamics of water confined in a nanoporous sol-gel silica glass: a neutron scattering study.* Molecular Physics, 2003. 101(22): p. 3323-3333.

22. Koga, K., Zeng, X.C., and Tanaka, H., *Freezing of confined water: A bilayer ice phase in hydrophobic nanopores.* Physical Review Letters, 1997. 79(26): p. 5262-5265.

23. Slovak, J., Koga, K., Tanaka, H., and Zeng, X.C., *Confined water in hydrophobic nanopores: Dynamics of freezing into bilayer ice.* Physical Review E, 1999. 60(5): p. 5833-5840.

24. Bellissentfunel, M.C., Bradley, K.F., Chen, S.H., Lal, J., and Teixeira, J.,

Slow Dynamics of Water-Molecules in Confined Space. Physica A, 1993. 201(1-3): p. 277-285.

25. Crupi, V., Majolino, D., Migliardo, P., and Venuti, V., *Neutron scattering study and dynamic properties of hydrogen-bonded liquids in mesoscopic confinement. 1. The water case.* Journal of Physical Chemistry B, 2002. 106(42): p. 10884-10894.

26. Lee, C.Y., Mccammon, J.A., and Rossky, P.J., *The Structure of Liquid Water at an Extended Hydrophobic Surface.* Journal of Chemical Physics, 1984. 80(9): p. 4448-4455.

27. Spohr, E., *Molecular dynamics simulation studies of the density profiles of water between (9-3) Lennard-Jones walls.* Journal of Chemical Physics, 1997. 106(1): p. 388-391.

28. Fang, J.X., Marlow, W.H., Lu, J.X., and Lucchese, R.R., *Monte Carlo studies of effects of substrate size on water-substrate interaction energy and wafer structure.* Journal of Chemical Physics, 1997. 107(13): p. 5212-5216.

29. Zhu, S.B. and Robinson, G.W., *Structure and Dynamics of Liquid Water between Plates.* Journal of Chemical Physics, 1991. 94(2): p. 1403-1410.

30. Lee, S.H. and Rossky, P.J., *A Comparison of the Structure and Dynamics of Liquid Water at Hydrophobic and Hydrophilic Surfaces - a Molecular-Dynamics Simulation Study.* Journal of Chemical Physics, 1994. 100(4): p. 3334-3345.

31. Spohr, E., Hartnig, C., Gallo, P., and Rovere, M., *Water in porous glasses. A computer simulation Study.* Journal of Molecular Liquids, 1999. 80(2-3): p. 165-178.

32. Dosseh, G., Morineau, D., and Alba-Simionesco, C., *Benzene confined in MCM-41 below its melting point: A proton NMR study.* Journal De Physique Iv, 2000. 10(P7): p. 99-102.

33. Dosseh, G., Xia, Y.D., and Alba-Simionesco, C., *Cyclohexane and benzene confined in MCM-41 and SBA-15: Confinement effects on freezing and melting.* Journal of Physical Chemistry B, 2003. 107(26): p. 6445-6453.

34. Jobic, H., *Dynamics of molecules in confinement and technical relevance.* Jounal De Physique IV, 2000. 10: p. 125-130.

35. Gavrilko, T., gnatyuk, I., Puchkovskaya, G., Goltsov, Y., Matkovskaya, L., Baran, J., Drozd, M., and Ratajczak, H., *Effect of encapsulation in MCM-41 type molecular sieves on vibrational spectra of liquid crystalline state.*

Vibrational Spectroscopy, 2000. 23: p. 199-206.

36. Iannacchione, G.S., Crawford, G.P., Zumer, S., Doane, J.W., and Finotello, D., *Randomly Constrained Orientational Order in Porous-Glass.* Physical Review Letters, 1993. 71(16): p. 2595-2598.

37. Kralj, S., Zidansek, A., Lahajnar, G., Zumer, S., and Blinc, R., *Phase behavior of liquid crystals confined to controlled porous glass studied by deuteron NMR.* Physical Review E, 1998. 57(3): p. 3021-3032.

38. Cramer, C., Cramer, T., Kremer, F., and Stannarius, R., *Measurement of orientational order and mobility of a nematic liquid crystal in random nanometer confinement.* Journal of Chemical Physics, 1997. 106(9): p. 3730-3742.

39. Vilfan, M., Apih, T., Gregorovic, A., Zalar, B., Lahajnar, G., Zumer, S., Hinze, G., Bohmer, R., and Althoff, G., *Surface-induced order and diffusion in 5CB liquid crystal confined to porous glass.* Magnetic Resonance Imaging, 2001. 19(3-4): p. 433-438.

40. Zidansek, A., Kralj, S., Repnik, R., Lahajnar, G., Rappolt, M., Amenitsch, H., and Bernstorff, S., *Smectic ordering of octylcyanobiphenyl confined to control porous glasses.* Journal of Physics-Condensed Matter, 2000. 12(8A): p. A431-A436.

41. Crawford, G.P. and Zumer, S., *Lquid Crystals in Complex Geometies formed by porous and polymer networks*. 1996: Taylor & Francis. 325-370.

42. Basu, S. and Aliev, F.M., *Dynamic light scattering in liquid crystal confined to cylindrical pores: Effect of different layer thicknesses and boundary conditions.* Molecular Crystals and Liquid Crystals, 2004. 421: p. 49-60.

43. Bengoechea, M.R., Basu, S., and Aliev, F.M., *Dielectric relaxation in liquid crystal confined to cylindrical pores: Effect of different layer thicknesses and boundary conditions.* Molecular Crystals and Liquid Crystals, 2004. 421: p. 187-196.

44. Bellini, T., Clark, N.A., Muzny, C.D., Wu, L., Garland, C.W., Schaefer, D.W., Olivier, B.J., and Oliver, B.J., *Phase-Behavior of the Liquid-Crystal 8cb in a Silica Aerogel.* Physical Review Letters, 1992. 69(5): p. 788-791.

45. Clark, N.A., Bellini, T., Malzbender, R.M., Thomas, B.N., Rappaport, A.G., Muzny, C.D., Schaefer, D.W., and Hrubesh, L., *X-Ray-Scattering Study of Smectic Ordering in a Silica Aerogel.* Physical Review Letters, 1993. 71(21): p. 3505-3508.

46. Zeng, H.R., Zalar, B., Iannacchione, G.S., and Finotello, D., *Effects of*

quenched disorder on the orientational order of the octylcyanobiphenyl liquid crystal. Physical Review E, 1999. 60(5): p. 5607-5618.

47. Yokoyama, H., *Nematic-isotropic transition in bound thin films.* Jounal of the Chemical Society, Faraday Transitions 2: Molecular and CHemical Phsics, 1988. 84(8): p. 1023-1040.

48. Copic, M. and Mertelj, A., *Reorientation in random potential: A Model for glasslike dynamics in confined liquid crystals.* Physical Review Letters, 1998. 80(7): p. 1449-1452.

49. Stallinga, S., Wittebrood, M.M., Luijendijk, D.H., and Rasing, T., *Light scattering by thin nematic liquid crystal films.* Molecular Crystals and Liquid Crystals Science and Technology Section a-Molecular Crystals and Liquid Crystals, 1997. 304: p. 231-234.

50. Wittebrood, M.M., Luijendijk, D.H., Stallinga, S., Rasing, T., and Musevic, I., *Thickness-dependent phase transition in thin nematic films.* Physical Review E, 1996. 54(5): p. 5232-5234.

51. Stallinga, S., Wittebrood, M.M., Luijendijk, D.H., and Rasing, T., *Theory of light scattering by thin nematic liquid crystal films.* Physical Review E, 1996. 53(6): p. 6085-6092.

52. Mertelj, A. and Copic, M., *Evidence of dynamic long-range correlations in a nematic-liquid-crystal-aerogel system.* Physical Review E, 1997. 55(1): p. 504-507.

53. Batalla, B., Sinha, G., and Aliev, F., *Dynamics of molecular motion of nematic liquid crystal confined in cylindrical pores.* Molecular Crystals and Liquid Crystals Science and Technology Section a-Molecular Crystals and Liquid Crystals, 1999. 331: p. 1981-1988.

54. Aliev, F.M., *Photon correlation spectroscopy of confined liquid crystals in isotropic, nematic, and smectic phases.* Molecular Crystals and Liquid Crystals Science and Technology Section a-Molecular Crystals and Liquid Crystals, 1999. 329: p. 1129-1136.

55. Aliev, F.M. *Dynamics of liquid crystals confined in random porous martices*. in *Acess in Nanoporous Materials*. 1995: Plenum Press, New York.

56. Sinha, G. and Aliev, F., *Glass-like relaxation in confined liquid crystals.* Molecular Crystals and Liquid Crystals, 2001. 358: p. 155-166.

57. Leheny, R.L., Park, S., Birgeneau, R.J., Gallani, J.L., Garland, C.W., and Iannacchione, G.S., *Smectic ordering in liquid-crystal-aerosil dispersions. I. X-ray scattering.* Physical Review E, 2003. 67(1): p. -.

58. Iannacchione, G.S., Park, S., Garland, C.W., Birgeneau, R.J., and Leheny, R.L., *Smectic ordering in liquid-crystal-aerosil dispersions. II. Scaling analysis.* Physical Review E, 2003. 67(1): p. -.

59. Imperor-Clerc, M., Davidson, P., and Davidson, A., *Existence of a microporous corona around the mesopores of silica-based SBA-15 materials templated by triblock copolymers.* Journal of the American Chemical Society, 2000. 122(48): p. 11925-11933.

60. Ravikovitch, P.I. and Neimark, A.V., *Characterization of micro- and mesoporosity in SBA-15 materials from adsorption data by the NLDFT method.* Journal of Physical Chemistry B, 2001. 105(29): p. 6817-6823.

61. Erin H. Lay, A. Kirakosian, J.-L. Lin, D. Y. Petrovykh, J. N. Crain, and Himpsel, F.J., *Alignment of Liquid Crystals on Stepped and Passivated Silicon Templates Prepared in Ultrahigh Vacuum.* Langmuir, 2000. 16: p. 6731-6738.

62. Cumpston, B.H., Ananthavel, S.P., Barlow, S., Dyer, D.L., Ehrlich, J.E., Erskine, L.L., Heikal, A.A., Kuebler, S.M., Lee, I.Y.S., McCord-Maughon, D., Qin, J.Q., Rockel, H., Rumi, M., Wu, X.L., Marder, S.R., and Perry, J.W., *Two-photon polymerization initiators for three-dimensional optical data storage and microfabrication.* Nature, 1999. 398(6722): p. 51-54.

63. Rouquerol, J., Avnir, D., Fairbridge, C.W., Everett, D.H., Haynes, J.H., Pernicone, N., Ramsay, J.D.F., Sing, K.S.W., and Unger, K.K., *Recommendations for the Characterization of Porous Solids.* Pure and Applied Chemistry, 1994. 66(8): p. 1739-1758.

64. Berne, B.J. and Pecora, P., *Dynamic light scattering with applications to chemisry, biology, and physics*. 1976, New York: Wiley.

65. Val'kov, A.Y., Romanov, V.P., and Shalaginov, *Fluctuations and light scattering in liquid crystals.* Physics-Uspekhi, 1994. 37(2): p. 139-183.

66. Gennes, P.G.d. and Prost, J., *The Physics of Liquid Crystals*. 2nd Ed. ed. 1993: Clarendon Press, Oxford.

67. Chatelain, P., Acta Crystallogr, 1948. 1: p. 315.

68. Ehrentraut, H., *Elastic distortions of a nematic liquid crystal*, in *http://wwwitp.physik.tuberlin.de/muschik/liquid_crystals/lc_intro.html*. 1997.

69. Ericksen, J.L., Arch. Ration. Mech. Anal, 1960. 4: p. 231.

70. Ericksen, J.L., Phys. Fluids, 1966. 9: p. 1205.

71. Leslie, F.M., Quart. J. Mech. Anal., 1966. 19: p. 357.

72. Leslie, F.M., Arch. Ration. Mech. Anal, 1968. 28: p. 265.

73. Parodi, O.J., J. Phys. (Paris), 1970. 31: p. 581.

74. Salin, D., Smith, I.W., and Durand, G., J. Phys. (Paris), 1974. 35: p. L-165.

75. Chu, K.C. and Mcmillan, W.L., Phys. Rev. A, 1976. 11: p. 1059.

76. Delaye, M., J. Phys. (Paris), 1976. 37: p. C3-99.

77. Birecki, H. and Lister, J.D., Mol. Crys. Liq. Cryst., 1977. 42: p. 33.

78. Huang, C.C., Pindak, R.S., Flanders, P.J., and Ho, J.T., Phys. Rev. Lett., 1974. 33: p. 400.

79. Leger, L. and Martinet, A., J. Phys. (Paris), 1976. 37: p. C3-89.

80. Havriliak, S. and Negami, S., Polymer, 1967. 8: p. 101.

81. *Handbook of liquid crystal research*, ed. e.i.c. Peter J. Collings and Jay S. Patel. 1997: New York ; Oxford: Oxford University Press.

82. Frunza, S., Frunza, L., and Schonhals, A., *Dielectric measurements of liquid crystals confined to molecular sieves.* Journal De Physique Iv, 2000. 10(P7): p. 115-118.

83. Aliev, F., Kreuzer, M., Tabiryan, N., and zel'dovich, B., *Light scattering and photon correlation spectroscopy of filled and confined liqid crystals.* Mol. Crys. Liq. Cryst., 1998. 320: p. 173-191.

84. P. G. Cummins, D. A. Danmur, and Laidler, D.A., Mol. Crys. Liq. Cryst., 1975. 30(30): p. 109.

85. D. Lippens, J. P. Parneix, and Chapoton, A., J. de Phys., 1977. 38: p. 1465.

86. J. M. Wacrenier, C. Druon, and Lippens, D., Mol. Phys., 1981. 43: p. 97.

87. Urban, S., Gestblom, B., and Wurflinger, A., *Comparison of the dielectric relaxation data for the isotropic and nematic phases of three homologous series: nCb, nOCB and nPCH, (n=5 divided by 8).* Molecular Crystals and Liquid Crystals Science and Technology Section a-Molecular Crystals and Liquid Crystals, 1999. 331: p. 1973-1980.

88. Rozanski, S.A., Stannarius, R., Groothues, H., and Kremer, F., *Dielectric properties of the nematic liquid crystal 4-n-pentyl-4'-cyanobiphenyl in porous membranes.* Liquid Crystals, 1996. 20(1): p. 59-66.

89. Cramer, C., Cramer, T., Arndt, M., Kremer, F., Naji, L., and Stannarius, R., *NMR and dielectric studies of nano-confined nematic liquid crystals.* Molecular Crystals and Liquid Crystals Science and Technology Section

a-Molecular Crystals and Liquid Crystals, 1997. 303: p. 209-217.

90. Sinha, G.P. and Aliev, F.M., *Dielectric relaxation of nematic liquid crystal confined in porous matrices.* Molecular Crystals and Liquid Crystals Science and Technology Section a-Molecular Crystals and Liquid Crystals, 1997. 304: p. 309-314.

91. Sinha, G.P. and Aliev, F.M., *Dielectric spectroscopy of liquid crystals in smectic, nematic, and isotropic phases confined in random porous media.* Physical Review E, 1998. 58(2): p. 2001-2010.

92. Aliev, F.M., Nazario, Z., and Sinha, G.P., *Broadband dielectric spectroscopy of confined liquid crystals.* Journal of Non-Crystalline Solids, 2002. 305(1-3): p. 218-225.

93. Peierls, R., *Transition temperatures.* Helvetica Phsica Acta, 1934. 7(Suppl. II): p. 81-83.

94. Landau, L., *Theory of phase changes. I.* Physikalische Zeitschrift der Sowjetunion, 1937. 11: p. 26-47.

95. Hohenberg, P.C., *Exisitance of long-range order in one and two dimensions in superfluids and superconductors.* Phys. Rev., 1967. 158(2): p. 383-386.

96. R. Richert, A. Blumen, and Verlag, S., *Disorder Effects on Relaxational Processes*. 1994, Berlin.

VITA

Yang Gao was born in Bejing, China on July 7th, 1973. She graduated from Jilin high school in 1992. From there, she went to Tianjing University, the oldest University in China, and received a B.S. in fine chemical engineering in 1996. After that, she started working as an assistant engineer in Jilin Dye Plant, the oldest and biggest dye plant in China. In 1998, she was admitted into Tianjin University as a graduate student majored in Chemical engineering, and received a M.S. in 2001.

Yang is currently pursuing her doctorate in chemical engineering at University of Tennessee, Knoxville, TN.